

ulm university universität
uulm

Fakultät für
Naturwissenschaften
Institut für Elektrochemie

Atomistic multiscale modelling of degradation phenomena on metallic lithium electrodes

Dissertation zur Erlangung des akademischen Grades *doctor rerum naturalium* (Dr. rer. nat.)
an der Universität Ulm

Vorgelegt von:
Matthias van den Borg
aus Ulm

2025

Fassung 1. Juni 2025

Amtierender Dekan:
Prof. Dr. Kay-E. Gottschalk

Gutachter:
Prof. Dr. Timo Jacob (Erstgutachter)
Prof. Dr. Arnulf Latz (Zweitgutachter)

Tag der mündlichen Prüfung:
24.03.2025

Danksagung

An dieser Stelle möchte ich mich bei allen bedanken, die mich im Rahmen dieser Arbeit unterstützt, motiviert und inspiriert haben.
Zuallererst möchte ich Prof. Dr. T. Jacob meinen aufrichtigen Dank dafür aussprechen dass er mir die Möglichkeit gegeben hat an spannenden wissenschaftlichen Fragestellungen zu arbeiten und eine Dissertation am Institut für Elektrochemie zu schreiben. Sein umfangreiches Wissen war ausgesprochen wertvoll für die Gestaltung meiner Arbeit und sein konstruktives Feedback hat mir maßgeblich dabei geholfen, die Herausforderungen meiner Dissertation zu meistern.
Herrn Prof. Dr. A. Latz möchte ich für die freundliche Bereitschaft sich als Zweitgutachter bereitzustellen danken.
Ich möchte mich auch besonders bei Dr. D. Fantauzzi bedanken, da er mich während meiner Masterarbeit und zu Beginn der Promotion unterstützt, und mich mit seinem Enthusiasmus stets inspiriert hat. Seine Hingabe und sein Rat trugen wesentlich dazu bei, den Grundstein für diese Arbeit zu legen und mein Verständnis der Multiskalenmodellierung zu prägen.
Weiterhin möchte ich mich bei Dr. E. Knobbe für sein unermüdliches Engagement und seine freundschaftliche Zusammenarbeit bedanken, die für mich von unschätzbarem Wert waren.
Ein großes Dankeschön geht auch an alle Kolleginnen und Kollegen am Institut für Elektrochemie. Mein besonderer Dank gilt hierbei meinen Freunden und Kollegen aus der Theoriegruppe Daniel, Christoph, Björn und Florian. Es war ein Privileg mit euch allen zusammenzuarbeiten und ich bin dankbar für die schöne gemeinsame Zeit am Institut.
Zu guter Letzt möchte ich mich herzlichst bei meiner Freundin und meiner Familie für ihre unermüdliche Unterstützung und Ermutigung bedanken. Ihre Liebe, Geduld und Aufopferung haben mir geholfen, all meine Ziele zu erreichen. Ihr wart stets eine Quelle der Kraft für mich und ohne euch wäre diese Arbeit nicht möglich gewesen.

Contents

1 Introduction **4**

2 Theory **8**

2.1 Multiscale Modeling 8

2.2 Quantum Mechanical Methods 10

2.2.1 Schrödinger Equation 10

2.2.2 Density Functional Theory (DFT) 11

Hohenberg-Kohn-Theorem 1 11

Hohenberg-Kohn-Theorem 2 12

Kohn-Sham Equations 13

The Exchange-Correlation Functional 15

2.2.3 Implementation of DFT 17

2.3 ReaxFF 19

2.3.1 Bonding Interactions 20

2.3.2 Non-bonding Interactions 22

2.3.3 ReaxFF in the Multiscale Approach 24

3 Theoretical studies on the initial oxidation of metallic lithium anodes 26

3.1 Abstract 27

3.2 Introduction 27

3.3 Computational details 29

3.4 Results and discussion 32

3.4.1 Adsorption and absorption on/by lithium surfaces 32

3.4.2 Dissociative adsorption/absorption of O_2 37

3.4.3 Diffusion of absorbates 39

3.4.4 Coverage-dependent absorption 41

3.5 Conclusions . . . 48

4 A first principle study on the initial nitride formation on lithium metal 51
4.1 Abstract . . . 52
4.2 Introduction . . . 52
4.3 Results and discussion . . . 55
4.3.1 Nitrogen adsorption/absorption . . . 55
4.3.2 Diffusion of monoatomic nitrogen on Li(100) and in Li(*bcc*) bulk 58
4.3.3 Diffusion and dissociation processes of molecular N_2 on Li(100) 61
4.3.4 Coverage-dependent absorption on Li(100) . . . 65
4.4 Conclusions . . . 68

5 Atomistic studies on water-induced lithium corrosion 70
5.1 Abstract . . . 71
5.2 Introduction . . . 72
5.3 Computational details . . . 74
5.4 Results and discussion . . . 76
5.4.1 Hydrogen adsorption/absorption energies . . . 76
5.4.2 Mobility of Hydrogen on Li(100) and Li(*bcc*) . . . 80
5.4.3 Mobility and dissociation of OH on Li(100) . . . 83
5.4.4 Mobility and dissociation of water on Li(100) . . . 86
5.4.5 Hydrogen evolution on Li(100) . . . 88
5.5 Conclusion . . . 92

6 ReaxFF guided simulation of lithium anode oxidation 95
6.1 Abstract . . . 96
6.2 Introduction . . . 96
6.3 Computational details . . . 99
6.3.1 ReaxFF parameterisation and calculations . . . 99
6.3.2 DFT calculations . . . 99
6.3.3 ReaxFF GCMC . . . 100
6.3.4 Settings for molecular dynamics . . . 101
6.4 Results and discussion . . . 102
6.4.1 Optimization and validation of Li-O parameters . . . 102
6.4.2 Oxidation of lithium nanoparticles . . . 108
6.5 Conclusion . . . 112

7 Further work **113**
7.1 Microscopic Properties of Na and Li-A First Principle Study of Metal Battery Anode Materials 114
7.2 First-Principles Studies on the Atomistic Properties of Metallic Magnesium as Anode Material in Magnesium-Ion Batteries 116
7.3 KVIK Optimiser - An Enhanced ReaxFF Force Field Training Approach 117
7.4 Development of a Mg/O ReaxFF Potential to describe the Passivation Processes in Magnesium-Ion Batteries 119
7.5 Cornforth–Evans transition states in stereocontrolled allylborations of epoxy aldehydes 121
7.6 Multifunctional Polyoxometalate Platforms for Supramolecular Light-Driven Hydrogen Evolution 123

8 Summary and Outlook **125**

A Appendix **129**
A.1 Theoretical studies on the initial oxidation of metallic lithium anodes 129
A.2 A first principle study on the initial nitride formation on lithium metal 134
A.3 Atomistic studies on water-induced lithium corrosion 135
A.4 ReaxFF guided simulation of lithium anode oxidation 138

Bibliography **141**

Publications

This thesis is based on the following publications and drafts:

1. *Theoretical studies on the initial oxidation of metallic lithium anodes*
   Matthias van den Borg, Daniel Gaissmaier, Edwin Knobbe, Donato Fantauzzi, Timo Jacob
   Appl. Surf. Sci. **2021**, *555*, 149447

2. *Atomistic studies on water-induced lithium corrosion*
   Matthias van den Borg, Daniel Gaissmaier, Edwin Knobbe, Donato Fantauzzi, Timo Jacob
   ChemSusChem **2022**, *15*, e2021017

3. *A first principle study on the initial nitride formation on lithium metal*
   Matthias van den Borg, Daniel Gaissmaier, Edwin Knobbe, Timo Jacob
   To be submitted

4. *ReaxFF guided simulation of lithium anode oxidation*
   Matthias van den Borg, Daniel Gaissmaier, Florian Fiesinger, Edwin Knobbe, Timo Jacob
   To be submitted

Publications included in abstract form:

5. *Microscopic Properties of Na and Li-A First Principle Study of Metal Battery Anode Materials*
   Daniel Gaissmaier, Matthias van den Borg, Donato Fantauzzi, Timo Jacob
   ChemSusChem **2020**, *13*, 771-783

6. *Cornforth–Evans transition states in stereocontrolled allylborations of epoxy aldehydes*
   Robert R. A. Freund, Matthias van den Borg, Daniel Gaissmaier, Robin Schlosser, Timo Jacob, Hans-Dieter Arndt
   Chem.Eur.J. **2020**, *26*, 8639-8650

7. Multifunctional Polyoxometalate Platforms for Supramolecular Light-Driven Hydrogen Evolution
   Salam Maloul, Matthias van den Borg, Carolin Müller, Linda Zedler, Daniel Gaissmaier, Timo Jacob, Sven Rau, Benjamin Dietzek-Ivansic, Carsten Streb
   Chem. Eur. J. **2021**, *27*, 16846-16852

8. *First-Principles Studies on the Atomistic Properties of Metallic Magnesium as Anode Material in Magnesium-Ion Batteries*
   Florian Fiesinger, Daniel Gaissmaier, Matthias van den Borg, Timo Jacob
   ChemSusChem **2022**, *15*, e202200414

9. *KVIK Optimiser - An Enhanced ReaxFF Force Field Training Approach*
   Daniel Gaissmaier, Matthias van den Borg, Donato Fantauzzi, Timo Jacob
   ChemRxiv **2022**, DOI 10.26434/chemrxiv-2022-lrsjd

10. *Development of a Mg/O ReaxFF Potential to describe the Passivation Processes in Magnesium-Ion Batteries*
    Florian Fiesinger, Daniel Gaissmaier, Matthias van den Borg, Julian Beßner, Adri C. T. van Duin, Timo Jacob
    ChemSusChem **2023**, *16*, e202201821

Further publications:

11. *A novel and highly efficient indolyl-based electrolyte for Mg–batteries*
    Steve Zaubitzer, Saustin Dongmo, Philipp Schüler, Sven Krieck, Florian Fiesinger, Daniel Gaissmaier, Matthias van den Borg, Timo Jacob, Matthias Westerhausen, Margret Wohlfahrt-Mehrens, Mario Marinaro
    Energy Technol., **2022**, *10*, 2200440

12. *Suitability of Carbazolyl Hauser and Turbo-Hauser Bases as Magnesium-Based Electrolytes*
    Philipp Schüler, Simon Sengupta, Steve Zaubitzer, Florian Fiesinger, Saustin Dongmo, Helmar Görls, Margret Wohlfahrt-Mehrens, Matthias van den Borg, Daniel Gaissmaier, Sven Krieck, Mario Marinaro, Timo Jacob, Matthias Westerhausen
    Eur. J. Inorg. Chem., **2022**, *17*, e202200149

1

Introduction

Since the beginning of the industrial revolution the accelerated combustion of fossil fuels by anthropogenic activity has led to a large increase in greenhouse gases (GHGs) in the atmosphere [1]. The rapid growth in heat-trapping GHG concentrations in the atmosphere is causing a rise in global temperatures, commonly known as climate change. Global climate change is already having far-reaching impacts on people and the environment and is increasingly threatening our very existence as we know it [2–10]. With the transport sector as one of the largest contributors to anthropogenic GHG emissions, developing a sustainable transport concept is one of the most pressing challenges of our generation [11]. A shift away from hydrocarbon-based fuels is therefore urgently needed and will also be implemented politically in the automotive sector through bans on conventional combustion engines [12]. To realize this transformation, comprehensive electrification of land and air transport is required by replacing fossil fuels with electrical energy storage systems with high energy density.

In the field of electromobility, lithium-ion batteries (LIB) are a widespread key technology, which has become the standard for electric vehicles due to their relatively high gravimetric energy densities, long cycle life and low self-discharge rate [13–16]. Because of these advantageous properties, LIBs have also empowered a variety of other portable electronics, such as cell phones, laptops and tablets, where they are used extensively as a power source. In general, the main design of rechargeable LIBs consists of two intercalation compounds with different potentials, which are used as

cathode and anode, and an electrolyte, allowing the movement of the lithium ions between the two electrodes. In most commercial LIBs graphite is used as an anode, while the cathode typically contains a lithium metal oxide [14, 17]. During the charging and discharging process, the Li^+ ions are now shuttled back and forth between the two intercalation electrodes. This operating principle is based on an idea proposed by Michel Armand in the 1970s and is widely known as "rocking-chair" technology [18, 19].

Despite the considerable progress made in the development of LIBs in the last few decades, rocking-chair technology is reaching its limits in the long term [17, 20–22]. As LIBs slowly approach the theoretical value of the respective cathode and anode materials, the use of other electrode materials within a new battery technology becomes inevitable to reach energy densities that can compete with those of fossil fuels.

Batteries that are based on a negative metallic lithium electrode belong to the most promising technologies in terms of high specific energies and energy densities. This is due to the extraordinarily favourable characteristics of lithium: with an atomic weight of only 6.94 u and a standard electrode potential of -3.04 V, lithium is not only the lightest metal but also shows the most negative standard electrode potential of all chemical elements in the periodic table [23]. With an exceptionally high theoretical capacity of 3862 mA h g^{-1} (2062 mA h cm^{-3}), metallic lithium is is one of the most attractive anode materials for high-energy-density batteries [13, 14, 24, 25].

A commercial application of metallic lithium in batteries on a large scale, however, faces several challenges and safety concerns that must first be surmounted. A significant safety risk is the free growth of lithium whiskers and dendrites during charge and discharge cycles, which in the worst case can even cause a thermal runaway of the battery due to an internal cell short circuit [26–29].

Additional challenges arise from lithium's high reactivity. As metallic lithium is thermodynamically unstable in contact with the electrolyte, irreversible and continuous reactions with the electrolyte at the anode interface result in the formation of a passivating solid electrolyte interphase (SEI) [25, 30–38]. The formation of the SEI through a variety of undesirable side reactions with liquid organic electrolytes ultimately leads to lower reversibility, consumption of electrolyte, loss of active lithium, and low Coulomb efficiency (CE). Although the SEI protects the anode from further degradation, large volume and morphology changes during deposition/stripping of Li render the SEI film

brittle with repeated cycling. This leads to further lithium loss through constant breakage and reformation of the SEI, as the freshly exposed Li surfaces react rapidly with the electrolyte. The growth of the whiskers/dendrites is closely related to the SEI, as the surface component and structure of the layer have a high impact on the morphology of the Li deposition. In addition, the formation of whiskers/dendrites exacerbates further SEI formation due to their high surface-to-bulk ratio. Consequently, several concepts have been developed to increase the efficiency, cycling stability, and safety of metallic lithium anodes by controlling the SEI. These approaches range from the optimization of the electrolyte, mechanical surface modifications over to the introduction of an artificial, controlled SEI film [28, 39–42].

Despite the various approaches and the correspondingly large number of studies on the modification and manipulation of the metallic lithium anode and its interface, however, comparatively little scientific work in this area is devoted to the quantitative characterization of the composition, morphology and electronic properties of the pristine lithium surfaces, which ultimately react with electrolytes and form the interface. Even before the reaction in the battery, the metallic lithium surface can be contaminated with impurities from the atmosphere during processing. Atmospheric impurities can also enter the battery via the electrolyte and have a lasting effect on the efficiency of the lithium anode, as lithium is known to react violently with many species present in the ambient environment, such as O_2, N_2 and H_2O [43–50].

Since experimental methods encounter severe limitations on an atomic level in terms of spatial, time and energy resolution, theoretical calculations have emerged as a very promising approach in recent times to face the comprehension of the atomistic mechanisms in electrochemical systems. Quantum chemical methods such as density functional theory (DFT) are characterized by their comparatively high accuracy and often provide detailed insight into the structural and electronic properties of a chemical system [51, 52]. However, due to their high computational cost and poor scaling with system size, *ab-initio* methods are limited to relatively small systems and are unable to capture many battery-relevant processes on the required time and length scales. Classical molecular dynamics, on the other hand, enables the treatment of much larger systems, but not the simulation of chemical reactions. The idea behind reactive force fields like the bond-order-based ReaxFF is to bridge the gap between quantum mechanical methods and classical molecular dynamics by extending a proper description of chemical reactions to larger time and length scales [53]. By determining

and updating the bond order, ReaxFF, in contrast to classical force fields, allows the simulation of the formation and cleavage of chemical bonds at a much lower computational cost than quantum chemical methods. Within the ReaxFF framework, the interatomic interactions are captured through a parameterized potential and require therefore extensive optimizations and adaptations to a training set based on *ab-initio* calculations.

This work aims to develop a deeper understanding of the initial degradation phenomena on the metallic Li electrode caused by the intrusion of the atmospheric constituents O_2, N_2 and H_2O. Fundamental principles, thermodynamic stabilities, morphologies, electronic properties, and reaction processes will be identified and classified for the interaction of these impurities with metallic lithium. A significant part of this work is therefore devoted to the identification of the most important degradation processes at a quantum mechanical level via DFT simulations through the simulation of comparatively small model systems. Using the insights from DFT, a ReaxFF-based multiscale approach for the oxidation of metallic lithium is developed to model the ongoing processes on larger time and length scales. For the passivation of a lithium anode, a Li-O ReaxFF potential is therefore optimized thus paving the way for a powerful tool that might guide the evolution of the metallic lithium anode.

2

Theory

2.1 Multiscale Modeling

The field of theoretical chemistry encompasses numerous methods for predicting the properties and behaviour of a chemical system at different levels with varying degrees of accuracy. Within a multi-scale approach as presented in Fig. 2.1, these methods are combined hierarchically, with the most accurate and computationally demanding models being used at smaller scales, while less computationally expensive models are used at larger scales. This hierarchical approach allows for efficient simulations that capture relevant details at each level of resolution. In the lower left corner one finds quantum mechanical methods, such as Hartree-Fock (HF) and Density functional theory (DFT), which all represent *ab - initio* approaches. By calculating the electronic structure, these methods (to some extent) do not use empirical data and represent ways to numerically approximate the solution of the Schrödinger equation. The HF method for instance uses the so-called mean-field approach, to approximatively calculate wave functions and orbital energies. This enables the calculation of fundamental properties of molecular, bulk and surface systems. Despite relatively good accuracy, $ab\text{-}initio$ methods are however restricted to rather small systems.

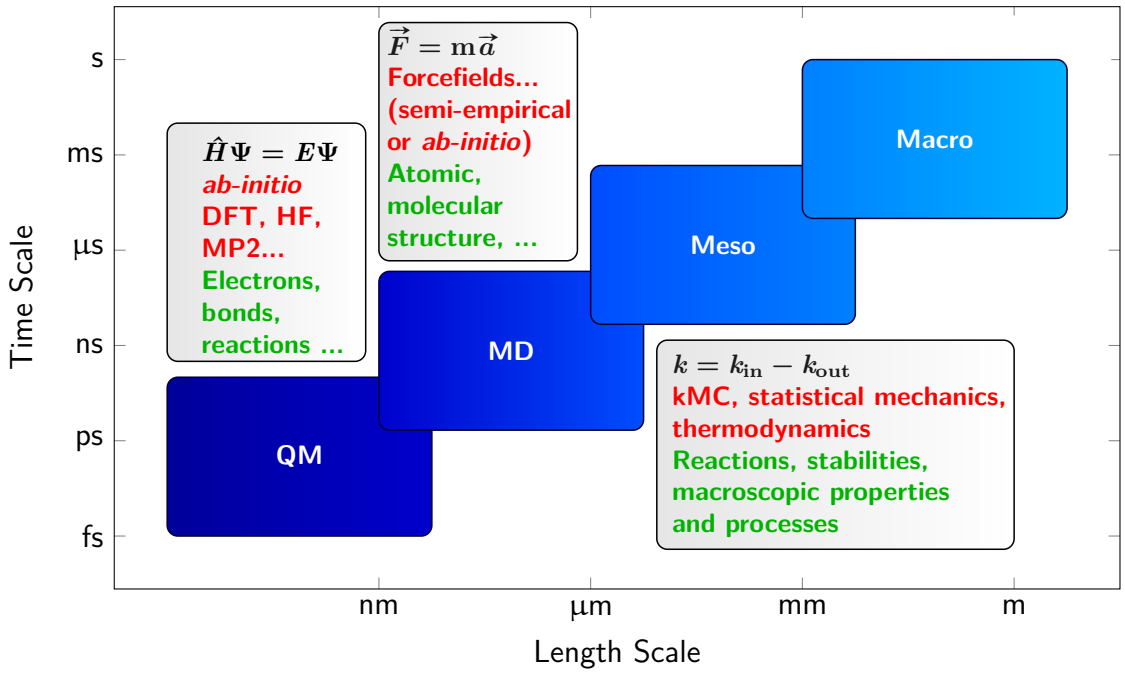

Figure 2.1. Schematic representation of the different methods in computational chemistry within their different length and time scales and the respective possible applications.

As the computational effort increases tremendously with the number of electrons, the outermost limit for these methods lies in the magnitude of pico seconds and nanometres. In comparison, molecular dynamics (MD) methods using classical force fields provide a means to simulate larger systems. In this approach, force fields utilize potential energy terms originating from classical mechanics to calculate the system's energy. While *ab-initio* methods are restricted to chemical systems containing a few hundred atoms, force fields enable the simulation of tens of thousands of particles within a MD framework. As conventional force fields do not explicitly include electrons, adjustments to an experimental or higher-level theoretical calculations training set are necessary to determine the parameters for the potential energy terms. It is important to note that these adjustments and the inherent limitations of force fields result in comparatively lower accuracy when compared to *ab-initio* methods. Additionally, the applicability of force fields is confined to chemical problems included in the training data set, thereby limiting their effectiveness in addressing chemical phenomena beyond those parameters.

2.2 Quantum Mechanical Methods

2.2.1 Schrödinger Equation

For a complete theoretical description of a system, it is necessary to consider all interactions within the system, which can be summarised in the Hamiltonian. The Hamiltonian $\hat{H}$ contains the whole information of a system so that every physical and chemical property can be determined through it

$$\hat{H} = \underbrace{-\frac{1}{2}\sum_{\mathrm{i}}\vec{\nabla}_{\mathrm{i}}^2}_{\hat{T}_{\mathrm{el}}} \underbrace{-\frac{1}{2}\sum_{\mathrm{I}}\frac{1}{M_{\mathrm{I}}}\vec{\nabla}_{\mathrm{I}}^2}_{\hat{T}_{\mathrm{nucl}}} + \underbrace{\sum_{\mathrm{i,I}}\frac{Z_{\mathrm{I}}}{\left|\vec{r}_{\mathrm{i}}-\vec{R}_{\mathrm{I}}\right|}}_{\hat{V}_{\mathrm{nucl-el}}} + \underbrace{\frac{1}{2}\sum_{\mathrm{i}\neq\mathrm{j}}\frac{1}{\left|\vec{r}_{\mathrm{i}}-\vec{r}_{\mathrm{j}}\right|}}_{\hat{V}_{\mathrm{el-el}}} + \underbrace{\frac{1}{2}\sum_{\mathrm{I}\neq\mathrm{J}}\frac{Z_{\mathrm{I}}Z_{\mathrm{J}}}{\left|\vec{R}_{\mathrm{I}}-\vec{R}_{\mathrm{J}}\right|}}_{\hat{V}_{\mathrm{nucl-nucl}}}. \tag{2.1}$$

Using atomic units ($\hbar = e = m_{\mathrm{el}} = 1$), in this equation $\vec{\nabla} = \frac{\partial}{\partial x}\cdot\vec{e_{\mathrm{x}}} + \frac{\partial}{\partial y}\cdot\vec{e_{\mathrm{y}}} + \frac{\partial}{\partial z}\cdot\vec{e_{\mathrm{z}}}$ is the Nabla operator, $\vec{r}_{\mathrm{i}}$ represents the position of the electron (el) and M_{I}, Z_{I} and $\vec{R}_{\mathrm{I}}$ are the mass, charge and position of the nuclei (nucl). T_{el} and T_{nucl} denote the kinetic energy of the electrons and the atomic nuclei, while $V_{\mathrm{nucl-el}}$ denotes the attractive electrostatic interactions between nuclei and electrons, and $V_{\mathrm{nucl-nucl}}$ as well as $V_{\mathrm{el-el}}$ label the repulsive interactions between like-charged nuclei or electrons, respectively.

By knowing the Hamiltonian the time-independent, non-relativistic Schrödinger equation (SE) [54] can be formulated:

$$\hat{H}\Psi\left(\vec{R},\vec{r}\right) = E\Psi\left(\vec{R},\vec{r}\right). \tag{2.2}$$

With wave function $\Psi\left(\vec{R},\vec{r}\right)$, which depends on the coordinates of nuclei $\vec{R}$ and electrons $\vec{r}$, as eigenfunction and E as eigenvalue, the SE corresponds to an eigenvalue equation, with which in principle every property of a system can be calculated. However, the SE can only be solved analytically for a very small number of systems and due to many-body effects, more complex systems with more than one electron require the application of approximation methods. As a first measure to approximatively solve the SE, the Born-Oppenheimer approximation [55] is applied. The Born-Oppenheimer approximation is based upon the large mass difference between nuclei and electrons,

which are due to their small mass, much faster than the nuclei. Hence electrons follow the movement of nuclei instantaneously. In the course of this approximation, the electronic Hamiltonian $\hat{H}_{\mathrm{el}}$ for fixed nuclear coordinates $\left\{\vec{R}\right\}$ can be formulated:

$$\hat{H}_{\mathrm{el}}\left(\left\{\vec{R}\right\}\right) = \hat{T}_{\mathrm{el}} + \hat{V}_{\mathrm{nucl-el}} + \hat{V}_{\mathrm{el-el}}. \tag{2.3}$$

The electronic SE is therefore given by

$$\hat{H}_{\mathrm{el}}\left(\left\{\vec{R}\right\}\right)\Psi_{\mathrm{el}}\left(\vec{r},\left\{\vec{R}\right\}\right) = E_{\mathrm{el}}\left(\left\{\vec{R}\right\}\right)\Psi_{\mathrm{el}}\left(\vec{r},\left\{\vec{R}\right\}\right). \tag{2.4}$$

As can be seen in equation 2.4, the electronic SE just depends on the electron coordinates $\vec{r}$. Nevertheless, the equation is still, despite the approximation, too complex to solve, as the computational cost increases immensely with the number of electrons. Consequently, further approximation procedures are needed to lower the computational cost. In this context, DFT represents an approach, where the computational effort to approximately solve the many-body SE is tremendously reduced in comparison to other quantum mechanical methods.

2.2.2 Density Functional Theory (DFT)

With N as the number of electrons, the many-body wave function depends on $3N$ coordinates, which causes high computational cost for a large number of electrons. Therefore DFT uses the electron density instead of the many-body wave function, which only depends on three spatial coordinates. The coordinates of every single atom are therefore no longer required for the calculation of the ground state energy, which corresponds to a large decrease in computational cost. The foundation for DFT is given by the two Hohenberg-Kohn-theorems, which were presented by Walter Kohn and Pierre Hohenberg in 1964 [51].

Hohenberg-Kohn-Theorem 1

The first theorem establishes the connection between the electron density of the ground state and the external potential. It states that every ground state electron density $n\left(\vec{r}\right)$ of an interacting many-electron system in an external potential $V_{\mathrm{ext}}\left(\vec{r}\right)$, uniquely

defines this potential, which can be proved by contradiction. Although this proof merely reveals the linkage between electron density and external potential for a non-degenerate ground state, the first Hohenberg-Kohn-theorem can easily be extended to degenerate cases as well. Through the unique relation between the electron density and the external potential, the Hamiltonian $\hat{H}$ and consequently every property of the ground state, like its wave function Ψ_0 and energy E_0, can be determined through the ground state electron density n_0:

$$n_0 \Rightarrow V_{\text{ext}} \Rightarrow \hat{H} \Rightarrow \Psi_0 \Rightarrow E_0 \tag{2.5}$$

The ground state energy of a many-electron system is therefore a unique functional of the electron density.

Hohenberg-Kohn-Theorem 2

The second theorem of Hohenberg and Kohn is an application of the Rayleigh-Ritz variational principle from wave functions to electron densities and states, that the functional gives the lowest energy only if the input electron density $n(\vec{r})$ is equal to the system's true ground state electron density. By adhering to the essential boundary condition of preserving the total number of electrons N in the system with $N = \int n(\vec{r}) d^3\vec{r}$, the second Hohenberg-Kohn theorem can therefore be used to determine the exact ground state energy E_0 by minimizing the energy functional. The ground state energy E_0 thus serves as a boundary value that is attained exclusively when the trial electron density $n(\vec{r})$ corresponds precisely to the ground state electron density $n_0(\vec{r})$:

$$E\left[n\left(\vec{r}\right)\right] \geq E_0 \tag{2.6}$$

Utilizing both the Hohenberg-Kohn theorems, the determination of the ground state energy becomes feasible. However, while the first Hohenberg-Kohn theorem establishes the ground state energy as a functional of the electron density, it does not define a universally applicable functional $E[n(\vec{r})]$. Given the absence of an exact expression for the electron density functional, the approach introduced by Kohn and Sham [52], emerges as a widely embraced variant of DFT.

Kohn-Sham Equations

In 1965 Walter Kohn and Lu Jeu Sham introduced a method to perform DFT, which simplified the problem by replacing the interacting many-body system in an external potential $V_{\mathrm{ext}}(\vec{r})$ through a non-interacting many-body system in an effective potential $V_{\mathrm{eff}}(\vec{r})$. The demand for the effective potential is that it generates the same ground state density as the interacting many-body system [52]. Using this approach, which is known as the Kohn-Sham Ansatz, one can now separate the constructed non-interacting many-body system into single-particle equations, so that the total energy can be expressed as a sum of all the energies of the non-interacting electrons and the energies, which arise from the electron-electron-interaction:

$$\begin{aligned} E\left[n\left(\vec{r}\right)\right] &= \underbrace{\sum_{\mathrm{i}=1}^{N} \int \phi^{*}(\vec{r}_{\mathrm{i}}) \frac{\nabla^{2}}{2} \phi(\vec{r}_{\mathrm{i}}) d\vec{r}_{\mathrm{i}}}_{E_{\mathrm{kin}}[n(\vec{r}_{\mathrm{i}})]} + \underbrace{\int V_{\mathrm{ext}}(\vec{r}_{\mathrm{i}}) n(\vec{r}_{\mathrm{i}}) d\vec{r}_{\mathrm{i}}}_{E_{\mathrm{ext}}[n(\vec{r})]} \\ &+ \underbrace{\int\int \frac{n(\vec{r}_{\mathrm{i}}) n(\vec{r}_{\mathrm{j}})}{|\vec{r}_{\mathrm{i}} - \vec{r}_{\mathrm{j}}|} d\vec{r}_{\mathrm{i}} d\vec{r}_{\mathrm{j}}}_{E_{\mathrm{H}}[n(\vec{r})]} + E_{\mathrm{xc}}\left[n\left(\vec{r}\right)\right] \\ &= E_{\mathrm{kin}}\left[n\left(\vec{r}\right)\right] + E_{\mathrm{ext}}\left[n\left(\vec{r}\right)\right] + E_{\mathrm{H}}\left[n\left(\vec{r}\right)\right] + E_{\mathrm{xc}}\left[n\left(\vec{r}\right)\right]. \end{aligned} \tag{2.7}$$

The first and second terms in equation 2.7 are the kinetic energy E_{kin} and the potential energy of electrons in the external potential E_{ext}. These terms correspond to the energies of non-interacting electrons. The third and fourth terms represent the energies which result from the interaction between the electrons. Here, E_{H} describes the Coulomb interaction between the electrons, while the exchange-correlation term E_{xc} includes all non-classical electron-electron interactions.

As a consequence of the second Hohenberg-Kohn theorem, the energy functional must be minimized with respect to the electron density to find the energy of the ground state. By applying the variational principle, one obtains the so-called Kohn-Sham equations:

$$\left[-\frac{1}{2}\vec{\nabla}^{2} + V_{\mathrm{eff}}(\vec{r}_{\mathrm{i}})\right] \phi_{\mathrm{i}}(\vec{r}) = \varepsilon_{\mathrm{i}} \phi_{\mathrm{i}}\left(\vec{r}\right). \tag{2.8}$$

In equation 2.8 V_{eff} is the effective potential, which summarizes all potentials acting on the electrons:

$$V_{\mathrm{eff}}(\vec{r}) = V_{\mathrm{ext}}(\vec{r}) + V_{\mathrm{H}}(\vec{r}) + V_{\mathrm{xc}}(\vec{r}). \tag{2.9}$$

The potential $V_{\mathrm{ext}}(\vec{r})$ and $V_{\mathrm{H}}(\vec{r})$ are the external potential and the Hartree potential for the classical electrostatic interaction between electrons, while $V_{\mathrm{xc}}(\vec{r})$ is the exchange-correlation potential, which is given by the derivative of the exchange-correlation functional $E_{\mathrm{xc}}\left[n\left(\vec{r}\right)\right]$:

$$V_{\mathrm{xc}}(\vec{r}) = \frac{\delta E_{\mathrm{xc}}[n(\vec{r})]}{\delta n(\vec{r})}. \tag{2.10}$$

The derivation of the Kohn-Sham equations is similar to other methods for solving the many-body Schrödinger equation, such as the Hartree and Hartree-Fock methods. This likeness stems from the shared underlying procedure, emphasizing a fundamental similarity in their principles. In contrast to the one particle Schrödinger-equation the eigenvalues ε_{i} in equation 2.8 are however not necessarily the eigenenergies, but Lagrange multipliers, which guarantee the orthogonality between two Kohn-Sham orbitals in the virtual non-interacting system. Solving the Kohn-Sham equations eventually allows the determination of the electron density:

$$n(\vec{r}) = \sum_{\mathrm{i}=1}^{N} |\phi_{\mathrm{i}}|^2. \tag{2.11}$$

Knowing the correct electron density, one can now determine the ground state energy:

$$E_0 = \sum_{\mathrm{i}=1}^{N} \varepsilon_{\mathrm{i}} + E_{\mathrm{xc}}[n\left(\vec{r}\right)] - \int V_{\mathrm{xc}} n\left(\vec{r}\right) d\vec{r} - V_{\mathrm{H}} + V_{\mathrm{nucl-nucl}}. \tag{2.12}$$

Solving the Kohn-Sham equations, however, already requires prior knowledge of the electron density due to the incorporation in the exchange-correlation potential, which inherently includes the electron density $n\left(\vec{r}\right)$, as indicated in equation 2.10. As a result, the solution of the Kohn-Sham equations has to follow an iterative fashion using a self-consistent field (SCF) method. In this method, an initial trial electron density is assumed to solve the Kohn-Sham equation to acquire refined Kohn-Sham orbitals. The electron density is then recalculated using these updated orbitals, and the process

iterates until reaching a state of self-consistency. Due to equation 2.10 the choice of the exchange-correlation functional is a crucial factor for calculating the exchange and correlation effects of the electrons.

The Exchange-Correlation Functional

The exchange-correlation functional is a key component of DFT, as it accounts for all quantum mechanical many-body effects, providing a direct path to determine the ground state energy of a chemical system. However, the exact mathematical expression of the exchange-correlation functional remains elusive, making the use of approximation methods imperative. Consequently, the performance and accuracy of the DFT method depend heavily on the choice of the exchange-correlation approximation. The approximations follow different approaches, with the local density approximation (LDA) and the generalized gradient approximation (GGA) arguably being among the most popular.
In LDA the exchange-correlation energy is derived through the Jellium model for solids, a uniform electron gas (*i.e.* a uniform electron density) which is compensated by a positive background charge representing the atomic nuclei [56]:

$$E_{\mathrm{xc}}^{\mathrm{LDA}}[n(\vec{r})] = \int \; n(\vec{r}) \; \varepsilon_{\mathrm{xc}}^{\mathrm{LDA}}\,[n(\vec{r})]\,\mathrm{d}\,\vec{r}. \tag{2.13}$$

Here, $n(\vec{r})$ denotes the density of the uniform electron gas and $\varepsilon_{\mathrm{xc}}^{\mathrm{LDA}}[n(\vec{r})]$ the exchange-correlation energy per electron. The expression $\varepsilon_{\mathrm{xc}}^{\mathrm{LDA}}[n(\vec{r})]$ can be further divided into an explicitly calculated exchange $\varepsilon_{\mathrm{x}}[n(\vec{r})]$ and a correlation component $\varepsilon_{\mathrm{c}}[n(\vec{r})]$, approximated numerically through a quantum Monte Carlo approach [57]. The exchange-correlation energy of systems with an open electron shell configuration can be determined by explicitly including the spin within the local spin density approximation (LSDA) through

$$E_{\mathrm{xc}}^{\mathrm{LSDA}}[n(\vec{r})_{\alpha}, n(\vec{r})_{\beta}] = \int \; n(\vec{r})\varepsilon_{\mathrm{xc}}^{\mathrm{LSDA}}\,[n(\vec{r})_{\alpha}, n(\vec{r})_{\beta}]\,\mathrm{d}\,\vec{r}, \tag{2.14}$$

where $n(\vec{r})_{\alpha}$ and $n(\vec{r})_{\beta}$ refer to the local spin densities. Although uniform electron gas approximations are appropriate for describing metals due to their delocalized electron clouds, LDA is usually not an appropriate method for modelling localized covalent or ionic bonds. In most cases, LDA is also not suitable for the calculation of molecular

systems, since its use often leads to high overbinding due to the overestimation of the atomization energy [58]. In comparison to LDA, GGA represents a more sophisticated method. While LDA completely ignores the inhomogeneities of the electron density, GGA tries to factor in the irregularities by including gradients of the density. By taking into account the gradients of spin densities $n(\vec{r})_\alpha$ and $n(\vec{r})_\beta$, the general form of GGA can be expressed as

$$E_{\mathrm{xc}}^{\mathrm{GGA}}[n(\vec{r})_\alpha, n(\vec{r})_\beta] = \int n(\vec{r})\varepsilon_{\mathrm{xc}}^{\mathrm{LDA}}(n(\vec{r}))F_{\mathrm{xc}}[n_\alpha, n_\beta, \nabla n_\alpha, \nabla n_\beta]\mathrm{d}\vec{r}. \quad (2.15)$$

In equation 2.15 the term F_{xc} is a correction function which is referred to as enhancement factor. To calculate the contribution of the exchange-energy via

$$E_{\mathrm{x}}^{\mathrm{GGA}}[n(\vec{r})] = \int n(\vec{r})\varepsilon_{\mathrm{x}}^{\mathrm{LDA}}[n(\vec{r})]F_{\mathrm{x}}(s)\mathrm{d}\vec{r}. \quad (2.16)$$

the exchange enhancement factor F_{x} is used, which is often represented as a function of the reduced density gradient $s[n(\vec{r})]$. The different functionals use varying approximations for the exchange enhancement factor. For the widely used functional of Perdew, Burke and Ernzerhof (PBE) [59], the exchange enhancement factor is calculated as follows:

$$F_{\mathrm{x}}^{\mathrm{PBE}}(s) = 1 + \kappa - \frac{\kappa}{1 + \frac{\mu s^2}{\kappa}}, \ (\kappa = 0.804, \mu = 0.2195) \quad (2.17)$$

In addition to PBE, there are several other GGA functionals with varying degrees of accuracy. To address the challenge of quantifying uncertainties within an ensemble of different exchange-correlation functionals, Wellendorff *et al.* introduced the Bayesian Error Estimation Functional with Van der Waals Correlation (BEEF-vdW) [60], which is represented by:

$$E_{\mathrm{xc}}^{\mathrm{BEEF-vdW}}[n] = \sum_{\mathrm{m}} a_{\mathrm{m}} E_{\mathrm{m}}^{\mathrm{GGA-x}} + \alpha_{\mathrm{c}} E^{\mathrm{LDA-c}} + (1 - \alpha_{\mathrm{c}}) E^{\mathrm{PBE-c}} + E^{\mathrm{nl-c}}. \quad (2.18)$$

As can be seen from equation 2.18 the exchange-correlation energy is represented as a sum of contributions, incorporating semilocal GGA exchange energy ($E^{\mathrm{GGA-x}}$),

purely local LDA correlation ($E^{\mathrm{LDA-c}}$) as implemented by Perdew-Wang, semilocal PBE correlation ($E^{\mathrm{PBE-c}}$), and vdW-DF2 type nonlocal correlation ($E^{\mathrm{nl-c}}$). The inclusion of expansion factors (a_{m} and α_{c}) parameterized against diverse energetic and structural datasets, along with the prevention of overfitting through a divided cost function, enables BEEF-vdW to generate an ensemble of 2000 distinct functionals, each stemming from a probabilistic distribution of model parameters. This ensemble approach, which computes the standard deviation of energies, provides a robust means of addressing uncertainties in electronic structure calculations.

2.2.3 Implementation of DFT

Proper and efficient treatment of a periodic system with a great number of particles like bulk materials or surfaces within DFT is the application of periodic boundary conditions (PBC) in all three spatial directions so that the infinitely large system is approximated with the help of a small unit cell [56]. Implementation of efficient DFT calculations for such systems requires further approximations and expressions for the electron density. To solve the Kohn-Sham-equations, a suitable basis set ϕ, in which the Kohn-Sham orbitals can be expanded, has therefore to be found. Usually the wave function $\chi(\vec{r})$ is expanded in a linear combination of basis functions ϕ in the following fashion:

$$\chi_{\mathrm{i}=1}(\vec{r}) = \sum_{\mathrm{n}}^{\mathrm{N}} C_{\mathrm{i,n}} \phi_{\mathrm{n}}(\vec{r}). \tag{2.19}$$

Through the expansion in basis functions, designed to model the atomic orbitals, a linear combination of the so-called Kohn-Sham pseudo orbitals allows the calculation of the energy iteratively through the determination of the $C_{\mathrm{i,n}}$ coefficients. As bulk and surface systems represent infinitely large periodic frameworks, these systems are treated with periodic boundary conditions, which is equivalent to the periodic translation in all spatial directions. Consequently such a system comprises a unit cell within a translation lattice, which is defined through a set of basis vectors $\vec{a}_1$, $\vec{a}_2$, $\vec{a}_3$, whose combination forms the lattice vector $\vec{R}_{\mathrm{ijk}}$:

$$\vec{R}_{\mathrm{ijk}} = n_{\mathrm{i}}\,\vec{a}_1 + n_{\mathrm{j}}\,\vec{a}_2 + n_{\mathrm{k}}\,\vec{a}_3. \tag{2.20}$$

This lattice vector is related to a reciprocal set of basis vectors $\vec{b}_1$, $\vec{b}_2$, $\vec{b}_3$, which define the first Brillouin Zone. A point in real space is consequently given through the vector $\vec{r}$ and a point in reciprocal space through the wave vector $\vec{k}$. Due to the system's periodicity, the wave functions have to be compatible with the Bloch theorem, which is why it has to be applied to the Kohn-Sham pseudo orbitals:

$$\chi\left(\vec{r}+\vec{R}\right) = e^{\mathrm{i}\vec{\mathrm{k}}\cdot\vec{\mathrm{R}}}\chi_{\vec{\mathrm{k}}}\left(\vec{r}\right). \tag{2.21}$$

With the utilization of the expansion into Kohn-Sham pseudo orbitals into a linear combination of basis functions as in equation 2.19 one obtains the Bloch function for a specific system as shown in equation 2.22:

$$\chi_{\mathrm{i,n_r,L},\vec{\mathrm{k}}}(\vec{r}) = \sum_{\vec{\mathrm{R}}} e^{\mathrm{i}\vec{\mathrm{k}}\cdot\vec{\mathrm{R}}} C_{\mathrm{i,n}}\phi_{\mathrm{i,n_r,L}(\vec{\mathrm{r}}-\vec{\mathrm{R}})}. \tag{2.22}$$

Here n_r refers to the radial quantum number and $L = (l, m)$ to the quantum numbers for the basis function. Through this formulation, the Kohn-Sham pseudo orbital function is now additionally depending on the $\vec{k}$-vector, thus making the basis function suitable for the periodic boundary conditions. As the computational effort increases with the number of basis functions, which are required for the expansion of the wave function, a small basis set is desired. To reduce the size of the basis set and improve computational efficiency, the core electrons of atoms are often replaced with pseudopotentials.
The approach of not explicitly considering the core electrons is based on the fact that the chemical properties of most atoms are mainly determined by their valence electrons, while the influence of core electrons is negligible. Pseudopotentials must be generated individually for each element and can significantly speed up plane-wave calculations.
Within the PBC, surfaces are represented using the supercell approach, as the periodicity for surfaces is limited to only two spatial coordinates. Here, surfaces are represented by a slab, which corresponds to an arrangement of several atomic layers. To consider the PBC perpendicular to the surface, a sufficiently wide vacuum layer is applied to the slab. If the vacuum layer is wide enough, interactions in the periodic arrangement between the individual slabs are avoided.

2.3 ReaxFF

Given the unfavourable scaling of the computational cost of quantum mechanical methods with the number of electrons, empirical force fields are a notably efficient alternative for describing intermolecular forces. The fundamental concept behind force fields is to portray atoms in a simplified way, conceptualizing them as point masses within space and disregarding their intricate electronic structure. Meanwhile, the description of intermolecular interactions follows a systematic breakdown of the potential energy into relatively small mathematical terms. In general, the potential energy is consecutively fragmented into terms for the contribution of atom pairs, triplets and quadruplets, while higher interaction terms are not explicitly taken into account [61]. With respect to the character of the bonding, that is either covalent or not, these terms can be divided into bonding or non-bonding (or non-covalent) interactions. In so-called classical force fields, the bonding interactions are typically described using harmonic potentials. The determination of whether a bonding interaction exists between two atoms is established through a binding table at the beginning of a simulation. Throughout the course of a simulation employing a classical force field, this assignment remains static, thus precluding an effective representation of chemical bond dissociation within the classical framework.

To overcome the limitations of classical force fields, reactive force fields present a promising option. Through the employment of a reactive force field, this method allows the simulations of chemical reactions. Such reactive force fields don't utilize the approximation through harmonic potentials and consider the surroundings of atoms, which is a concept attributed to the work of Linus Pauling [62], where he established the connection between bond length and bond order. Therefore reactive force fields are based on a more sophisticated formulation and are thus more costly compared to regular force fields. Examples of reactive force fields, which are summed up under the term of *bond order potentials*, are among others the Tersoff potential [63], the Brenner potential [64] and ReaxFF [53]. The latter, ReaxFF, was developed at the *California Institute of Technology* by Adri C. T. van Duin and William A. Goddard III. and allows molecular dynamics simulations on a large scale. Similar to classical force fields, the formulation for reactive force fields comprises a sum of different contributions to the energy as shown in equation 2.23. Depending on the system, different terms are taken into account for the formulation:

$$
\begin{aligned}
E_{\text{system}} &= \underbrace{E_{\text{bond}} + E_{\text{over}} + E_{\text{under}} + E_{\text{angle}} + E_{\text{tors}}}_{\text{bonding}} \\
&+ \underbrace{E_{\text{vdWaals}} + E_{\text{Coulomb}}}_{\text{non-bonding}} + E_{\text{add.}}
\end{aligned}
\tag{2.23}
$$

The bonding terms in this equation are given by the term for the covalent bond energy E_{bond}, penalty terms for under- and over-coordination E_{over} and E_{under} to enforce a correct valency and the terms E_{angle} to include the strain from the 3-body valence angle and E_{tors} for the 4-body torsional angle. E_{vdWaals} and E_{Coulomb} denote dispersion and Coulomb contributions, which account for the non-bonding interactions. $E_{\text{add.}}$ refers to additional energy contributions, which can be added to equation 2.23 to account for the description of e.g. conjugation or hydrogen bonds.

2.3.1 Bonding Interactions

A feature of ReaxFF is the utilization of a correlation between bond length and bond order instead of fixed binding tables to determine the presence of a bond. Thus bond formation and breaking can, in addition to pairwise non-bonding Coulomb- and van-der-Waals interactions, be simulated. In ReaxFF all bonding interactions depend on the bond order, which guarantees a smooth transition between bond breaking and formation. In the following, the dependence on the bond order will be illustrated for the bond energy E_{bond} between two carbon atoms. This dependence is exemplary for the architecture of every other bond between two elements in ReaxFF.

The uncorrected bond order BO'_{ij} is calculated with equation 2.25, which contains exponential terms for a single σ- and two π-bonds. The exponential expressions approach zero for increasing bond distances r_{ij} and one when it decreases. Subsequently, the maximum bond order in this example is three:

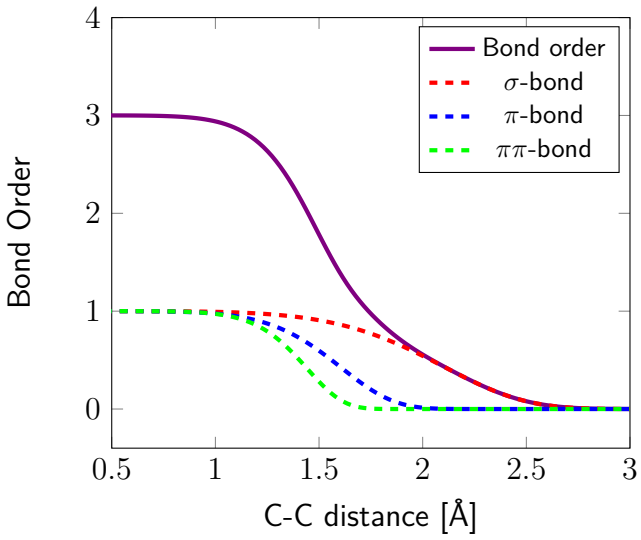

Figure 2.2. Illustration of the bond length/bond order relation exemplified for a C-C bond. Reprinted (adapted) with permission from [53] (*Copyright 2001 American Chemical Society*).

$$
\begin{aligned}
BO'_{\mathrm{ij}} &= BO^{\sigma'}_{\mathrm{ij}} + BO^{\pi'}_{\mathrm{ij}} + BO^{\pi\pi'}_{\mathrm{ij}} \\
&= \underbrace{\exp\left[p_{\mathrm{bo},1}\left(\frac{r^{\sigma}_{\mathrm{ij}}}{r_0}\right)^{p_{\mathrm{bo},2}}\right]}_{\sigma-\mathrm{bond}} + \underbrace{\exp\left[p_{\mathrm{bo},3}\left(\frac{r^{\pi}_{\mathrm{ij}}}{r_0}\right)^{p_{\mathrm{bo},4}}\right]}_{\pi-\mathrm{bond}} \\
&+ \underbrace{\exp\left[p_{\mathrm{bo},5}\left(\frac{r^{\pi\pi}_{\mathrm{ij}}}{r_0}\right)^{p_{\mathrm{bo},6}}\right]}_{\pi\pi-\mathrm{bond}}.
\end{aligned}
\tag{2.24}
$$

In this equation the parameters $p_{\mathrm{bo},1}, ...p_{\mathrm{bo},6}$ are fit parameters which contain the dependence between bond order and geometry. The calculation of the bond order however requires a correction which is given by equation 2.25:

$$
\Delta'_{\mathrm{i}} = \sum_{\mathrm{j}=1}^{n_{\mathrm{bond}}} BO'_{\mathrm{ij}} - Val_{\mathrm{i}}. \tag{2.25}
$$

Here Δ'_{i} is a measure for the deviation of the sum of the uncorrected bond orders around an atomic centre from their specific valency Val_{i}. With this correction factor,

one obtains the corrected bond order:

$$BO_{\mathrm{ij}} = BO_{\mathrm{ij}}^{'} \cdot f_1(\Delta_{\mathrm{i}}^{'}, \Delta_{\mathrm{j}}^{'}) \cdot f_4(\Delta_{\mathrm{i}}^{'}, BO_{\mathrm{ij}}^{'}) \cdot f_5(\Delta_{\mathrm{j}}^{'}, BO_{\mathrm{ij}}^{'}). \tag{2.26}$$

As a result of 2.26 one obtains a curve shape for the bond order as it is illustrated in Fig. 2.2 using the example of a C-C bond. The corrected bond order now enters terms for the specific potentials, which, despite some similarities, considerably distinguish themselves from the formulation in classical force fields. The inclusion of the bond order takes place in the same fashion as shown in equation 2.27, which is used for the calculation of the bond energy between two atoms i and j with D_{e} and $p_{\mathrm{be},1}$ as additional bonding parameters:

$$E_{\mathrm{bond,ij}} = -D_{\mathrm{e}} \cdot BO_{\mathrm{ij}} \cdot \exp[p_{\mathrm{be},1}(1 - \mathrm{BO}_{\mathrm{ij}}^{p_{\mathrm{be},1}})]. \tag{2.27}$$

Thus the contribution to the energy vanishes as soon as the bond order approaches zero, which is equivalent to the bond between the two atoms breaking. Furthermore, the formulation of the bond order ensures that there aren't any discontinuities for the energy and consequently for the calculation of the forces.

2.3.2 Non-bonding Interactions

The non-bonding contributions of the system include van der Waals and Coulomb interactions. The van der Waals term E_{vdWaals} encapsulates both repulsion at short interatomic distances and the dispersion of long-range interactions. The Coulomb term E_{Coulomb} on the other hand encompasses electrostatic and polarization effects. The non-bonding interactions are computed for every atom pair whose distance is smaller than a specified cutoff radius. To ensure a smooth energy transition, a taper correction $Tap(r_{\mathrm{ij}})$ is implemented, preventing discontinuities and facilitating a gradual decay of non-bonding interactions to zero at the cutoff boundary.

The van der Waals interactions are accounted for using a distance-corrected Morse

potential:

$$\begin{aligned} E_{\mathrm{vdW}} &= Tap(r_{\mathrm{ij}}) \cdot D_{\mathrm{ij}} \\ &\cdot \left\{ \exp\left[\alpha_{\mathrm{ij}} \cdot \left(1 - \frac{f_{13}(r_{ij})}{r_{\mathrm{vdW}}}\right)\right] - 2 \cdot \exp\left[\frac{1}{2} \cdot \alpha_{\mathrm{ij}} \cdot \left(1 - \frac{f_{13}(r_{\mathrm{ij}})}{r_{\mathrm{vDW}}}\right)\right]\right\}. \end{aligned} \tag{2.28}$$

In equation 2.29, shielded interactions are incorporated using the function f_{13} within the potential, defined as

$$f_{13}(r_{\mathrm{ij}}) = \left[r_{\mathrm{ij}}^{p_{\mathrm{vdW1}}} + \left(\frac{1}{\gamma_{\omega}}\right)^{p_{\mathrm{vdW1}}}\right]^{\frac{1}{p_{\mathrm{vdW1}}}}, \tag{2.29}$$

aiming to further mitigate excessively strong repulsive forces between bonded atoms. Here, r_{ij} denotes the interatomic distance between atoms i and j, whereas D_{ij}, α_{ij}, r_{vdW}, p_{vdW1}, and γ_{ω} represent van der Waals parameters. Similar to the treatment of van der Waals interactions, Coulomb interactions are considered for all atom pairs. To account for orbital overlap between atoms in close proximity, a shielded Coulomb potential is employed:

$$E_{\mathrm{Coulomb}} = Tap(r_{\mathrm{ij}}) \cdot \frac{1}{4\pi\epsilon_0} \cdot \frac{q_{\mathrm{i}} \cdot q_{\mathrm{j}}}{\left[r_{\mathrm{ij}}^3 + \gamma_{\mathrm{ij}}^{-3}\right]^{\frac{1}{3}}}. \tag{2.30}$$

In equation 2.30, the shielding term is represented by γ_{ij}, while q_{i} and q_{j} denote the respective charges of two atoms, i and j, which are at a distance r_{ij} from each other. In ReaxFF, the computation of the fluctuating atomic charges can be determined through methodologies such as the Electronegativity Equilibration Method (EEM) or the utilization of the atom-condensed Kohn-Sham density functional theory, approximated up to second order (ACKS2) charge equilibration scheme.

2.3.3 ReaxFF in the Multiscale Approach

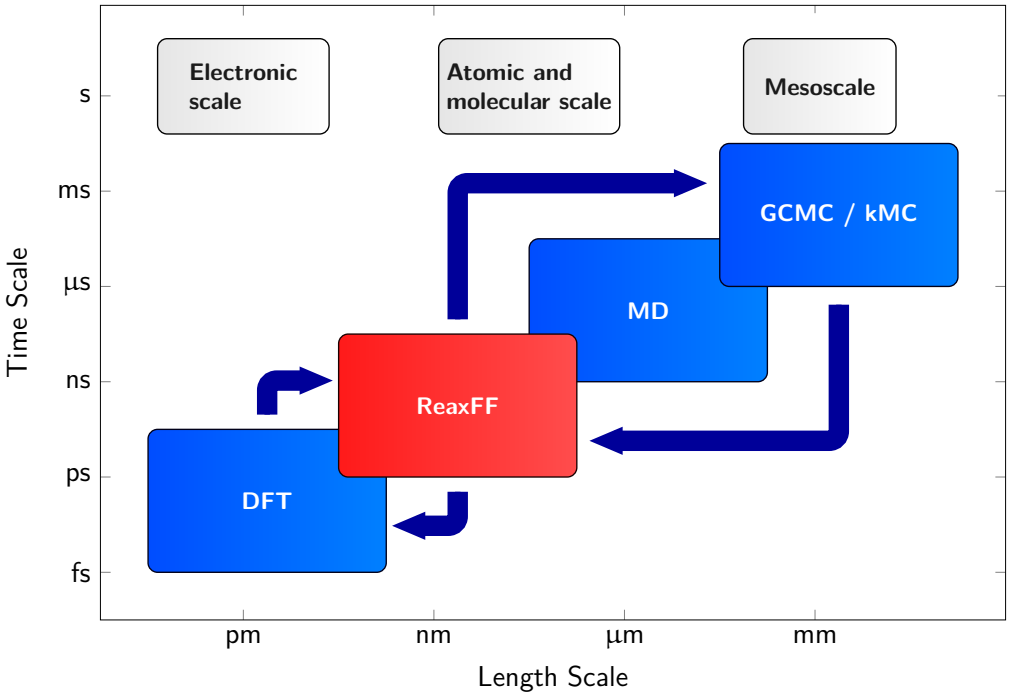

Figure 2.3. Scheme for the classification of ReaxFF in the multiscale hierarchy.

With the presented way of inserting the bond order into the various potential terms, ReaxFF is by far more accurate than its classical counterparts. Due to the possibility of bond breaking and formation, ReaxFF is moreover usable in fields, where classical force fields fail, making it a powerful tool that can sometimes even reach the accuracy of quantum mechanical methods. As a consequence, ReaxFF enables the simulation of systems which aren't manageable with quantum mechanical methods on the scale of several thousand atoms, with a quality that is nevertheless comparable to the same methods. Hence ReaxFF has the potential to bridge the gap between quantum mechanical methods and classical MD as shown in Fig. 2.3. To go a step further ReaxFF can even be implemented as the centrepiece for methods such as Grand Canonical Monte Carlo (GCMC) [65, 66] or kinetic Monte Carlo (kMC) [67], which makes simulations in the mesoscale accessible. In Fig. 2.3 it is indicated by the arrows, that a method is based on a method that lies below it in the multiscale hierarchy. A characteristic of ReaxFF for example is, that its parameters are solely optimized on

the basis of quantum mechanical calculations. By implication, the method which lies higher in the hierarchy has to be tested against the more accurate method and be able to reproduce the results to ensure a reliable quality. Because ReaxFF is the core of the presented multiscale approach, this strategy stands or falls with the quality of the reactive force field. The optimization and validation of ReaxFF is therefore inevitable and one of the main objectives in this work.

3

Theoretical studies on the initial oxidation of metallic lithium anodes

Matthias van den Borg [1, 2], Daniel Gaissmaier[1, 3, 4], Edwin Knobbe[2], Donato Fantauzzi [3, 4, 5] and Timo Jacob[1, 3, 4], *Appl. Surf. Sci.* **2021**, *555*, 149447.

Reproduced from Ref. [68] with permission from Elsevier.

Style, numbering and citations have been adapted to ensure a consistent presentation throughout the work.

[1] Institute of Electrochemistry, Ulm University, Albert-Einstein-Allee 47, D-89081 Ulm, Germany
[2] BMW Group, 80809 Munich
[3] Helmholtz-Institute Ulm (HIU) for Electrochemical Energy Storage, Helmholtzstr. 11, 89081 Ulm, Germany
[4] Karlsruhe Institute of Technology (KIT), P.O. Box 3640, 76021 Karlsruhe, Germany

3.1 Abstract

Due to their high theoretical specific capacity and their low electrochemical potential, lithium metal anodes are ideal candidates for future generations of high energy density batteries to successfully implement electric mobility on a grand scale. Unfortunately, lithium's high reactivity with atmospheric contaminations represents a high safety risk, which may limit the commercial application of metallic lithium anodes. Using the example of lithium oxidation, this work presents the formation of coordinated clusters on metallic lithium surfaces, which show striking similarities to the compound class of suboxides. It is shown, that the clusters have a decisive influence on the absorption, dissociation and diffusion on the metal surface and provide mechanistic insights for the initial reconstruction observed for lithium anodes.

3.2 Introduction

Of the many existing energy storage systems, rechargeable batteries with a metallic lithium anode are considered to be among the most promising candidates for high-energy storage, as they excel in terms of theoretical specific energies and gravimetric and volumetric densities. This is due to the extraordinarily favourable characteristics of lithium. With its low specific weight of only 0.53 $\mathrm{g\ cm^{-3}}$ and a standard electrode potential of -3.04 V, lithium is not only the lightest metal but also shows the most negative standard electrode potential of all chemical elements in the periodic table [13, 24, 25]. On this account, Li-based anodes are an essential key component of new generation devices such as all-solid-state or even Li-sulfur [69–72] and Li-air batteries [73–77], whose theoretical capacities would outperform those of graphite anodes in present lithium-ion batteries (LIBs) by up to ten times. Unfortunately, these technologies crucially depend on the reversibility and stability of the metallic lithium anode, whose application is connected with severe performance issues, that have boosted the development of the LIB technology in the first place [13, 24, 78]. Besides dendritic growth and a limited Coulumbic efficiency during the repeated deposition and stripping of lithium, several problems are posed by its chemical nature: while its extreme electropositive character is a desired property for a high voltage anode, it is also responsible for a wide variety of side reactions at the anode's interface. This is reflected in the dissociation of small, atmospheric molecules [33, 79, 80] exposed

to the clean surface and a general instability towards almost any kind of organic electrolytes [30–34, 80], which ensures that the chemical reactions at the interface are amongst the decisive factors for cycle stability. In combination with non-aqueous electrolytes, metallic lithium anodes are therefore immediately covered by a passivating solid electrolyte interphase (SEI) [25, 30–38], which protects the anode from further degradation, but is also the cause for several challenges and safety risks. Progressive electrolyte decomposition through cracks in the SEI caused by subsequent stripping and plating means a loss of active material and lowering Coulomb efficiency and may, for example, lead to high-impedance failures. Although many studies have focused solely on the degradation reactions with organic components, comparatively little attention has been spent on the interactions with the surrounding environment. It is generally known that molecules such as nitrogen, oxygen or water from the surrounding environment react with lithium in an exothermic fashion to Li_2O [43–48], Li_3N [49, 50], LiOH [46, 47] and derivates. Through the entrance of atmospheric contaminations into the battery cell, only small amounts in the electrolyte or at the anode could therefore result in a very fast corrosion of lithium metal, which would endanger the safe battery operation. The risk would apply in particular to new open storage systems such as Li-air batteries, where the metallic anode is by design close to being contaminated by O_2 and other atmospheric species [81]. Here the reactive impurities could by accident reach the anode via diffusion through the electrolyte.

Corrosion of the lithium surface significantly affects battery life, capacity and safety during production and operation. On an atomistic level, however, surprisingly little is known about the structure, composition or corrosion mechanisms of the lithium interface, since experimental methods encounter major limitations in terms of spatial, time and energetic resolution. Previous investigations on lithium oxidation are therefore almost exclusively limited to fundamental studies on the composition and occurrence of oxidised lithium species [44–46, 82]. Based on spectroscopic investigations, the formation of Li_2O_2, Li_2O and LiOH phases and the storage of oxygen has been suggested to also occur under the Li surface. However, only a few is said about the exact processes or structures on an atomic level. *Ab-initio* quantum chemistry methods, in particular density functional theory (DFT) [51, 52], have therefore emerged as a very promising approach to face the comprehension of the most fundamental atomistic mechanisms in electrochemical systems in recent times. So far, there is only a very limited selection of theoretical studies on lithium corrosion through atmospheric contaminants at an

atomistic level [83–85]. Due to restrictions in time and length scales that can be covered by a fully quantum mechanical treatment, the complexity of describing the entire corrosion process currently far exceeds the capabilities of these methods. The strength of DFT, in this case, lies in the identification of fundamental principles and mechanisms at the atomic level, the understanding of which could contribute to improving the chemical stability of metallic lithium anodes. To unravel the basic principles behind lithium oxidation, the present work summarises periodic DFT calculations on the fundamental properties of the lithium interaction with atmospheric oxygen. In the first step, the monoatomic absorption on low-index Li-surfaces was calculated, where recurring cluster-like structures were found. The dissociative absorption of molecular oxygen was then evaluated to confirm these findings and oxygen diffusion paths were evaluated to classify the kinetics for corrosion. To gain deeper insights into the initial stages of oxidation and thus possible corrosion on an atomic scale, the binding energies were determined as a function of surface coverage.

3.3 Computational details

All DFT calculations were performed using projector augmented-wave (PAW) potentials with valence states of $2s$ for lithium and $2s2p$ for oxygen as implemented in the periodic Vienna *ab initio* simulation package (VASP) [86–88]. To account for the exchange and correlation effects, we used the Bayesian error estimation functional with van der Waals correlation (BEEF-vdW) [60]. BEEF-vdW was developed using regularization and crossover point-validation methods known from machine learning. The functional developed by Wellendorf *et al.* corresponds to a semilocal approximation with an additional nonlocal correlation term, aimed at general applicability to strong, as well as to weak interactions. In our previous study [89], we were able to show that for metallic lithium, BEEF-vdW and the widely used PBE [90] functional both produce values in good agreement with experimental data. Despite the O_2 overbinding error present in DFT, however, BEEF-vdW yields a significantly improved value for the binding energy of an oxygen molecule compared to the PBE functional, as can be seen in the appendix. Although the Grimme dispersion correction [91] has improved the description of the bulk-Li_2O formation energy with the PBE functional in other works [92, 93], we did not use this approach, as it leads to a slight underestimation of the lattice constant for the bulk structure of *bcc*-lithium.

The plane wave energy cutoff was set to 400 eV and a Gaussian smearing of 0.2 eV was used. For the molecular reference, we used a smaller smearing of 0.01 eV. The metallic lithium surfaces were simulated using a supercell consisting of an eleven-layer slab for Li(100) and Li(110) and a seventeen-layer slab for Li(111), where the lowest two layers have been fixed to the calculated bulk structure of *bcc*-lithium (a=3.40 Å). The remaining surface layers and oxygen adsorbates were allowed to fully optimize their geometries until the force-convergence criterion of 0.005 eV/Å was met. Such extended slabs were found to be necessary to obtain converged results. Each supercell employed a 15 Å vacuum region normal to the surfaces. The Bader-charge [94] analysis of the adsorbed complexes was based on the total charge density, *i.e.* taking into account the electronic as well as the ionic nuclei, as implemented by Henkelman *et al.* [95]. As an additional analysis, net charges and bond orders were determined via the DDEC6 scheme by Manz *et al.* [96–98]. Binding energies were referenced to the respective gas phase molecules and calculated through

$$E_{\mathrm{bind}} = \frac{1}{N_{\mathrm{ads}}}\left[E_{\mathrm{ad}}^{\mathrm{tot}} - E_{\mathrm{slab}}^{\mathrm{clean}} - \frac{N_{\mathrm{ads}}}{2}\left(E_{\mathrm{molecule}}^{\mathrm{gas}} + E_{\mathrm{molecule}}^{\mathrm{ZPE}}\right)\right], \tag{3.1}$$

where $E_{\mathrm{ad}}^{\mathrm{tot}}$ is the total energy of the Li-surface + adsorbates, $E_{\mathrm{slab}}^{\mathrm{clean}}$ the total energy of the surface slab, N_{ads} the number of absorbed oxygen atoms, $E_{\mathrm{molecule}}^{\mathrm{gas}}$ the total energy of an O_2 gas phase molecule and $E_{\mathrm{molecule}}^{\mathrm{ZPE}}$ the zero-point energy correction, which was calculated within the harmonic approximation. The energy barriers for diffusion processes were determined using the climbing-image nudged-elastic-band method (CI-NEB) [99, 100] developed by Henkelmann with a total number of seven images. The initial diffusion pathways were created by linearly interpolating between the initial and final images, and the forces were allowed to relax to the same threshold of 0.01 eV/Å. The calculations of diffusion barriers on Li(100) were calculated on a (5x5) cell, while the coverage dependence of the binding energy was simulated on a (6x6) slab at coverages between 0.03 and 1.0 ML. The coverage was classified in terms of geometric monolayers (ML), which are defined as the ratio between the number of adsorbates and the number of substrate atoms in the top surface layer. Calculations on Li(110) were carried out on a (4x8) surface unit cell, while a (4x6) cell was used for Li(111). All calculations were performed with a $\boldsymbol{k}$-point mesh density of 0.15 $\mathrm{Å}^{-1}$ according to the scheme of Monkhorst and Pack [101]. To evaluate the thermodynamic stability of various surface structures and compositions under different environmental pressure and temperature conditions, the Gibbs free energy of adsorption $\Delta\gamma^{\mathrm{ad}}$ for

each surface phase was calculated as a function of oxygen's chemical potential $\mu^{\mathrm{gas}}_{\mathrm{molecule}}$ using

$$\Delta\gamma^{\mathrm{ad}}(T, p_{\mathrm{gas}}) = \frac{1}{A}\left[E^{\mathrm{tot}}_{\mathrm{ad}} - E^{\mathrm{clean}}_{\mathrm{slab}} - \frac{N_{\mathrm{ads}}}{2} \cdot \mu^{\mathrm{gas}}_{\mathrm{molecule}}(T, p_{\mathrm{gas}})\right]. \tag{3.2}$$

The surface area of the slab is labelled A, while the pressure and temperature of the surrounding gas-phase reservoir are denoted by T and p_{gas}, respectively. Using this atomistic thermodynamics approach [102], the surface free energy is calculated as a function of the chemical potential of the molecular species. The chemical potential itself can be determined and expressed in terms of partial pressure and temperature of the corresponding gas phase reservoir.

3.4 Results and discussion

3.4.1 Adsorption and absorption on/by lithium surfaces

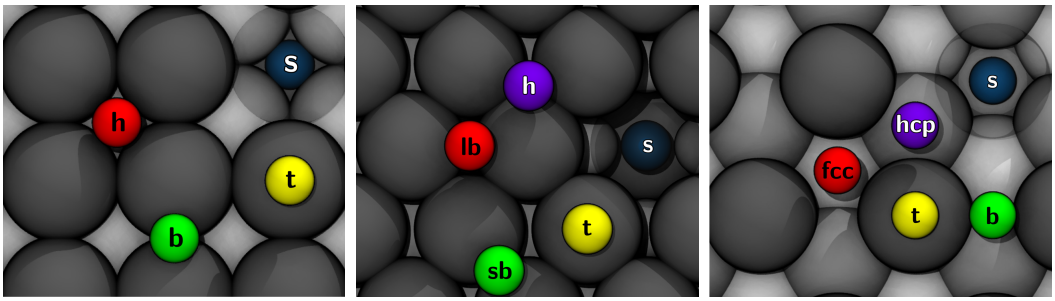

(a) Li(100) (b) Li(110) (c) Li(111)

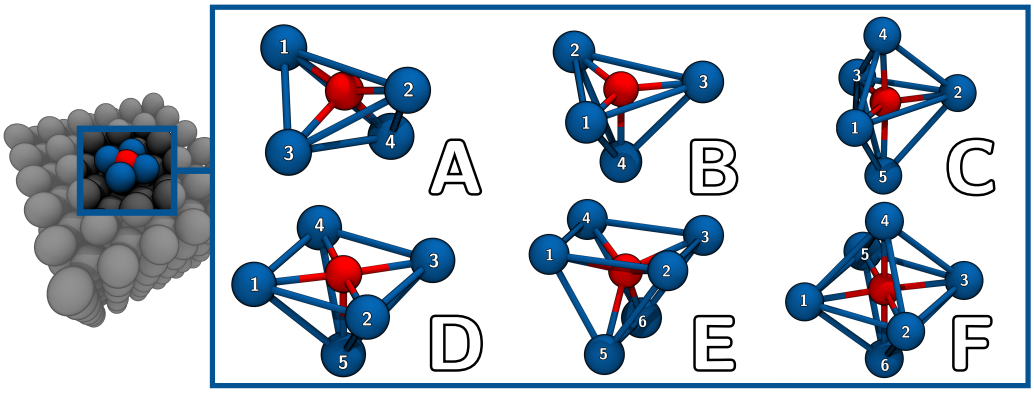

(d)

Figure 3.1. Adsorption sites on the low-index surfaces. Li(100) in **(a)** : hollow (h), bridge (b), subsurface (s) and top (t), Li(110) in **(b)**: long-bridge (lb), hollow (h), short-bridge (sb), subsurface (s) and top (t)) and Li(111) in **(c)**: hcp, fcc, bridge (b), subsurface (s) and top (t). Depending on the layer, the lithium atoms are illustrated in different shades of grey. In **(d)** an exemplary illustration of the surface structure of the Li(100) surface after monoatomic absorption and a summary of the occurring clusters. The coordinating lithium atoms are shown in blue and oxygen in red.

Table 3.1 Calculated binding energies in eV on the different surface sites shown in Fig. 3.1 (a)-(c). According to the number and geometry of the surrounding Li-atoms of the absorbates, the absorption structures were assigned to a type of cluster structure, corresponding to the ones shown in Fig. 3.1. The charge transferred to the oxygen atom during absorption was determined with the Bader and DDEC6 charge analysis and is given in e/atom. For the absorbed oxygen atoms, the respective sum of bond orders (SBO) is presented, as derived from the DDEC6 method.

(*hkl*)	Adsorption site	$E_{\mathrm{bind,O}}$	type	$Q_{\mathrm{bader,O}}$	$Q_{\mathrm{DDEC6,O}}$	$SBO_{\mathrm{DDEC6,O}}$
Li(100)	*hollow*	-5.59	**D**	-1.86	-1.32	1.97
	bridge	-5.48	**F**	-1.94	-1.29	2.14
	subsurface	-5.35	**F**	-2.07	-1.28	2.13
	top	-4.32	**D**	-1.98	-1.33	1.94
Li(110)	*long-bridge/hollow*	-5.75	**D**	-1.82	-1.32	2.05
	short-bridge	-5.28	**E**	-1.90	-1.29	2.11
	subsurface	-5.43	**F**	-1.89	-1.27	2.18
	top	-5.00	**D**	-1.84	-1.31	1.95
Li(111)	*hcp*	-5.40	**B**	-1.80	-1.46	2.02
	fcc	-5.22	**B**	-1.89	-1.38	1.91
	bridge	-5.20	**A**	-1.80	-1.43	2.01
	subsurface	-5.33	**C**	-2.00	-1.23	1.99
	top	-5.14	**F**	-1.87	-1.33	2.02

To assess the general effect of oxygen adsorption on lithium, it was examined at first how the adsorption of monoatomic oxygen influences the energetic and structural behaviour of the surface. The initial adsorption geometries were prepared by placing an oxygen atom on the high-symmetry adsorption sites of the low-index surfaces Li(100), Li(110), and Li(111), as shown in Fig. 3.1. In all cases, the structures showed remarkably high binding energies, which well reflected the extraordinarily exothermic nature of lithium oxidation. A particularly striking feature was the uptake of atomic oxygen into the surface via an absorption process, by rearranging the surface morphology through the construction of cluster-like coordination compounds (see Fig. 3.1). Depending on the surface geometry, differently coordinated structures were formed by attracting the surrounding surface atoms, whose assignment with the corresponding adsorption

sites can be found in Table 3.1. On Li(100) the absorption on the *hollow* position led to the formation of a cluster, in which the oxygen atom was present in a five-fold coordinated, square pyramidal arrangement (see clusters in Fig. 3.1). With a binding energy of -5.59 eV the Li(100)-O_{hollow} structure was the thermodynamically most favourable configuration on Li(100). The tendency to form cluster-like structures was especially evident for the absorption on the *top* position on Li(100), where the driving force to form a five-fold coordinated cluster was strong enough to tear four lithium atoms out of the surface. In Li(100)-O_{top}, the oxygen atom was in a similar square pyramidal arrangement as in Li(100)-O_{hollow}, but by 1.27 eV less stable and thus with -4.32 eV the least stable configuration on Li(100). The second most stable structure on Li(100) was the Li(100)-O_{bridge} structure with a binding energy of -5.48 eV. Here, the oxygen atom took an octahedral coordination, which was formed through the penetration of oxygen into the lithium surface. Likewise, the oxygen atom was stored in an octahedral coordination in Li(100)-$O_{\mathrm{subsurface}}$, which was by 0.13 eV less stable than Li(100)-O_{bridge}. The comparison of Li(100)-O_{hollow} and Li(100)-O_{bridge} showed, that absorption of an oxygen atom below the surface was only by 0.11 eV less favourable than on top of it. Similar tendencies were observed for both the Li(110) and Li(111) surfaces. On Li(110), absorption on the *hollow* and on the *long-bridge* position led to the formation of the same square pyramidal cluster. With -5.75 eV, the Li(110)-$O_{\mathrm{long-bridge}}$ structure had the highest binding energy of all the investigated absorption complexes. Analogous to Li(100), the Li(110)-O_{top} structure emerged by attracting four lithium atoms from the surface under the formation of a five-fold square pyramidal cluster. With -5.00 eV Li(110)-O_{top} was also the least stable structure on Li(110). Absorption into the *short-bridge* and the *subsurface* position both led to the formation of octahedral clusters, in which oxygen was located below the surface, but Li(110)-$O_{\mathrm{subsurface}}$ is 0.15 eV more stable than Li(110)-$O_{\mathrm{short-bridge}}$. On Li(110) the absorption below the surface into Li(110)-$O_{\mathrm{subsurface}}$ is thus 0.22 eV less stable than above into Li(110)-$O_{\mathrm{long-bridge}}$. On Li(111), the geometric environment enabled the formation of different coordination geometries. Through the absorption into the *hcp* and *fcc* sites, trigonal-pyramidal clusters were observed on the surface and a bipyramidal coordination geometry below the surface through absorption into the *subsurface*. The absorption into the *bridge* and the *top* position, however, resulted in a tetrahedral and a square pyramidal cluster. Of the investigated surfaces, Li(111) showed the smallest energy differences between the different absorption sites. Between the most stable Li(111)-O_{hcp} and the most unstable Li(111)-O_{top} the difference of the energy was only

0.26 eV. With regard to the absorption of an oxygen atom above in Li(111)-O_{hcp} and below the surface in Li(111)-$O_{\mathrm{subsurface}}$ the energy difference is with 0.07 eV equally small as on Li(100).

As can be seen in Table 3.1, a charge analysis of the absorption complexes with both the Bader and the DDEC6 methodology revealed, that the absorption has led to a substantial charge transfer ($Q_{\mathrm{bader,O}}$: -1.80 up to -2.07 e/atom and $Q_{\mathrm{DDEC6,O}}$: -1.23 up to -1.46 e/atom) from the surface towards the oxygen atom. Within a fully oxidised lithium system, oxygen is present as an oxide ion (O^{2-}) and is embedded in the ordered and stable antifluorite Li_2O salt. Using the Bader and DDEC6 methods, a net charge of -1.60 and -1.61 e/atom was determined for the oxide ion in bulk-Li_2O. Consequently, the amount of charge transferred to the oxygen during absorption tends to be close to the charge oxygen would carry in the ionic Li_2O phase. Due to the low coverage, however, the oxygen atoms in our calculations are by design in a metal-rich environment. In relation to the Li_2O phase, the coordinating lithium atoms are therefore present in abundance. Formally, the absorption complexes thus can be classified as suboxides, which are characterised by an excess of the more electropositive element (in this case lithium) with respect to the charge of the oxide ion [103]. Suboxides are therefore also often referred to as metal-rich compounds. So far the formation of suboxides has yet not been observed for lithium, and the formation of suboxides in alkali metals was experimentally only measured for the heavier elements rubidium and caesium. Interestingly enough, the octahedrally coordinated oxygen of lithium in our calculations is isostructural to the experimentally characterised building blocks of metal-rich rubidium and caesium suboxides [103–108]. With respect to LiO clusters as isolated compounds, there is a wide range of theoretical studies of stoichiometric [109, 110] and metal-rich clusters [111–114]. Using Hartree-Fock, MP-perturbation theory and DFT calculations, these studies examined the structure and electronic properties of the clusters as a function of lithium content. While the work of Simons *et al.* [114] solely focused on the Li_3O species, the tetrahedral, square-pyramidal and octahedral coordination was found to be a recurrent structural element of the most stable oxygen clusters in all studies on metal-rich compounds. Likewise to this work, the study of metal-rich, suboxidic clusters of Noguera *et al.* [111] also identified a coordination of six as the highest for oxygen. Experimentally, the existence of isolated, metal-rich LiO clusters has been proven using high-temperature mass spectrometry [115, 116]. In addition to the net charges, we have investigated the bond orders, in

order to classify the nature of the Li-O bond on the surfaces. As can be seen in Table 3.1, an examination of the sum of bond orders (SBO) via the DDEC6 method revealed in all cases substantial SBOs for the oxygen atoms, which range from 1.91 to 2.18 (in comparison, the SBO for oxygen in bulk-Li_2O amounts to 1.49). In connection with the high oxygen net charges, the character of the Li-O bonds in the absorption complexes can therefore be classified between a polar covalent and an ionic bond.

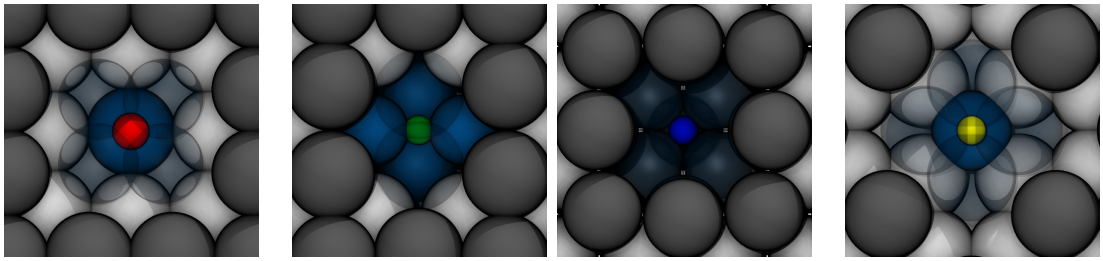

(a) hollow (h) (b) bridge (b) (c) subsurface (s) (d) top (t)

Figure 3.2. Surface structures of absorbed oxygen on Li(100) on the respective adsorption sites. For illustration purposes the coordinating lithium atoms are shown in blue and oxygen is represented with the same colour code from Fig 3.1.

As the formation of suboxidic clusters seems to be a general phenomenon on all investigated surfaces, the following work will focus on the oxygen absorption on the most stable Li(100) surface, to further demonstrate the effect of the formation of clusters on lithium surfaces. Since the following investigations thus refer to the coordination structures formed on the Li(100) surface, the structures on the surface are shown for illustration in Fig. 3.2.

3.4.2 Dissociative adsorption/absorption of O_2

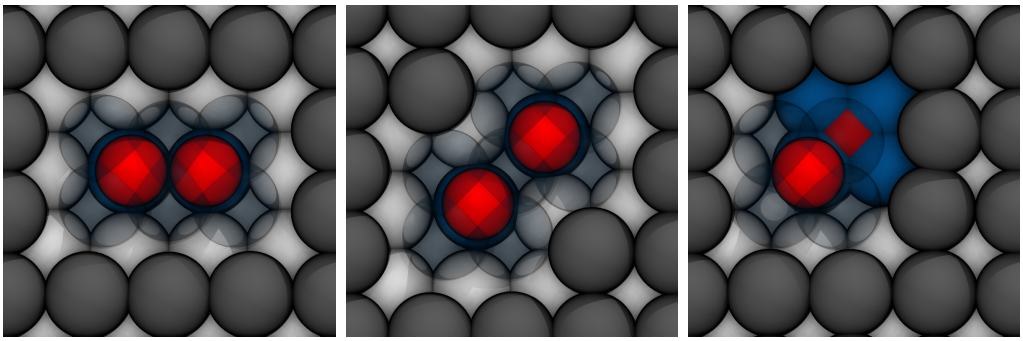

(a) h1h2 (b) h1h3 (c) h1s1

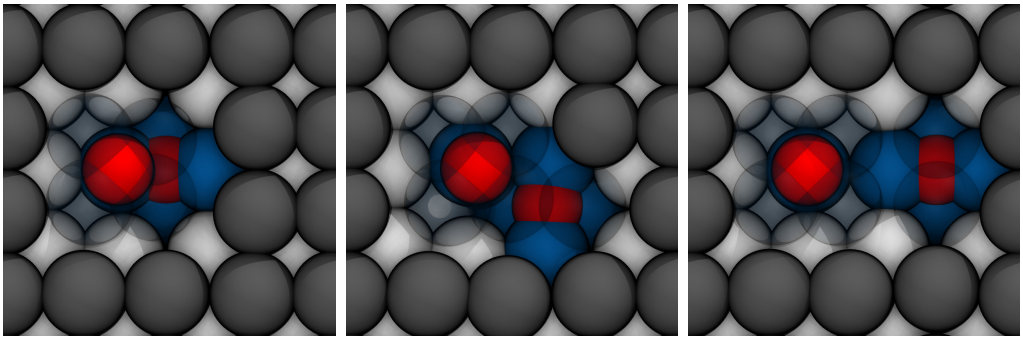

(d) h1b1 (e) h1b2 (f) h1b3

Figure 3.3. Absorption structures of dissociated O_2 on Li(100). The molecular oxygen dissociated in structures in which it was present in a combination of the observed clusters from Fig. 3.1. The labelling of the structures refers to the corresponding adsorption sites on Li(100).

In agreement with the indication of previous experimental [45, 48] and theoretical studies [83] on the absorption of molecular oxygen, our results show that O_2 is not stable in the presence of the metallic lithium surface. Instead, a dissociation of the molecule takes place under the formation of the structures shown in Fig. 3.3. Analyzing the features shows that the compounds dissociated into the already observed coordinations and that the oxygen molecule thus adopts a combination of the different absorption structures discussed above. Noticeable was the simple storage of oxygen in one of the underground *bridge* and *subsurface* absorption sites, which was observed for several initial configurations. The most stable structures of the complexes formed were the *h1h2* shown in Fig. 3.3 (a), consisting of two square planar *hollow*-complexes linked

Table 3.2 Binding energies per atom $E_{\mathrm{bind,O}}$ on the Li(100) surface. The energies are referenced to molecular oxygen in the gas phase and are reported in eV.

Configuration	h1h2	h1h3	h1s1	h1b1	h1b2	h1b3
$E_{\mathrm{bind,O}}$ (eV)	-5.52	-5.41	-5.47	-5.33	-5.45	-5.51

by two lithium atoms at the surface, as well as the *h1b3*, which is simply a combination of a *hollow* and an octahedral *bridge* complex. The energetic degeneracy of these two structures and a comparison of the binding energies listed in Table 3.2 shows that the neighbourhood of the complexes to each other can generally influence the way oxygen absorbs into lithium. While it has already become clear with monoatomic absorption that the difference in stability between the absorption site on and below the surface is marginal, it has been shown through the absorption of molecular O_2 that the neighbourhood of the clusters to each other can even influence the stability in such a way that absorption below the surface becomes energetically more stable.

3.4.3 Diffusion of absorbates

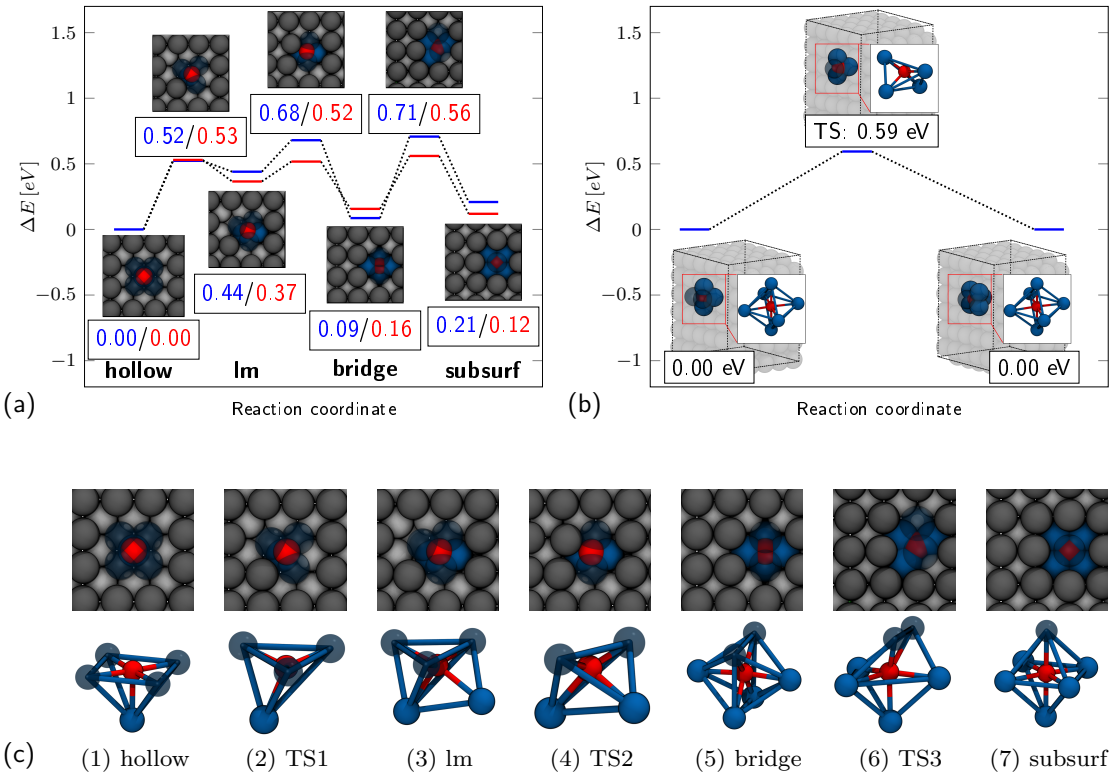

Figure 3.4. Energy profiles for the surface and bulk diffusion of oxygen obtained using NEB calculations. The energy profile in **(a)** shows the diffusion from a *hollow* site to a neighbouring *bridge* site via an intermediate local minima (*lm*), followed by a diffusion to an adjacent *subsurface* position on the Li(100) surface. The blue path represents the monoatomic path, while the red path represents the equivalent diffusion from structure *h1h2* to *h1s1* by passing *h1b2* from Fig. 3.3. The framed values indicate the relative energy related to the most stable *hollow* (and *h1h2*) structure in eV. The diffusion profile for an oxygen atom through the bulk-Li(bcc) structure is shown in **(b)**. The framed values indicate the relative energy in eV related to the most stable structure. The diffusion takes place from a position in the bulk material in which oxygen is octahedrally coordinated via a tetrahedral transition state to equivalent octahedral coordination. Shown are the structures of the octahedrally coordinated initial and final structure, as well as the tetrahedral transition state. In **(c)** the surface sections and corresponding clusters refer to the structures illustrated in the diffusion profile for the monoatomic surface diffusion. For illustration, the coordinating lithium atoms at the surface are depicted transparently in the clusters as well.

Our previous studies on the monoatomic absorption at high symmetrical sites have proven that absorption into subsurface sites often has similar energies to absorption on top of the surface planes. From a thermodynamic point of view, this would allow the storage of adatoms under the lithium surface and perhaps even in the bulk material. Calculations of the dissociative absorption of molecular oxygen also suggested that these absorption sites are easily accessible. To enable a kinetic evaluation of the embedding of oxygen under the surface, the energy barriers for the diffusion of the adatom between the *hollow*, *bridge* and *subsurface* positions were determined. Energy profiles for the monoatomic transitions are shown in blue in Fig. 3.4a. For comparison an energy profile for the equivalent transition of the molecular structures shown in Fig. 3.3 from *h1h2* to *h1b2* towards *h1s1* is also presented in red. In all cases, the energies of the local minima and transition states are referred to the energy of the most stable *hollow* absorption complex, or the *h1h2* structure in the case of molecular diffusion. In both cases, diffusion of oxygen between the absorption sites is accompanied by restructuring of the lithium surface around the adatom. This is because the diffusion of oxygen on the metallic surface takes place within a coordination shell of lithium atoms. To move from one minimum to the next, a portion of the coordinating lithium atoms are entrained until the bond to them breaks and a new cluster is formed with other lithium atoms. Thus, further coordination structures are also formed for the transition states along the respective diffusion processes. The ease of the restructuring can be most likely attributed to the comparatively small cohesive energy and low self-diffusion barriers of lithium [89, 117].

As shown in Table 3.3 the movement of the absorbed oxygen atom is in all cases associated with relatively low diffusion barriers. The transition from the *hollow* position to the *bridge* position takes place by passing the 0.44 eV less stable local minima (*lm*) shown in Fig. 3.4c (3) in which the oxygen is present in a fivefold coordinated fashion. Here, the diffusion follows a path via a fourfold coordinated distorted tetrahedral transition state, shown in Fig. 3.4c (2), that lies 0.52 eV above the *hollow* site. From an energetic viewpoint, the *lm*-structure is unstable, as both forward and reverse processes are associated with low barriers so that the oxygen atom can penetrate the octahedrally coordinated *bridge* positions via the tetrahedral transition state shown in Fig. 3.4c (4), that lies 0.24 eV above the *lm*-structure. The barrier for the reverse process to the *hollow* site is with 0.08 eV even lower. Starting from the *bridge* position, oxygen can reach the octahedrally coordinated *subsurface* position

through a sixfold coordinated transition state, that energetically lies 0.62 eV above the *bridge* configuration. The insertion into the *subsurface* via the *bridge* position was also determined as the prevailing process during the calculation of the reaction profile for direct insertion starting from the *hollow* position. As the barriers for the respective reverse processes are in a similarly low order of magnitude, this supports the assumption of high oxygen mobility. In addition, the energy profile suggests a relatively low hindrance for oxygen to enter the lithium material. We therefore also investigated the diffusion into the bulk material. Within the *bcc* bulk structure, oxygen can be stored in a sixfold coordinated octahedron, which is the periodic continuation of the *subsurface* absorption site. With a barrier of 0.59 eV between these states oxygen is comparatively mobile in the bulk material as it is on the surface. The transition state is again surrounded by four lithium atoms and assumes a tetrahedron-like geometry.

Table 3.3 ΔE_{for} and ΔE_{back} diffusion barriers for the respective forward and backward diffusion processes in eV.

Process	Type	ΔE_{for}	ΔE_{back}
hollow $\rightarrow$ lm	h $\rightarrow$ lm	0.52	0.08
	h1h2 $\rightarrow$ lm	0.53	0.16
lm $\rightarrow$ bridge	lm $\rightarrow$ b	0.24	0.59
	lm $\rightarrow$ h1b1	0.15	0.36
bridge $\rightarrow$ subsurf	b $\rightarrow$ s	0.62	0.50
	h1b2 $\rightarrow$ h1s1	0.40	0.44
bulk diffusion	monoatomic	0.59	0.59

3.4.4 Coverage-dependent absorption

To evaluate the coverage dependency, symmetrical arrangements of the *hollow*, *bridge* and *subsurface* absorption sites with coverages between 0.03 and 1.00 ML have been optimised. Analogous to the monoatomic absorption, the formation of clusters also occurred for higher coverages up to 0.50 ML for the *hollow* and *subsurface* arrangements. When the oxygen coverage reached a limit of 0.50 ML the surface structure, which so far consisted of a well-ordered arrangement of clusters, switched over to a less sorted, amorphous-like arrangement. A schematic illustration of this behaviour is shown in Fig. A.3, where the reorganisation process on the surface is portrayed for coverages of

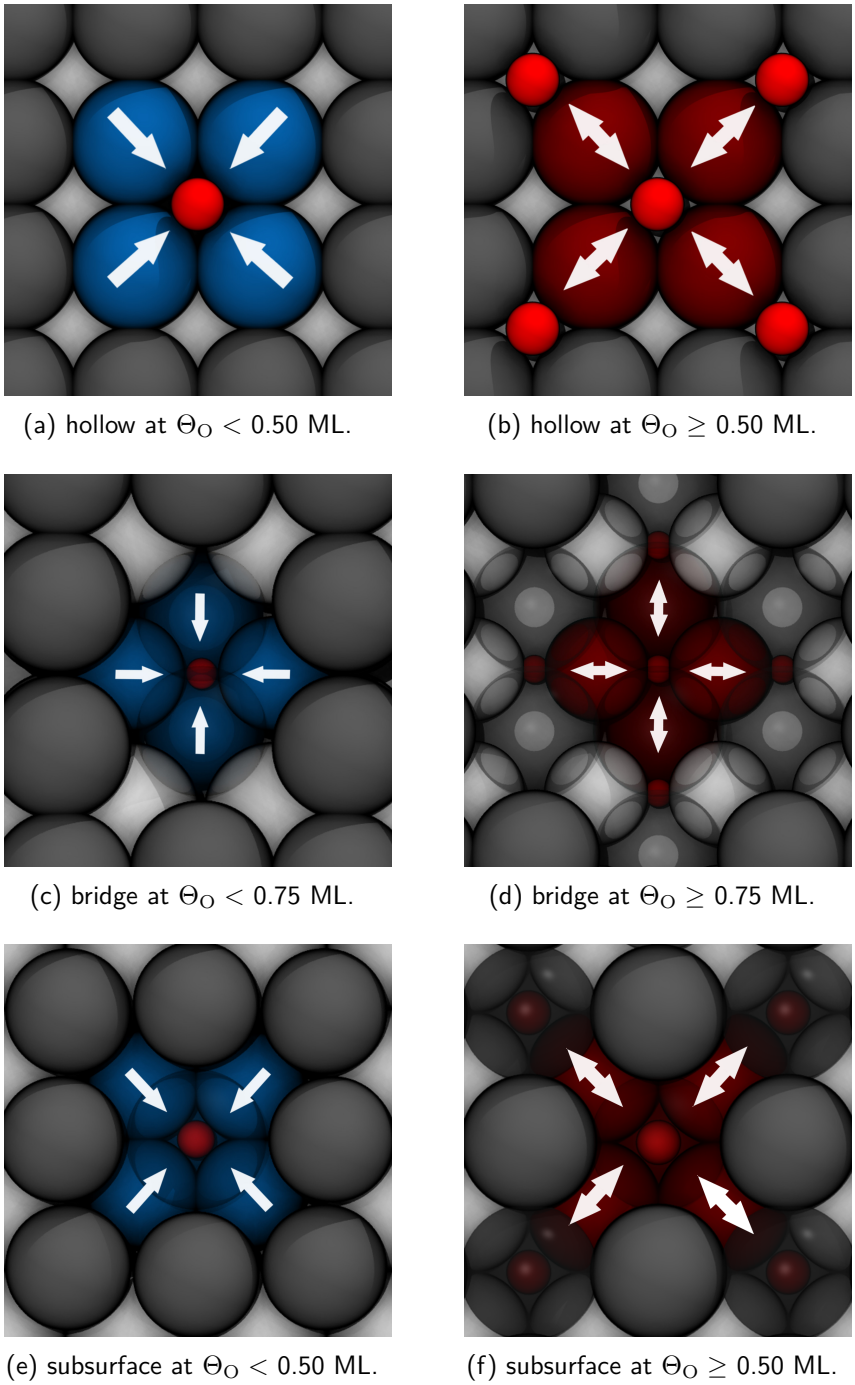

(a) hollow at $\Theta_O < 0.50$ ML.

(b) hollow at $\Theta_O \geq 0.50$ ML.

(c) bridge at $\Theta_O < 0.75$ ML.

(d) bridge at $\Theta_O \geq 0.75$ ML.

(e) subsurface at $\Theta_O < 0.50$ ML.

(f) subsurface at $\Theta_O \geq 0.50$ ML.

Figure 3.5. Schematic illustration of cluster formation on Li(100), which caused rearrangements on the surface at higher coverages. The blue symbols represent the attraction of Li atoms towards oxygen at lower coverages, leading to the formation of an ordered arrangement of clusters. The red symbols depict the attraction towards several oxygen atoms at higher coverages, which leads to a reorganisation of the surface.

Table 3.4 Binding energies per atom $E_{\mathrm{bind,O}}$ on the Li(100) surface as a function of the oxygen coverage Θ_{O} in monolayers (ML) for different arrangements of the high-symmetry adsorption sites. The energies are referenced to molecular O_2 in gas phase and are reported in eV.

Θ_{O} (ML)	$E_{\mathrm{bind,O}}$ (eV)		
	hollow	*bridge*	*subsurface*
0.03	-5.59	-5.48	-5.35
0.11	-5.59	-5.46	-5.34
0.25	-5.57	-5.40	-5.30
0.50	-5.37	-5.32	-5.28
0.75	-5.36	-5.25	-5.37
1.00	-5.38	-5.39	-5.42

0.11 ML and 0.50 ML, respectively. Since the absorption into the Li(100)'s *hollow* site involves the formation of the surface cluster shown in Fig. 3.1, the four surrounding lithium atoms at the surface are needed to enable the generation of a square pyramidal *hollow*-structure. At a coverage of 0.50 ML, too few lithium atoms are, however, available to form a well-ordered array of clusters, thus promoting a reorganisation of the Li(100) clusters to the already mentioned amorphous-like arrangement. In case of the *bridge* structures it was possible that separate clusters could form even at 0.50 ML due to the geometry of Li(100). Although the ordered arrangement is preserved in the case of the *bridge* structures, a continuous decrease of the binding energy can be observed with increasing coverage. This may be attributed to the fact that the number of suboxidic clusters facing each other increases with the coverage. Consequently, the interaction between the coordinating lithium atoms of different clusters decreases, as each oxygen centre attracts its surrounding lithium atoms. The destabilization due to the decrease of the cluster interaction is also in agreement with the stronger decrease of the binding energies of the *bridge* structures, since in principle each of the eight coordinating lithium atoms can face another cluster. In the case of the *subsurface* and *hollow* structures, only four lithium atoms face another cluster.

At 0.75 ML there was too little lithium to form separate octahedral coordinations on the *bridge* structure. Instead of amorphous arrangements, however, the *bridge* structures were transformed into a comparably ordered combination of tetrahedral and octahedral clusters. With -5.25 eV per oxygen atom, this structure has the lowest binding energy of the investigated geometries, since the tetrahedrally coordinated

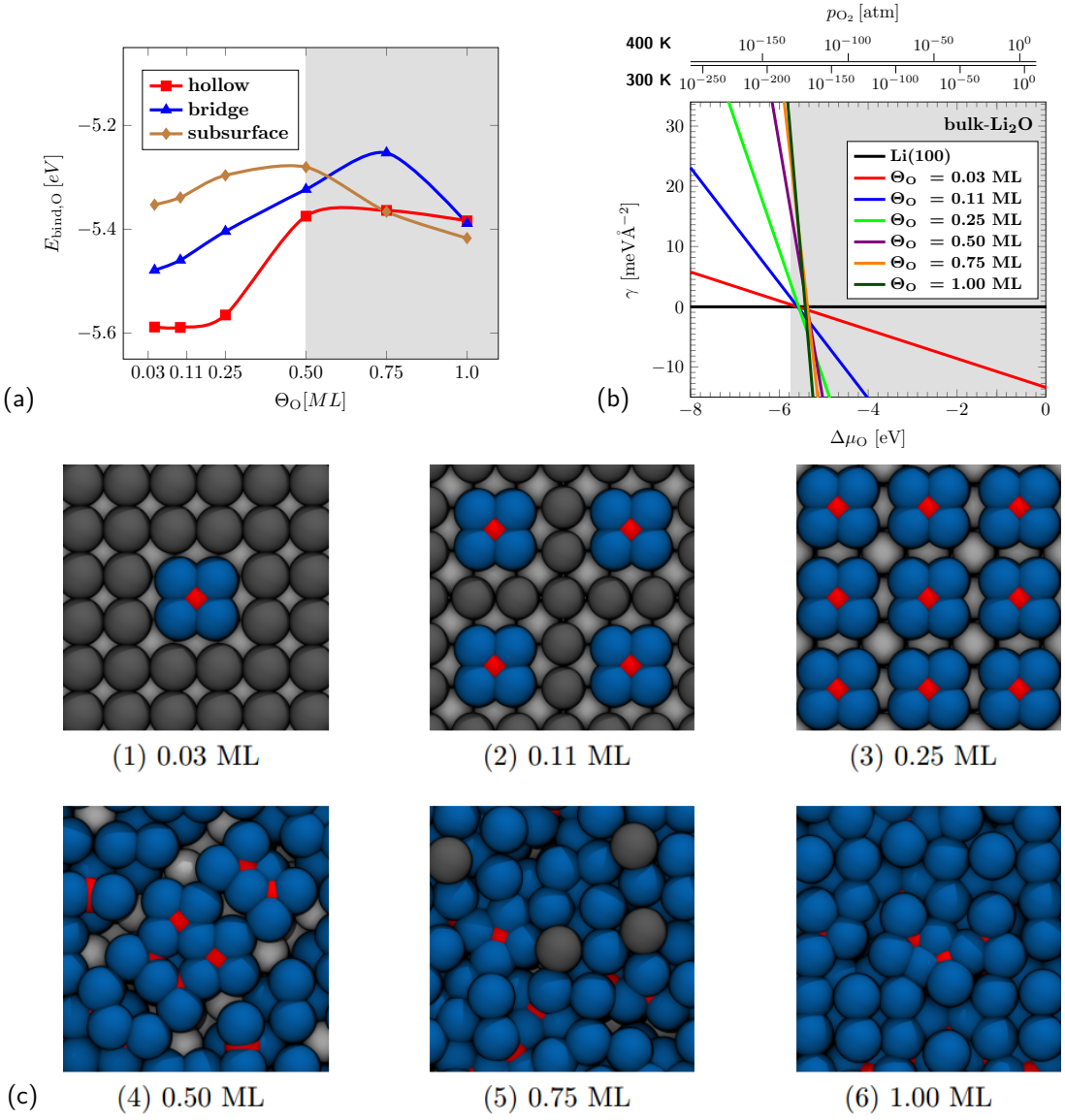

Figure 3.6. Binding energies per oxygen atom $E_{\mathrm{bind,O}}$ in eV as a function of the oxygen coverage Θ_O shown in **(a)**. The grey area represents the range, where a strong reorganisation of the Li(100) surface structure to an amorphous arrangement was observed. In **(b)** a phase diagram for the surface oxidation of Li(100) as a function of the oxygen chemical potential is shown. For fixed temperatures of 300 K and 400 K, the chemical potential has been translated to the corresponding pressures. The grey area resembles the oxygen-rich environment, where the Li_2O bulk oxide results as the most stable phase. In **(c)** sections of the most stable Li(100) surfaces at different oxygen coverages Θ_O are shown.

clusters are less stable than the octahedrally coordinated ones. As can be seen in Table A.2 the binding energy remained relatively constant up to a coverage of 0.11 ML and in the case of *hollow* structures even up to 0.25 ML. Starting from there, the influence of coverage became noticeable as the binding energy decreased until coverages were reached, where reorganisation of the lithium surface took place. As a result, the structures can no longer be assigned to their original absorption locations. Through the rearrangement, the initial *subsurface* structures showed the highest stability at coverages of 0.75 and 1.00 ML of the investigated structures as shown in Fig. a. To be able to classify the stability depending on the temperature and pressure of the surrounding oxygen atmosphere, the surface free energy of the considered phases was calculated as a function of the chemical potential of oxygen, using equation 3.2. The results are presented in Fig. b. As the oxygen chemical potential can be expressed in terms of temperature and partial pressure of oxygen, this allows the comparison of relative stabilities of the different absorption structures for environmental conditions. In this work, the variation of the chemical potential is associated with different partial pressures at temperatures of 300 K and 400 K, respectively, which is displayed in the pressure scales above the phase diagrams. Higher temperatures were not taken into account, since metallic lithium has a melting point of 453.69 K [118]. Under these circumstances, pure lithium surfaces (from a thermodynamic point of view) could be realized only at very low pressures. Of the considered structures, a coverage of 1.00 ML was the thermodynamically most stable coverage at some oxygen chemical potential between 0.00 and -5.30 eV. At lower chemical potentials up to -5.40 eV a coverage with 0.25 ML was more stable. From here the two lowest coverages of 0.11 ML and 0.03 ML had very narrow stability windows. Up to a chemical potential of -5.59 eV, the 0.11 ML coverage was more stable. A lower coverage of 0.03 ML was thermodynamically only stable down to a chemical potential of -5.59 eV, after which the pure Li(100) surface is thermodynamically preferred. Considering lithium oxide phases, however, shows that the investigated surfaces were all in the stability range of bulk-Li_2O. Taking this into account, the surface coverages must therefore be classified as metastable. An analogous examination of the coverage-dependent oxygen absorption on the second most stable Li(110) surface in the Supporting Information demonstrates that both the rearrangement of the surface structure, as well as the metastability of the suboxidic clusters towards bulk-Li_2O are phenomenons independent of the respective surface termination.

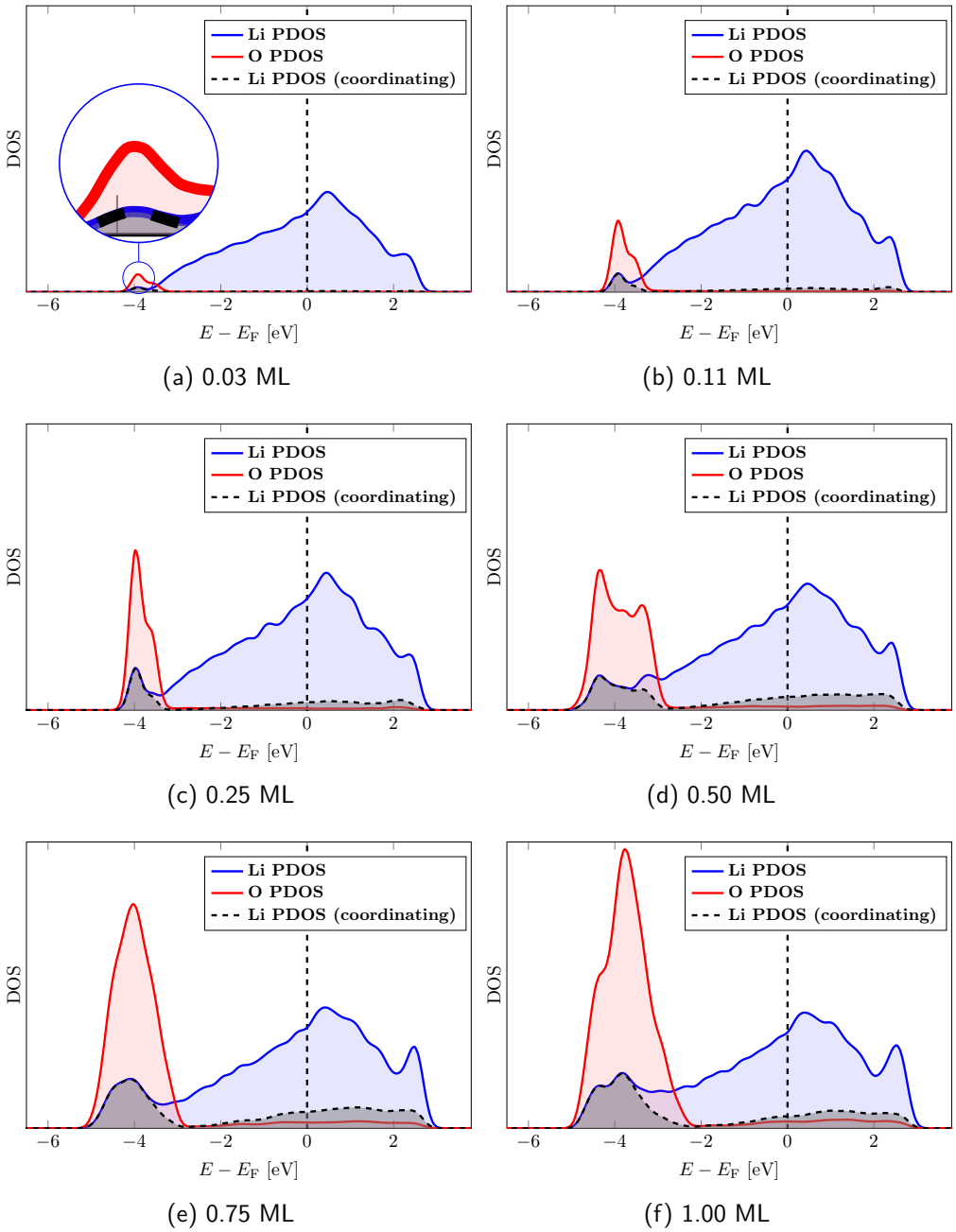

(a) 0.03 ML (b) 0.11 ML

(c) 0.25 ML (d) 0.50 ML

(e) 0.75 ML (f) 1.00 ML

Figure 3.7. Projected density of states (PDOS) for the most stable Li(100) absorption structures at different oxygen coverages Θ_O. Shown are the averaged PDOS of all lithium (blue) and oxygen (red) atoms. The states that belong to a lithium atom coordinating an oxygen atom are represented by a black dashed line.

It is important to emphasise that the phase diagram is only a statement about the thermodynamic stability and offers no possibility of describing the kinetics of the respective phase transitions. According to this, the oxide layer formed could, for example, protect metallic lithium from further corrosion. Since the diffusion barriers of oxygen within the bulk material are, however, similarly low as on the surface, it is more likely that the layers formed in our simulations do not protect against oxidation, as oxygen can easily diffuse into the bulk material. This is in accordance with results of XPS measurements of different groups [45, 82] reporting on difficulties for oxygen removal due to lithium's high reactivity.

From the projected density of states (PDOS) in Fig. 3.7 it can be seen, that the absorption of oxygen resulted in the hybridization with the coordinating lithium atoms, as their states perfectly overlap with those of oxygen. At a coverage of 0.03 ML, the PDOS implies that the coordinating lithium atoms mainly interact with the oxygen absorbate, as can be seen in Fig. 3.7a. In contrast to the residual surface, the coordinating lithium atoms do not show any metallic behaviour at low coverage, thus further indicating that the clusters are delimitable surface compounds. As can be seen in Fig. 3.7b - 3.7f, the clusters start to show a metallic character at higher coverages. This can be attributed to the suboxidic clusters increasingly getting into contact with metallic lithium as well as other clusters at higher coverages. The suboxidic surfaces thus show a fundamentally different nature, when compared to the non-metallic, insulating surfaces of Li_2O [119] and are therefore associated with a substantially different surface reactivity. In a combined theoretical and experimental study Etxebarria *et al.* already reported on the appearance of metallic surface states on top of insulating subsurface regions [84]. Here the authors postulated that the metallic surface states sustain a progressive reduction of oxygen, as they are electronically coupled with the metallic lithium, which in this case serves as an electron reservoir. It is further proposed that oxidation continues until the metallic surface states are separated from the metallic lithium by a sufficiently thick, electronically insulating Li_2O layer. This theory is supported by our results, which suggest that Li_2O must form for thermodynamic reasons from the suboxidic clusters.

Based on the low diffusion barriers in the bulk material and our insights from the phase diagram, it is therefore to be expected that the initial oxidation of lithium in a pure oxygen atmosphere can take place almost unhindered and that the oxidation of pure metallic lithium is inevitable. In this study, however, only the formation of suboxide-like

structures with a maximum coordination of six lithium was observed, whereas the oxygen in Li_2O must have a coordination of eight lithium atoms. At higher oxygen concentrations, it is therefore to be expected that larger rearrangements will have to take place from the amorphous arrangement of suboxides into the oxide.

3.5 Conclusions

Using periodic density functional theory, we studied the basic mechanisms of lithium oxidation. Simulating monoatomic absorption of oxygen on low-index Li(100), Li(110) and Li(111) surfaces implies the formation of coordinated cluster structures, whose formation is associated with a high negative charge transfer from the lithium surface to the absorbate. Here, oxygen has a negative charge, which is of comparable order of magnitude as the oxide ion in bulk-Li_2O. In relation to bulk-Li_2O, there is an excess of lithium on the metallic surface. Thus, the cluster structures can be identified as metal-rich compounds that show structural similarities with suboxides of the heavier alkali metals rubidium and caesium. A comparison of the binding energies on the highly symmetrical adsorption sites on and below the surface has shown that absorption of oxygen below the surface is similarly favourable than on the surface from a thermodynamic point of view. The formation and significance of the cluster structures could also be observed in the molecular absorption of O_2, which dissociated into a combination of the corresponding adsorption sites. Interestingly enough, with several initial structures, the oxygen molecules could already dissociate into the similarly stable *subsurface* positions during geometry optimizations, which already indicated a low energetic barrier for oxygen diffusion. These low barriers were also found in NEB calculations of atomic oxygen on lithium, which took place in coordination spheres of lithium via the fracture and formation of lithium/oxygen bonds. The diffusion of oxygen between the highly symmetrical adsorption sites on Li(100) supports the assumption that the penetration of oxygen into the lithium surface is accompanied by low diffusion barriers. Likewise, the oxygen diffusion through the bulk material is accompanied by low barriers. To assess coverage dependence, higher coverages of oxygen (up to 1 ML) on the *hollow*, *bridge* and *subsurface* sites have been calculated. In all cases the propulsion to form the clusters induced larger rearrangements, which always occurred, when not enough lithium atoms were available at the surface, to form an ordered arrangement of cluster structures with the absorbing oxygen atoms. The rearrangement of the lithium surface,

therefore, led to disordered structures in which the oxygen was still able to form the clusters despite the lithium deficiency at the surface. A thermodynamic assessment of the occurrence of the surface structures via a phase diagram has shown that the oxidised surfaces are energetically more stable than the pure lithium surface up to extremely low pressures, which would be experimentally difficult to achieve. This behaviour would qualitatively conform with the XPS experiments by Jaegermann *et al.* who, despite sputtering, have detected a small amount of oxygen remaining on the lithium surface [82]. Nevertheless, the surfaces must be regarded as metastable structures, since the lithium bulk oxide is thermodynamically more stable over the entire range of chemical potentials. In connection with the low diffusion barriers and the stable *subsurface* locations, it is therefore likely that oxygen will further penetrate the lithium surface. Even with comparatively low coverages, a slight restructuring of the surface could be observed. In agreement with the findings by Etxebarria *et al.*, who proposed the sustainment of oxidation via metallic surface states [84], the suboxidic clusters thus take on the role of reaction mediators for lithium oxidation. With further oxidation, the coordinated oxygen, which in our simulations had a coordination shell of a maximum of six lithium atoms, must reach eight to form the environment for bulk-Li_2O. Since (from a thermodynamic viewpoint) lithium oxide should form, the question arises, which processes lead to the formation of this structure. A phase transformation of the suboxides into Li_2O, however, will exceed the capacities of a conventional AIMD due to time and length scale limitations. While transformation barriers at the surface are rather difficult to capture due to the amorphous character of the suboxidic surfaces, an isolated consideration of the molecular clusters on the other hand is probably insufficient as it does not necessarily reflect the complex interactions of the clusters at the surface. Furthermore, the question arises, of which influence an electrolyte has on the relative stability of the cluster structures, since this work only considers the oxidation of metallic lithium in contact with the gas phase. In general, the suboxidic clusters can also occur below the surface, as well as in the bulk material, where the solvent has little to no influence. Although the phenomenon of suboxides thus appears to occur independently of solvent effects, the choice of the electrolyte in a battery will have a significant influence on the surface morphology. An investigation of the lithium oxidation in contact with an electrolyte should, however, be performed with an explicit solvent, since the solvent itself is involved in the degradation of the metallic lithium surfaces.

These questions, however, exceed by far the time and length scales which can be captured with density functional theory. For a realistic description of the transition from the initial absorption structures to the fully oxidised lithium, other methods, such as reactive force fields, must be used to capture these phenomena.

Acknowledgements

This work contributes to the research performed at CELEST (Center for Electrochemical Energy Storage Ulm-Karlsruhe) and was funded by the German Research Foundation (DFG) under Project ID 390874152 (POLiS Cluster of Excellence). Further, computational resources were provided by the state of Baden-Württemberg through bwHPC and the German Science Foundation (DFG) under Grant No. INST 40/467-1 FUGG.

4

A first principle study on the initial nitride formation on lithium metal

Matthias van den Borg [1, 2], Daniel Gaissmaier[1, 3, 4], Edwin Knobbe[2] and Timo Jacob[1, 3, 4]

To be submitted.

[1] Institute of Electrochemistry, Ulm University, Albert-Einstein-Allee 47, D-89081 Ulm, Germany
[2] BMW Group, 80809 Munich
[3] Helmholtz-Institute Ulm (HIU) for Electrochemical Energy Storage, Helmholtzstr. 11, 89081 Ulm, Germany
[4] Karlsruhe Institute of Technology (KIT), P.O. Box 3640, 76021 Karlsruhe, Germany

4.1 Abstract

For lithium-based batteries, the formation of lithium nitride is a crucial phenomenon, which influences important properties of the anode interface. In this study, we performed periodic DFT calculations on the interaction of metallic lithium with monatomic and molecular nitrogen. Our simulations show, that nitrogen forms cluster-like structures on the lithium surface in both its atomic and molecular state. Here, energetic and structural considerations indicated in both cases tendencies of nitrogen to migrate under the lithium surface. Our energy profile for the diffusion and dissociation of molecular nitrogen shows, that nitrogen possesses moderate diffusion barriers for the migration into the material. In accordance with experimental observations, our results suggest a dissociation of molecular nitrogen into metallic lithium, whereby the dissociation barrier under the surface is significantly lower than at the surface.

4.2 Introduction

Among the alkali metals, nitride chemistry is dominated by lithium nitride, a compound that has long attracted much attention due to its interesting physical and chemical properties [120, 121] and its application in different fields [122–125]. In contrast to sodium nitride [126–128] and potassium nitride [129], which are considered to be extremely unstable, and nitrides of heavier alkali metals (whose existence is generally debatable) lithium is the only alkali metal that forms stable nitrides. The most stable structure of lithium nitride under standard conditions is referred to as the α-Li_3N phase. The first successful efforts to characterize the structure of α-Li_3N were already made in the 1930s through single crystal X-ray diffraction by Zintl and Brauer [130], whose findings were later affirmed by Rabenau and Schulz [131] in 1976, who determined a *P6/mmm* space group and confirmed the hexagonal symmetry. On an atomic scale, lithium nitride is composed of an alternating arrangement of pure lithium layers and planar, graphite-like lithium hexagons with nitrogen in their centre [125, 131]. In the third dimension (along the *c*-axis), the layers are connected by lithium from the pure lithium layer above and below each nitrogen centre of the NLi_6 hexagons. Consequently, each nitrogen atom is in a hexagonal bipyramidal coordination geometry in which it is surrounded by a total of eight lithium atoms. Monocrystalline α-Li_3N is particularly known for its high ionic conductivity for lithium ions, caused by defects within the planar

Li_2N layers (at room temperature in the magnitude of $10^{-4}\ \Omega^{-1}\mathrm{cm}^{-1}$) [120, 121]. Owing to its high conductivity, monocrystalline lithium nitride was therefore used in battery research as one of the first solid-state electrolytes [122]. In addition to the α-Li_3N phase, there is also evidence for two further phases at increased pressures, namely the β-Li_3N phase in the *P6$_3$/mmc* group at $\sim$ 0.5 GPa, and the γ-Li_3N phase in the $Fm\bar{3}m$ group at $\sim$ 40 GPa [132]. The synthesis and formation of lithium nitride can take place in various ways [133–135], the simplest arguably being the reaction of solid lithium with nitrogen gas at elevated temperatures. This reaction can already take place under ambient conditions and is (together with various other side reactions) a reason why the manufacturing of lithium must take place under inert conditions. The interaction of lithium with molecular nitrogen is therefore of utmost importance for new generations of battery systems, such as all-solid-state, Li-sulfur [69–72] or Li-air [73–77] batteries, as they all employ a metallic lithium anode. In these types of batteries, metallic lithium has the potential to provide particularly high energy densities, as it has a low specific weight of 0.53 $\mathrm{g\ cm}^{-3}$ and with -3.04 V *vs.* SHE the highest standard electrode potential in the periodic table [13, 24, 25].

The spontaneous reaction of molecular nitrogen impurities during the production and operation of the battery can for example have an involuntary effect on the properties at the interface [49, 50]. In a battery lithium's pronounced electropositive nature causes the irreversible decomposition of any organic electrolyte and the formation of a solid-electrolyte interphase (SEI) on the metallic lithium anode [25, 30–38]. Although the formation of a stable SEI is thus associated with a loss of active material, it also prevents a progression of the irreversible reaction between lithium and the electrolyte. To ensure proper operability, the SEI must be both ion conductive and thermodynamically stable against lithium metal. Li_3N can therefore play several roles at the interface. Despite the limited time and length scales of quantum mechanical methods, which usually cannot cover the complexity of the description of the whole corrosion process, the identification of fundamental mechanisms at the atomic level may contribute to improving the chemical stability of metallic lithium anodes in a systematic way. In this work, we therefore present periodic density functional theory (DFT) calculations on absorption, diffusion and dissociation processes of monoatomic and molecular nitrogen on low index lithium surfaces, to obtain an understanding of the interaction between nitrogen and metallic lithium. As observed for other molecules in our previous studies [68, 136], nitrogen absorption on lithium was accompanied by the

emergence of recurring cluster-like Li/N-structures. To gain further insights into the initial stages of nitrogen corrosion, the binding energies were determined as a function of nitrogen coverage to assess the trends of the observed cluster formation.

4.3 Results and discussion

4.3.1 Nitrogen adsorption/absorption

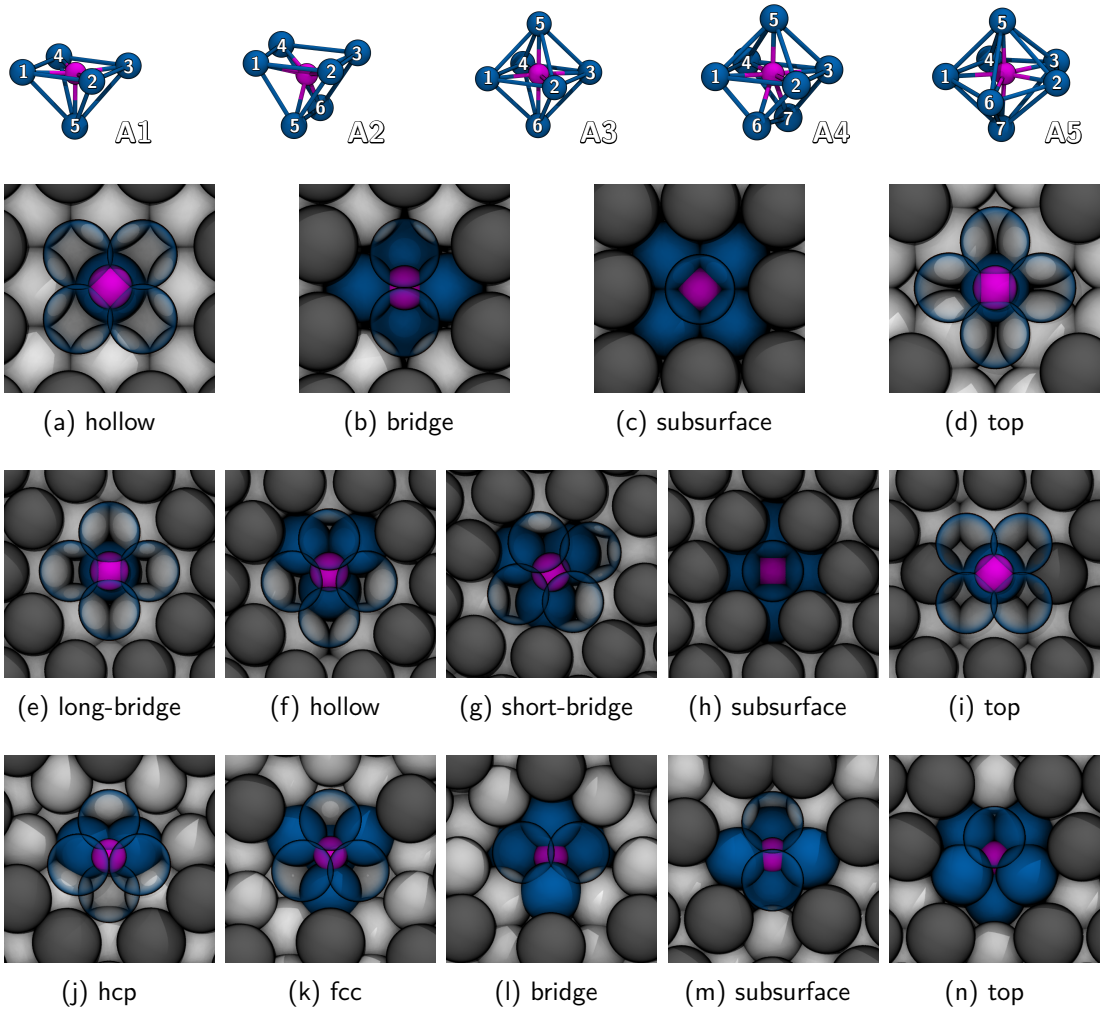

(a) hollow (b) bridge (c) subsurface (d) top

(e) long-bridge (f) hollow (g) short-bridge (h) subsurface (i) top

(j) hcp (k) fcc (l) bridge (m) subsurface (n) top

Figure 4.1. Surface structures of absorbed nitrogen on different adsorption sites on the low-index surfaces Li(100) in **(a)**−**(d)**, Li(110) in **(e)**−**(i)** and Li(111) in **(j)**−**(n)**. Lithium atoms of different layers are portrayed in different shades of grey. Nitrogen is shown in purple and the coordinating lithium atoms in blue. The graphic above is an exemplary depiction of the different cluster-like coordinations, which were formed on the absorption of hydrogen on the different lithium surfaces.

Table 4.1 Binding energies per atom $E_{\mathrm{bind,N}}$ on Li(100), Li(110) and Li(111). The binding energies are reported in eV and are referred to molecular N_2 in the gas phase. The charge of nitrogen on its absorption was analyzed using the DDEC6 charge methodology [96, 97] and is reported in e/atom.

(*hkl*)	Adsorption site	$E_{\mathrm{bind,N}}$	type	$q_{\mathrm{DDEC6,N}}$
Li(100)	*hollow*	-1.36	**A1**	-1.85
	bridge	-1.67	**A3**	-1.83
	subsurface	-1.53	**A3**	-1.81
	top	-0.43	**A1**	-1.88
Li(110)	*hollow*	-1.78	**A4/5**	-1.78
	long-bridge	-1.45	**A1**	-1.76
	short-bridge	-1.61	**A4**	-1.79
	subsurface	-1.44	**A3**	-1.76
	top	-1.16	**A2**	-1.76
Li(111)	*hcp*	-1.58	**A3**	-1.78
	fcc	-1.67	**A4**	-1.82
	bridge	-1.70	**A4**	-1.78
	subsurface	-2.08	**A3**	-1.87
	top	-1.24	**A4/5**	-1.79

To classify general aspects of the interaction between nitrogen and metallic lithium, we first investigated the monoatomic adsorption on the low-index surfaces Li(100), Li(110) and Li(111). To evaluate the storage of nitrogen, N atoms have been placed on highly symmetrical adsorption sites (Fig. 4.1a - 4.1n) above and below the surface. Depending on geometry and position at the surface, different cluster-like coordination structures (see Fig. 4.1) were formed through the interaction of nitrogen with the surrounding lithium environment. Their assignment to the corresponding adsorption sites can be found in Table 4.1.

In our earlier studies, we have already noticed a similar buildup of cluster-like structures on the absorption of hydrogen [136] and oxygen [68] on metallic lithium. In the case of hydrogen and oxygen, the lowest lithium coordination found was at four lithium atoms within a tetrahedral structure and the highest at six lithium atoms, which adopts an octahedral structure analogous to the **A3** cluster in Fig. 4.1. Although the energy difference was marginally low in both cases, the absorption of either hydrogen or oxygen on the surface was thermodynamically preferred to the absorption below the surface (*i.e.* subsurface). In comparison, nitrogen strived to form higher coordinated surface

clusters and tended to be embedded below the surface, where it was located in a more metal-rich environment. This can be seen from the binding energies in Table 4.1, as all absorption complexes below the surface show a higher stability. In this study, the lowest coordination we observed for nitrogen corresponded to the **A1** structure in which nitrogen was surrounded by five lithium atoms in a square pyramidal arrangement. On Li(100), the square pyramidal absorption structure was formed at both the *hollow* and *top* position. The Li(100)-N_{hollow} and Li(100)-N_{top} absorption complexes represented the only structures where nitrogen is adsorbed on the Li(100) surface. Analogous to the results from our previous studies on hydrogen and oxygen, four lithium atoms were torn from the surface to build the surface cluster on the *top* position. With a binding energy of -0.43 eV, Li(100)-N_{top} was the least stable complex on Li(100) and, despite the surface cluster's equivalent geometry, by 0.93 eV less stable than Li(100)-N_{hollow}. Li(100)-N_{subsurf} and Li(100)-N_{bridge} represented the absorption complexes below the surface on Li(100). While nitrogen was by design under the surface in the *subsurface* position, it penetrated through the first layer of lithium atoms into the surface on the absorption in the *bridge* position. In both complexes, nitrogen was trapped within an octahedral arrangement. In the case of Li(100), the Li(100)-N_{bridge} complex was with a binding energy of -1.67 eV the thermodynamically most favourable, followed by the only 0.14 eV less stable Li(100)-N_{subsurf} structure.

The adsorption on Li(110) led to the buildup of higher coordinated clusters. The cluster with the lowest coordination again had a square pyramidal **A1** geometry and was obtained for the absorption into the *long-bridge* with a binding energy of -1.45 eV. In comparison, Li(110)-N_{subsurf}, where nitrogen was located in an octahedral lithium environment, was with -1.44 eV almost degenerate. The least stable adsorption structure on Li(110) was obtained by absorption through the *top* position. Here, the attraction of the surrounding lithium atoms resulted in a trigonal prismatic-like **A2** cluster with a binding energy of -1.16 eV. Together with the Li(110)-$N_{\mathrm{longbridge}}$ complex, Li(110)-N_{top} was the only Li(110) structure, where nitrogen was found at the surface. In Li(110)-N_{hollow} and Li(110)-$N_{\mathrm{short-bridge}}$ nitrogen was found within a capped trigonal prismatic **A4** arrangement, which was with seven surrounding lithium atoms the highest coordination found on all investigated lithium surfaces. The *hollow* and *shortbridge* were with -1.78 and -1.61 eV respectively the most favoured absorption sites.

The trend of nitrogen absorbing under the surface continued for Li(111), as nitrogen preferably (from a thermodynamic point of view) absorbed into the *subsurface* position

with an energy of -2.08 eV, where it adapted octahedral coordination. Although Li(111)'s morphology predefined a trigonal pyramidal geometry for the surface clusters on the *hcp* and *fcc* sites (as was the case for hydrogen and oxygen), the nitrogen absorption caused the formation of higher coordinated octahedral and capped trigonal prismatic surface complexes. From a thermodynamic point of view, the *fcc* site was by 0.09 eV more stable than the *hcp* site. A capped trigonal prismatic coordination was also found in the Li(111)-N_{bridge} complex, which was with only 0.03 eV almost degenerate to Li(111)-N_{fcc}. The least stable surface complex on Li(111) was again found after the absorption on the top position. In the Li(111)-N_{top} structure, seven lithium atoms enclosed the nitrogen atom in a configuration, that can be described as an intermediate between the **A4** and **A5** geometry (*i.e.* **A4/5**). A DDEC6 charge analysis of the absorption complexes has shown, that in each case the absorption led to a large charge transfer from the surface to the nitrogen atom. As can be seen in Table 4.1, the order of magnitude for the transferred charge was somewhat below that of nitrogen in bulk-Li_3N $\left(q_{\mathrm{DDEC6,N}}^{\mathrm{Li_3N}} = -2.18\ e/\mathrm{atom}\right)$.

4.3.2 Diffusion of monoatomic nitrogen on Li(100) and in Li(*bcc*) bulk

A comparison of the binding energies for the different absorption sites has shown, that nitrogen (from a thermodynamic point of view) prefers to absorb into the Li(100) than on top of it. Furthermore, the absorption into the *bridge* position has shown that storage under the surface must be connected with very low diffusion barriers since the nitrogen atom has already penetrated the first layer of lithium atoms during simple energy minimization. Therefore, to evaluate the mobility of a nitrogen atom on metallic lithium, the energy profile for the diffusion between the *hollow*, *bridge* and *subsurface* positions was determined. The energy profile for monoatomic diffusion on Li(100) is shown with the corresponding surface structures in Fig. 4.2a, wherein the energies of the absorption complexes are related to those of Li(100)-N_{hollow}. Analogous to the findings for oxygen diffusion on the metallic Li(100) [68], the diffusion of nitrogen also took place within a coordination shell of lithium atoms. Due to the formation of further coordination complexes on the surface, several local minima were passed through during simple nitrogen diffusion between the highly

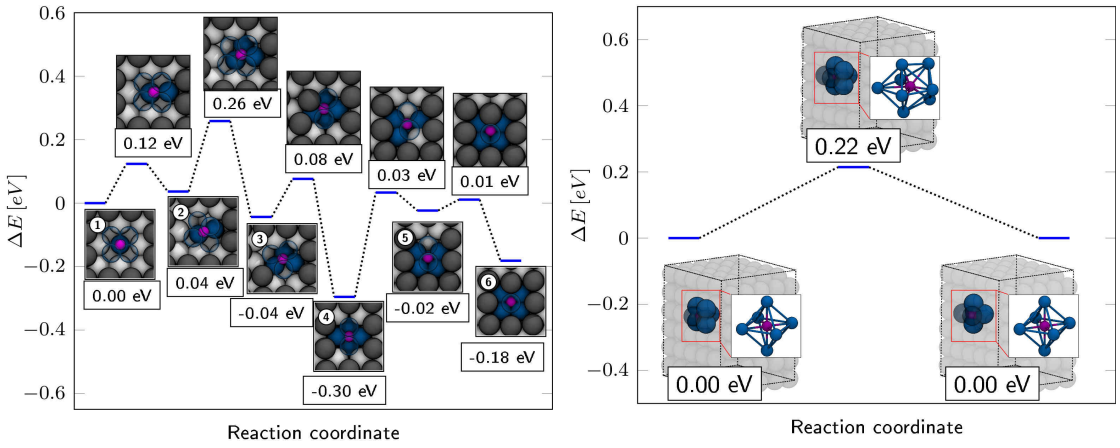

(a) Diffusion profile for a nitrogen atom on Li(100) (b) Diffusion profile for a nitrogen atom through Li(bcc)-bulk

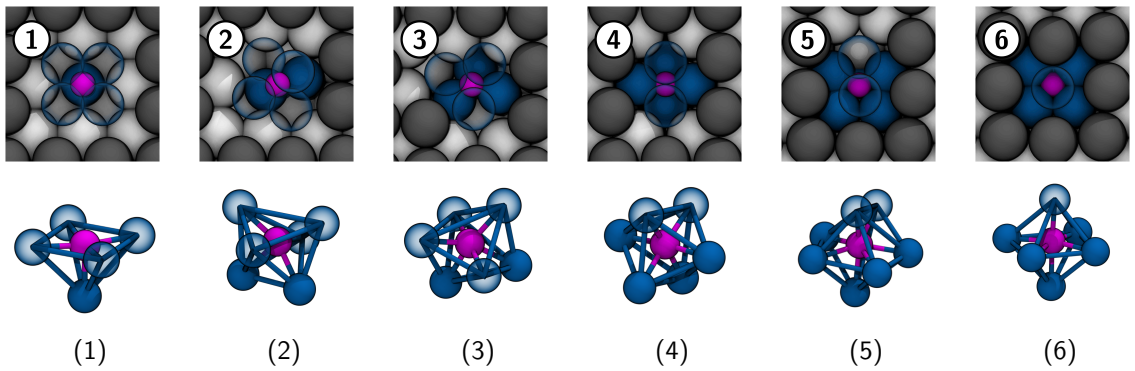

Figure 4.2. Energy profiles for the surface and bulk diffusion of nitrogen. The energy profile in **(a)** shows the diffusion on a Li(100) surface from a *hollow* site to a neighbouring *bridge* site via two intermediate local minima, followed by diffusion to a neighbouring *subsurface* position, by passing another local minimum. The framed values indicate the relative energy in eV related to the initial *hollow* position. The surface sections and corresponding clusters shown in **(1)** - **(6)** refer to the structures illustrated in the diffusion profile for the monoatomic surface diffusion. For illustration, the coordinating lithium atoms at the surface are depicted transparently in the clusters as well. The diffusion profile for a nitrogen atom through the Li(bcc)-bulk structure is shown in **(b)**. The framed values indicate the relative energy in eV related to the most stable structure. The diffusion takes place from a position in the bulk material in which nitrogen is octahedrally coordinated to an equivalent octahedral coordination. Shown are the structures of the octahedrally coordinated initial and final structure, as well as the transition state.

Table 4.2 ΔE_{back} and ΔE_{for} diffusion barriers for the respective backward and forward diffusion processes of monoatomic nitrogen in eV.

Process			ΔE_{for}	ΔE_{back}
①-N_{hollow}	$\longrightarrow$	②-N	0.12	0.08
②-N	$\longrightarrow$	③-N	0.22	0.30
③-N	$\longrightarrow$	④-N_{bridge}	0.12	0.38
④-N_{bridge}	$\longrightarrow$	⑤-N	0.33	0.05
⑤-N	$\longrightarrow$	⑥-N_{subsurf}	0.03	0.19
Li(bcc)-$N_{\mathrm{bulk,1}}$	$\longrightarrow$	Li(bcc)-$N_{\mathrm{bulk,2}}$	0.22	0.22

symmetric absorption sites. The assignment of the local minima, as well as the representation of the corresponding cluster geometries, is shown in Fig. 4.2 (1) - (6). Interestingly enough, the local minima showed similar coordination geometries as on the highly symmetric absorption sites, as nitrogen had an octahedral coordination environment of type **A3** in ②-N, while it was encapsulated within a **A4** capped trigonal prismatic cluster in ⑤-N. Within ③-N, the nitrogen atom was coordinated by six lithium atoms, resulting in a distorted octahedral structure. The diffusion of ①-N_{hollow} to ④-N_{bridge} took place via the two local minima ②-N and ③-N. The barrier for the diffusion of ①-N_{hollow} to ②-N was 0.12 eV and that of ②-N to ③-N was 0.22 eV, while the corresponding barriers for the diffusion back were 0.08 eV and 0.30 eV respectively. Thus, the barrier for the reverse process is lower by only 0.04 eV in the case of ①-N_{hollow} to ②-N, while it is higher by 0.08 eV for ②-N to ③-N. Starting from the ③-N structure, the nitrogen atom could diffuse into the ④-N_{bridge} position over a barrier of 0.12 eV. In comparison, the back diffusion barrier of 0.38 eV was more than three times as high, which makes back diffusion to the surface unlikely when kinetic aspects are also taken into account. Accordingly, nitrogen must be stored on the lithium surface not only from a thermodynamic point of view but also under consideration of the kinetic aspects. The diffusion of ④-N_{bridge} into ⑥-N_{subsurf} took place via the local minimum ⑤-N, whereby the diffusion barrier for the nitrogen atom from ④-N_{bridge} to ⑤-N was 0.33 eV and from ⑤-N to ⑥-N_{subsurf} 0.03 eV. Starting from ⑥-N_{subsurf} the corresponding back barriers were significantly lower at 0.05 eV and 0.19 eV. For nitrogen, the Li(100)-N_{bridge} structure is therefore not only the most thermodynamically stable structure on Li(100) but also easily accessible via low barriers and kinetically stabilized via comparably high back barriers. Nevertheless, all the barriers are of a magnitude that allows high nitrogen mobility on the metallic lithium

surface. Since storage into the metallic lithium surface is preferred, we also investigated the energy profile for the nitrogen diffusion in the *bcc*-bulk material in which nitrogen was stored in an octahedral cavity, as it is shown in Fig. 4.2b. Here, with 0.22 eV nitrogen again showed an extremely low barrier for bulk diffusion between two cavities. In contrast to hydrogen and oxygen, which had transition states in the bulk material, that were coordinated by four lithium atoms with a tetrahedral geometry, for bulk lithium, nitrogen is surrounded by eight lithium atoms in the transition state along the bulk-diffusion.

4.3.3 Diffusion and dissociation processes of molecular N_2 on Li(100)

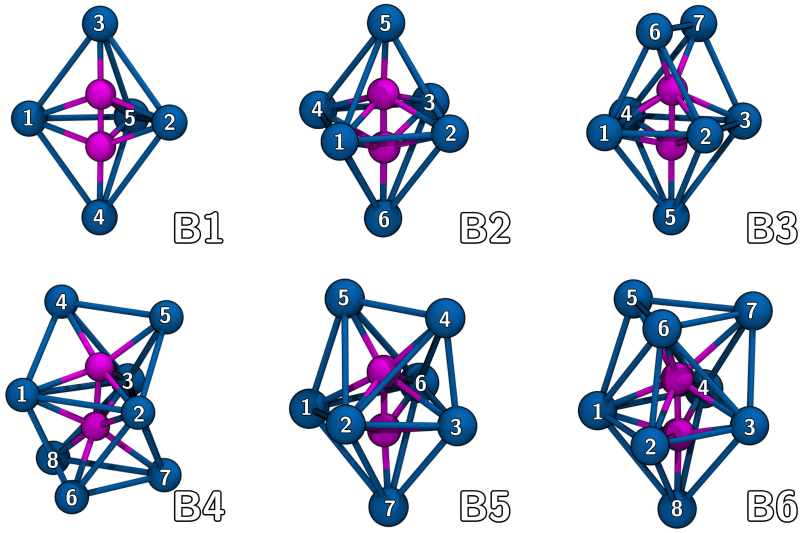

Figure 4.3. Summary of the different cluster-like coordinations, which were formed on the absorption of N_2 on metallic lithium surfaces. The coordinating lithium atoms are shown in blue and nitrogen in purple

In bulk-Li_3N a nitrogen atom is surrounded by only eight different lithium atoms/ions. An interaction between metallic lithium and the molecular nitrogen from the atmosphere requires an empty volume or vacancy to host molecular N_2. Here, our investigations of N_2 absorption on metallic lithium surfaces have shown, that molecular nitrogen can indeed also form cluster-like coordination compounds in which the undissociated N_2 molecule is embedded in a lithium coordination environment. In the following the

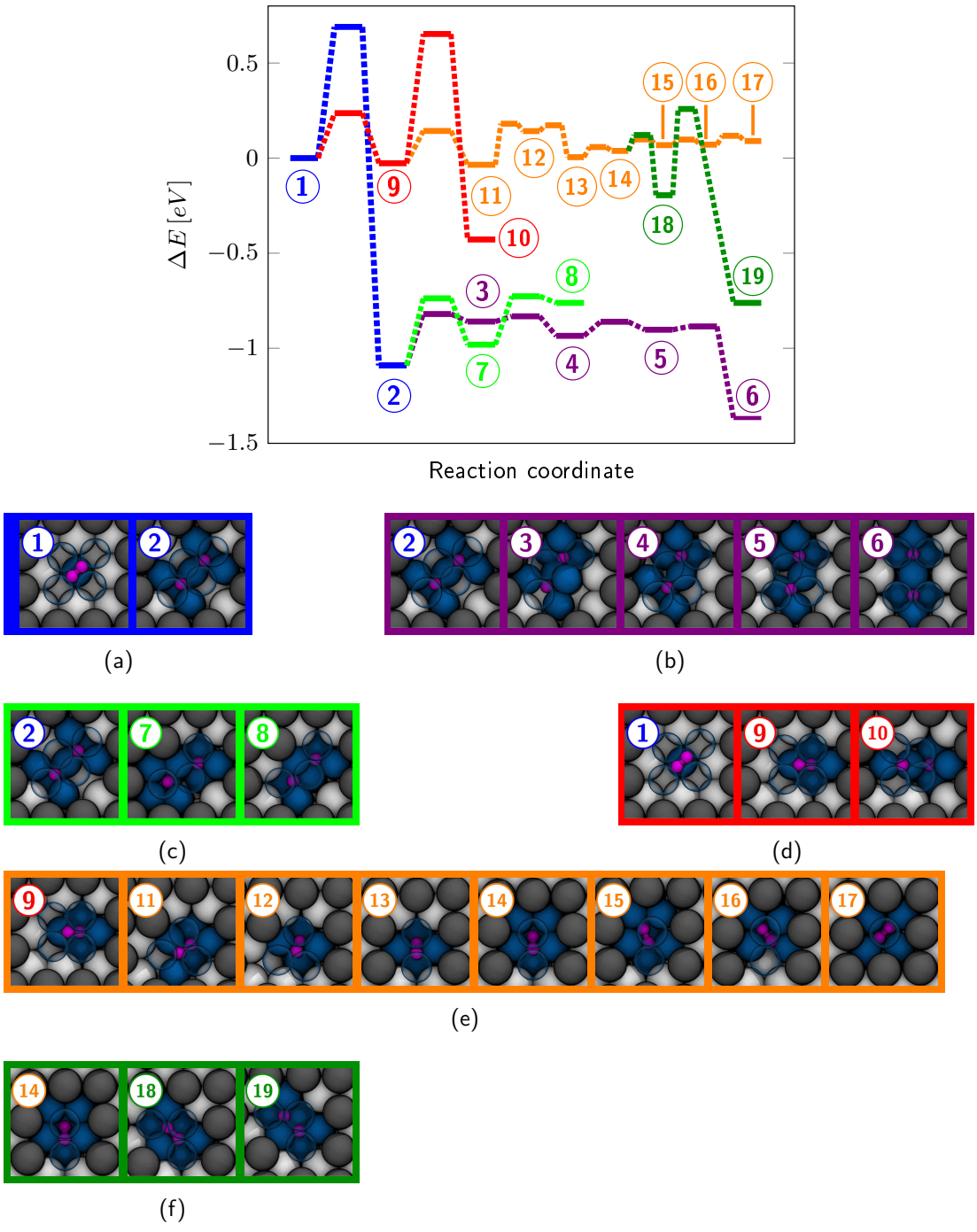

Figure 4.4. Energy profiles for the diffusion and dissociation of a single N_2 molecule on Li(100) obtained by means of NEB calculations. The different paths in **(a)** - **(f)** were assigned to the profile via a colour code. The numbering of the structures corresponds to that in the energy profile. The relative energies in the energy profile were all related to the initial, undissociated structure.

Table 4.3 Diffusion and dissociation barriers ΔE_{back} and ΔE_{for} of N_2 on Li(100) for the respective backward and forward processes in eV. Every second structure in every row was assigned its relative energy ΔE_{1-x} in eV (related to the initial structure) and the type of nitrogen cluster (see Fig. 4.1 or Fig. 4.3).

	Process			ΔE_{for}	ΔE_{back}	ΔE_{1-x}	type
4.4a	①-N_2	$\longrightarrow$	②-2N	0.69	1.78	-1.07	**A4/5**, **A4/5**
4.4b	②-2N	$\longrightarrow$	③-2N	0.27	0.04	-0.84	**A4/5**, **A5**
	③-2N	$\longrightarrow$	④-2N	0.03	0.10	-0.91	**A3**, **A4**
	④-2N	$\longrightarrow$	⑤-2N	0.07	0.04	-0.88	**A3**, **A3**
	⑤-2N	$\longrightarrow$	⑥-2N	0.02	0.48	-1.35	**A3**, **A3**
4.4c	①-2N	$\longrightarrow$	⑦-2N	0.35	0.24	-0.96	**A3**, **A5**
	⑦-2N	$\longrightarrow$	⑧-2N	0.25	0.04	-0.74	**A3**, **A3**
4.4d	①-N_2	$\longrightarrow$	⑨-N_2	0.24	0.26	-0.01	**B4**
	⑨-N_2	$\longrightarrow$	⑩-2N	0.68	1.08	-0.40	**A2**, **A3**
4.4e	⑨-N_2	$\longrightarrow$	⑪-N_2	0.17	0.18	-0.02	**B4/5**
	⑪-N_2	$\longrightarrow$	⑫-N_2	0.22	0.04	0.16	**B5**
	⑫-N_2	$\longrightarrow$	⑬-N_2	0.03	0.17	0.02	**B2**
	⑬-N_2	$\longrightarrow$	⑭-N_2	0.05	0.03	0.05	**B6**
	⑭-N_2	$\longrightarrow$	⑮-N_2	0.06	0.03	0.09	**B4/5**
	⑮-N_2	$\longrightarrow$	⑯-N_2	0.03	0.03	0.09	**B5**
	⑯-N_2	$\longrightarrow$	⑰-N_2	0.05	0.03	0.11	**B2**
4.4f	⑮-N_2	$\longrightarrow$	⑱-N_2	0.08	0.32	-0.18	**B4/5**
	⑱-N_2	$\longrightarrow$	⑲-2N	0.45	1.24	-0.74	**A3**, **A3**

absorption complexes have been used for studies on the energy profile for diffusion and dissociation of molecular N_2. Analogous to the energy profile for monoatomic nitrogen diffusion, the energy profiles for the diffusion of molecular N_2 also passed through different local minima, which were the result of the formation of different cluster geometries Fig. 4.4 and Fig. 4.3. A summary of all investigated energy profiles and the illustrations of the respective absorption complexes can be found in Fig. 4.4. The designation of the structures and an assignment to the corresponding energies and cluster structures can be found in Tab. 4.3. The starting point is the ①-N_2 absorption structure on Li(100), in which a N_2 molecule is absorbed in a *hollow* position with a binding energy of 1.03 eV/atom. In this structure, the N−N binding distance extends

its original 1.12 Å to 1.27 Å, whereby the N_2 molecule is in a **B1** configuration. For the specification of relative energies ΔE in the energy profile in Fig. 4.4 and in Table 4.3, the energies of the absorption complexes are related to the ①-N_2 structure. With a barrier of 0.69 eV nitrogen can dissociate directly from the ①-N_2 into the ②-2N configuration in which the two separated nitrogen atoms are present in a **A4/5** (see Fig. 4.1) configuration, as it is shown in Fig. 4.4a. From the ②-2N, the two separated nitrogen atoms can either diffuse into the ⑥-2N or ⑧-2N structure via green and magenta paths shown in Fig. 4.4b or in Fig. 4.4c, respectively. In both structures, the nitrogen atoms are located in two *bridge* positions, so that both have an octahedral lithium coordination shell. The ⑥-2N is, however, by 0.61 eV more stable and the nitrogen atoms are sharing a single lithium atom instead of three, as is the case in ⑧-2N. Since the formation of the coordination structures was induced by the attraction of lithium atoms through nitrogen, it can be assumed that the large energetic difference between those structures was due to a larger stress on more lithium atoms, caused by the attraction through two nitrogen atoms. Consequently a diffusion from ②-2N into ⑧-2N cannot be expected from a thermodynamic point of view, as it would lead to a decrease in stability. For the diffusion to ⑥-2N, the highest barrier was 0.27 eV, while the highest barrier for the reverse process was 0.48 eV. The remaining barriers for the diffusion between the local minima were comparatively low with a maximum of 0.10 eV.

Another dissociation process, that originated from the initial ①-N_2, is shown in Fig. 4.4d. In this path, the N_2 molecule first underwent a rotation, until one nitrogen atom was in the *hollow* and the other in a *bridge* position. The transition from ①-N_2 to ⑨-N_2 took place with a barrier of 0.24 eV and led to an energetically nearly degenerated structure with a difference of only 0.01 eV. In the ⑨-N_2 structure the nitrogen had a bond length of 1.45 Å and was embedded in a **B4**-type cluster configuration. Out of this structure, nitrogen could completely dissociate with a barrier of 0.68 eV into the *hollow* and *bridge* position in ⑩-2N. The dissociation resulted in an overall stability gain of 0.40 eV compared to the initial configuration. Coming from ⑨-N_2, N_2 could also diffuse beneath the surface instead of dissociating. The diffusion of the N_2 molecule from ⑨-N_2 to ⑪-N_2 showed with 0.17 eV a significantly lower barrier compared to dissociation. Via the orange path shown in Fig. 4.4e, N_2 could therefore diffuse into the *subsurface* without dissociating. The highest barrier on this path was 0.22 eV and found for the diffusion from ⑪-N_2 to ⑫-N_2. For the reverse process, the highest barrier

was 0.18 eV and corresponded to the diffusion of ⑪-N_2 to ⑨-N_2. The remaining barriers of this path were comparatively low with values between 0.03 and 0.06 eV and caused a very flat energy profile for diffusion under the surface. From a thermodynamic point of view, most of the N_2 structures under the surface are slightly less stable than in the initial ①-N_2 structure. Here the ①-N_2 structure shows with 0.16 eV the highest difference towards the initial structure, while the remaining absorption complexes on this path had small differences between -0.02 and 0.11 eV. The ⑭-N_2 complex, in which N_2 was trapped in a **B6** configuration, lied 0.09 eV above the initial structure. From here, dissociation of the N_2 molecule into ⑧-N_2 could occur via the dark green path shown in Fig. 4.4f. In contrast to the dissociation in Fig. 4.4b, the dissociation in Fig. 4.4f takes place under the surface. Via a low barrier of 0.08 eV N_2 could diffuse from the ⑭-N_2 into ⑮-N_2 structure. In ⑮-N_2, N_2 is present in the **B4/5** configuration and is by 0.18 eV more stable than in the initial structure. From this structure, N_2 can dissociate into the ⑧-N_2 structure via a barrier of 0.45 eV. For the processes found and studied, the barrier for N_2 dissociation from a structure below the surface was thus about 0.24 eV lower than on the surface. These results agree with the investigations of Ludwig *et al.* who observed the dissociation of nitrogen on Li(110) below the surface using a metadynamics investigation [137].

4.3.4 Coverage-dependent absorption on Li(100)

To assess the binding energy on Li(100) as a function of nitrogen coverage, symmetrical arrangements on the *hollow*, *bridge* and *subsurface* sites were created and geometry optimized for coverages between 0.03 and 1.0 monolayers (ML). As with the absorption of a single nitrogen atom, an ordered arrangement of the cluster-like structures was formed even with higher coverages up to 0.50 ML. As one can see in Table 4.4, the nitrogen coverages below 0.50 ML did not influence the binding energy since there were enough lithium atoms in between to form separate cluster-like structures. Consequently, the *bridge* position remained the most stable absorption site even at higher coverages. The influence on geometry and binding energy became evident at higher coverages since the proportion of lithium in relation to absorbed nitrogen became too small to form separate clusters at coverages $\geq$ 0.50 ML. In our previous study on lithium oxidation, we were able to show, that the driving force for cluster formation had led to a complete rearrangement of the ordered surface structure

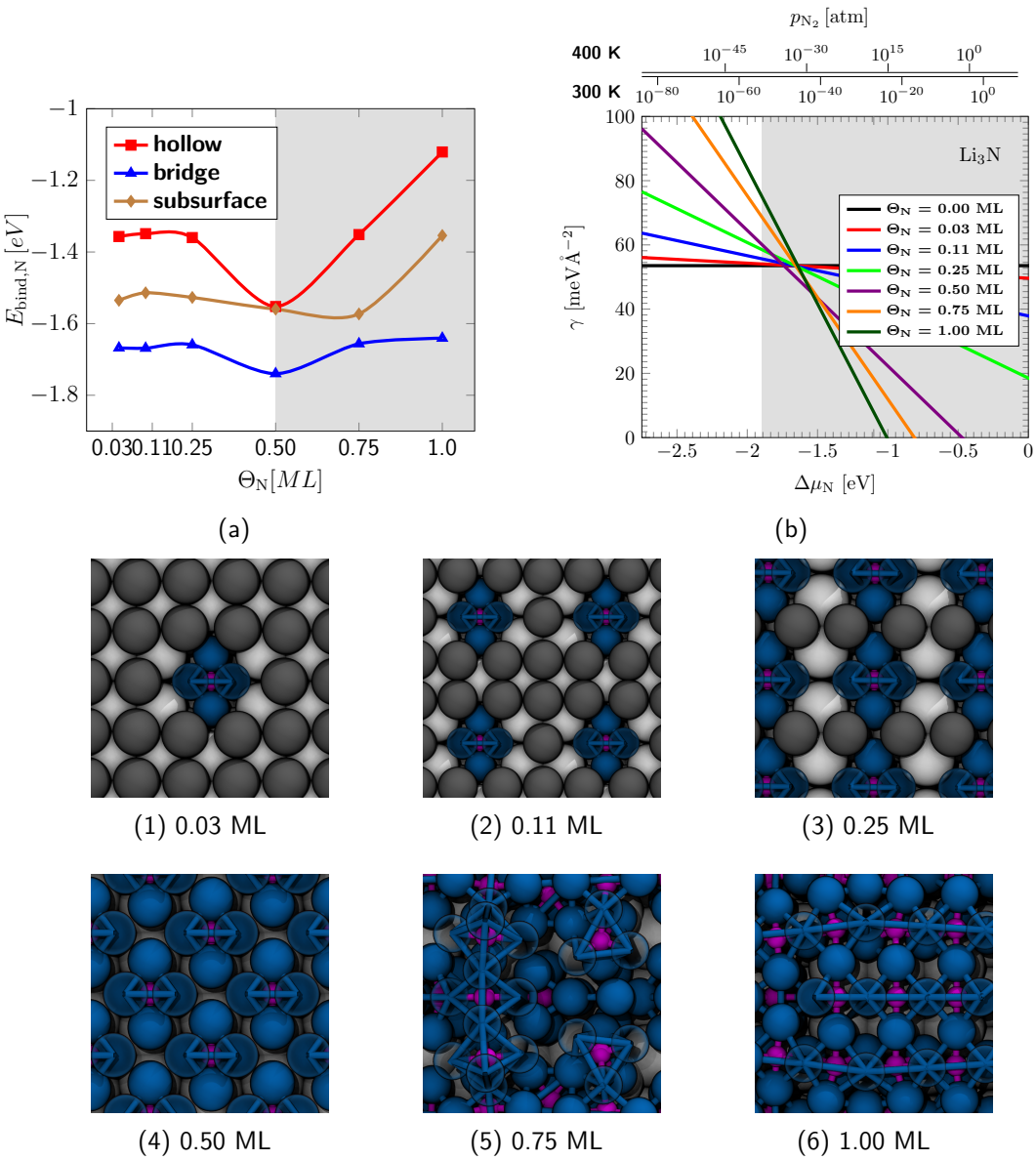

Figure 4.5. Binding energies per nitrogen atom $E_{\mathrm{bind,N}}$ in eV as a function of the nirtogen coverage Θ_{N} shown in **(a)**. The grey area represents the range, where a strong reorganisation of the Li(100) surface structure to an amorphous arrangement was observed. In **(b)** a phase diagram for the surface oxidation of Li(100) as a function of the nitrogen chemical potential is shown. For fixed temperatures of 300 K and 400 K, the chemical potential has been translated to the corresponding pressures. The grey area resembles the nitrogen-rich environment, where the $\mathrm{Li_3N}$ results as the most stable phase. In **(1)** - **(6)** sections of the most stable Li(100) surfaces at different nitrogen coverages Θ_{N} are shown. Here, the coordinating lithium atoms are coloured blue. To illustrate the coordination geometries, the bonds between the coordinating lithium atoms are drawn.

Table 4.4 Binding energies per atom $E_{\mathrm{bind,N}}$ on the Li(100) surface as a function of the nitrogen coverage Θ_{N} in monolayers (ML) for different arrangements of the high-symmetry adsorption sites. The energies are referenced to molecular N_2 in gas phase and are reported in eV.

Θ_{N} (ML)	$E_{\mathrm{bind,N}}$ (eV)		
	hollow	*bridge*	*subsurface*
0.03	-1.36	-1.67	-1.53
0.11	-1.35	-1.67	-1.51
0.25	-1.36	-1.66	-1.53
0.50	-1.55	-1.73	-1.56
0.75	-1.36	-1.66	-1.57
1.00	-1.12	-1.64	-1.35

at higher coverages. As can be seen in Fig. 4.5 (1) - (6), this behaviour was also observed for nitrogen absorption, where amorphous configurations were formed on the surface. With the most stable *bridge* arrangements, an amorphous arrangement was formed first with coverages $\Theta_{\mathrm{N}} > 0.50$ ML, while these formed already at $\Theta_{\mathrm{N}} = 0.50$ ML for the *hollow* and *subsurface* structures. The reason for this is, that it was possible to build an arrangement of *bridge* sites at 0.50 ML, in which the nitrogen coordinating lithium atoms were separated from each other. In contrast, an arrangement of *hollow* and *subsurface* sites, which would have allowed the formation of separated clusters, was not possible at 0.50 ML. The rearrangements of the *bridge* structures resulted in the additional formation of complexes **A4** and **A5** in addition to the octahedral **A3**. For the *hollow* and *subsurface* structures, molecular clusters, as they are shown in Fig. 4.3, were also observed with increasing coverage. This was the case at $\Theta_{\mathrm{N}} \geq 0.75$ ML for the *hollow* structures, and at $\Theta_{\mathrm{N}} = 1.00$ ML for the *subsurface* structures. The smallest influence of the coverage on the binding energies was found for *bridge* structures since the nitrogen atoms were already in octahedral coordinations at lower coverages, which was also the predominant coordination in the amorphous structures (despite the additional **A4** and **A5** complexes). For the same reason, the binding energies of the *subsurface* structures hardly changed for coverages $\Theta_{\mathrm{N}} \leq 0.75$ ML. Only when the more unstable molecular cluster compounds formed at a coverage of 1.00 ML, did the binding energy decrease to -1.35 eV/atom. In the case of the *hollow* structures, the formation of more highly coordinated octahedral structures through amorphization initially led to a gain in stability with a binding energy of -1.55 eV at

0.50 ML. However, with the formation of molecular N_2-structures at 0.75 ML and 1.00 ML, the stability decreased to binding energies of -1.36 eV and -1.12 eV, respectively. To classify how the stability depends on the surrounding temperature and pressure, the free surface energy of the considered phases was calculated as a function of the chemical potential of nitrogen, based on the *ab-initio* thermodynamic approach [102, 138–140]. As can be seen from the phase diagram in Fig. 4.5b, the surface structures of nitrogen on Li(100) are to be classified as metastable, since the nitrogen is preferably present in bulk-Li_3N (despite its stability against the pure lithium surface).

4.4 Conclusions

In this work, we have investigated the initial mechanisms and principles of the interaction between metallic lithium and atomic and molecular nitrogen through periodic density functional theory. Here, the calculations for monoatomic nitrogen absorption on the low-indexed Li(100), Li(110) and Li(111) surfaces have already shown that the formation proceeds analogously to the initial lithium oxidation under the formation of coordinated cluster-like structures. The adsorption/absorption took place, as one would expect due to lithium's low standard electrode potential, under a high negative charge transfer from the lithium surface to the adsorbate/absorbate. Because the negative charge had a comparable order of magnitude as the nitride ion in the bulk-$\mathrm{Li_3N}$, nitrogen formed cluster compounds with a higher number of lithium atoms in comparison to oxygen and hydrogen. The binding energies at the highly symmetric adsorption sites on and below the surface have shown that, from a thermodynamic point of view, the absorption of nitrogen below the surface is similarly stable or even more stable than at the surface. The stability of nitrogen under the surface can be explained by the tendency of nitrogen to form higher coordinated compounds since a higher number of lithium binding partners is available under the surface. Analogous to hydrogen and oxygen, the formation of coordinated nitrogen clusters also influences nitrogen's diffusion behaviour, as nitrogen moves within a coordination shell of lithium atoms. For the diffusion on metallic Li(100), nitrogen's aspiration to build up more bonds to lithium than in the case of hydrogen and oxygen becomes also evident by passing through different local minima, in which it takes on similar cluster structures as on the highly symmetric absorption sites. Of the investigated structures in this study, nitrogen adopts eight lithium atoms the highest coordination of lithium atoms in the transition state for bulk diffusion.

The analysis of the N_2 absorption on metallic lithium surfaces has shown, that nitrogen also forms cluster-like compounds in its molecular form, in which the N-N bond remains. The calculation of energy profiles for different diffusion and dissociation processes on the surface has shown, that the N_2 cleavage on the surface is associated with a comparatively high barrier of 0.69 eV. For the diffusion of the N_2 molecule below the surface, however, comparatively low barriers of a maximum of 0.22 eV had to be overcome. Starting from a position below the surface, the N_2 molecule showed a significantly lower barrier for dissociation. The findings for the N_2 dissociation on Li(100) are in good agreement with the simulations by Ludwig *et. al.* who observed the same behaviour for N_2 on Li(110) [137]. Assessing how the coverage depends on absorption, higher nitrogen coverages of up to 1 ML were calculated at the locations *hollow*, *bridge* and *subsurface*. As soon as there were not enough lithium atoms for the formation of cluster structures on the surface, the tendency to form the preferred cluster-like configuration led to larger transformations and disordered arrangements of cluster structures. The strong diffraction for rearrangement with a low supply of lithium on the surface could already be observed for the oxidation of metallic lithium. Due to the metastability of N_2 on the surface, nitrogen (in contrast to oxygen) was able to escape in clusters with an N-N bond, in which less lithium was required per nitrogen for coordination at higher coverages. The formation of the N-N clusters, however, led to a sharp drop in stability. The thermodynamic evaluation of the surface stability via a corresponding surface phase diagram has shown, that at low pressures of N_2 bulk-Li_3N is the thermodynamically preferred phase, although the investigated absorption complexes can be considered as metastable under these conditions.

5

Atomistic studies on water-induced lithium corrosion

Matthias van den Borg [1, 2], Daniel Gaissmaier[1, 3, 4], Edwin Knobbe[2], Donato Fantauzzi [3, 4, 5] and Timo Jacob[1, 3, 4], *ChemSusChem* **2022**, *15*, e2021017.

Reproduced from Ref. [136] under the CC BY-NC-ND 4.0 licence [141] and with the authors' permission.

Style, numbering and citations have been adapted to ensure a consistent presentation throughout the work.

[1] Institute of Electrochemistry, Ulm University, Albert-Einstein-Allee 47, D-89081 Ulm, Germany
[2] BMW Group, 80809 Munich
[3] Helmholtz-Institute Ulm (HIU) for Electrochemical Energy Storage, Helmholtzstr. 11, 89081 Ulm, Germany
[4] Karlsruhe Institute of Technology (KIT), P.O. Box 3640, 76021 Karlsruhe, Germany

5.1 Abstract

It is well known that lithium reacts violently with water under the release of molecular hydrogen and the formation of lithium hydroxide. In this work, the initial mechanisms for the surface reactions of metallic lithium with water from the gas phase were investigated using periodic DFT calculations. For this purpose, we investigated adsorption/absorption structures, diffusion and dissociation processes of hydrogen, OH and H_2O on low index metallic lithium surfaces. Through thermodynamic and kinetic considerations, we have identified negatively charged centres on the surface as the origin of hydrogen formation. The strikingly low reaction barriers for the reaction at these centres implied a self-supporting effect of hydrogen evolution and the associated lithium degradation.

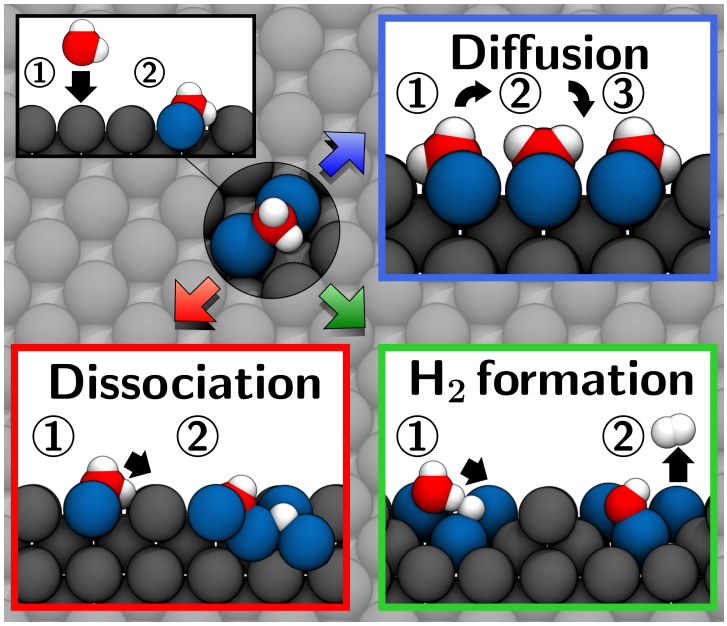

Figure 5.1. Schematic illustration of the investigated processes of H_2O on metallic lithium anodes.

5.2 Introduction

Having been used in a wide range of electronic applications since 1991 [142], lithium-ion batteries (LIBs) have successfully penetrated the automotive sector in the last decade, thus paving the way for the transition to electromobility on a large scale. To continue mass-market penetration in the automotive sector, it is mandatory to further advance the optimisation and development of new generations of batteries towards competitive alternatives to fossil fuels, by significantly increasing the batteries' energy densities and maintaining a high safety standard [143–145]. Since using Li-ions for energy storage is currently a very promising technology in terms of energy and power density, numerous approaches are aiming to improve the volumetric and gravimetric energy densities of anode and cathode materials. Thus, further developments of LIBs, *e.g.* through the use of high-capacity conversion materials, are all realised within the rocking-chair technology, which is based on the exchange of lithium ions between two intercalation/conversion materials [13, 24, 81, 146, 147]. While maintaining the necessary safety standards, the search for new candidates for energy storage in electromobility is not limited to the prevailing rocking-chair technology, but must also consider alternative battery concepts. As metallic lithium promises a particularly high energy density [13, 24, 25] (low specific weight of 0.53 $\mathrm{g\ cm^{-3}}$ and high standard electrode potential of -3.04 V *vs.* SHE), it is considered to be the "holy grail" among anode materials. Due to its outstanding features, the metallic lithium anode is therefore one of the key components of several innovative battery architectures at the moment [69–77]. Unfortunately, despite its excellent properties, metallic lithium is extremely difficult to handle, as its chemical nature causes several complications [13, 24, 78]. While problems of the lithium anode, such as plating and dendrite growth, are related to poorly understood, non-uniform deposition processes of metallic lithium, the extremely high reactivity of lithium already poses challenges both during production and cell operation. Inside a battery, the reactivity of lithium is expressed in particular by the decomposition of the electrolyte to form a solid electrolyte interphase (SEI) as soon as the lithium anode comes into contact with an organic electrolyte [25, 30–38] Lithium's reactivity, however, is already evident outside the battery, as lithium can undergo various reactions in contact with the atmosphere under the formation of stable salts. The instability of pure lithium against atmospheric molecules, such as oxygen [43–48], nitrogen [49, 50] and carbon dioxide [48] during processing is therefore already a factor, which makes inert conditions

imperative during production. In both cases, the degradation is associated with a loss of active material, leading to a lower cell performance. As lithium reacts violently with water, under the formation of hydrogen and lithium hydroxide [46], the degree of humidity in the environment is particularly important for lithium degradation. Due to an extreme vulnerability to even minor impurities of water at the ppm level, [148], exposure of the highly sensitive lithium surface to even tiny amounts of moisture already leads to reduced performance and lifetime during cell manufacturing. Within a battery, water can reach the lithium anode not only via moisture from the atmosphere (*e.g.* if there is a defect in the battery), but also via traces in the electrolyte and cathode, which often have a hygroscopic character [149]. The components of a battery can therefore already be the source of a considerable quantity of water within the cell. At the lithium anode, water impurities can decisively influence the anode's surface and interface properties by either reacting with the SEI, which (due to its composition of salts) often has a hygroscopic character, or directly through the reduction at the metal anode. Through the reaction of lithium with water and the resulting products, a variety of compounds (such as hydrides, oxides and hydroxides) can form on the anode's surface. Although the interaction between lithium and atmospheric impurities consequently has a crucial impact on the interface of the lithium metal anode, little is known about the exact processes of water-induced lithium corrosion on an atomic level. This is mainly due to the high reactivity of metallic lithium, as the investigation of adsorption processes and reactions with contaminants is experimentally difficult to access. To gain insights into the initial stages and mechanisms of water-driven lithium corrosion, we present in the current work periodic density functional theory (DFT) calculations on thermodynamic stabilities as well as diffusion and dissociation processes of hydrogen, hydroxide and water on metallic lithium surfaces. First, we investigated the interaction of monoatomic hydrogen with low-index lithium surfaces by considering structural changes and binding energies, as well as diffusion and dissociation processes of monoatomic and molecular hydrogen on Li(100). Afterwards, we investigated the fundamental diffusion and dissociation properties of OH and H_2O on Li(100) and further reaction mechanisms that can provide information on hydrogen evolution on metallic lithium.

5.3 Computational details

Periodic DFT calculations have been performed using the Vienna *ab initio* simulation package (VASP) [86–88]. The core electrons were described through projector augmented-wave (PAW) potentials as implemented in VASP, with valence states of 2*s* for lithium and hydrogen and 2*s*2*p* for oxygen. The plane wave energy cutoff was set to 400 eV. Exchange and correlation effects have been taken into account through the generalized gradient approximation (GGA) in the form suggested by Perdew, Burke, and Ernzerhof (PBE) [90]. The metallic lithium surfaces were calculated on (5x5) and (4x8) surface unit cells for Li(100) and Li(110) with eleven layers each, and a (4x6) surface unit cell with seventeen layers for Li(111). In all cases the Monkhorst-Pack [101] sampling with a ***k***-point mesh density of at least 0.15 $Å^{-1}$ was used. For all surface slabs, the lowest two layers have been fixed to the calculated lattice constant of *bcc*-Lithium present in the space group $\mathrm{Im\bar{3}m}$ (a=3.441 Å)[68, 89, 117]. The remaining surface layers and the respective adsorbates were allowed to fully optimize their geometries until the force-convergence criterion of 0.005 eV/Å was met. Each supercell employed a 15 Å vacuum region normal to the surfaces. Binding energies were referenced to $E^{\mathrm{gas+ZPE}}_{\mathrm{molecule}}$ of the respective gas phase molecule:

$$E^{\mathrm{gas+ZPE}}_{\mathrm{molecule}} = E^{\mathrm{gas}}_{\mathrm{molecule}} + E^{\mathrm{ZPE}}_{\mathrm{molecule}}. \tag{5.1}$$

Here, $E^{\mathrm{gas}}_{\mathrm{molecule}}$ is the total energy of the gas phase molecule and $E^{\mathrm{ZPE}}_{\mathrm{molecule}}$ the zero point energy correction, which was calculated within the harmonic approximation. For the adsorption of hydrogen $E_{\mathrm{bind,H}}$ was calculated through

$$E_{\mathrm{bind,H}} = \frac{1}{N_{\mathrm{ads,H}}}\left(E^{\mathrm{tot}}_{\mathrm{ad}} - E^{\mathrm{clean}}_{\mathrm{slab}} - \frac{N_{\mathrm{ads,H}}}{2}E^{\mathrm{gas+ZPE}}_{\mathrm{H_2}}\right), \tag{5.2}$$

where $E^{\mathrm{tot}}_{\mathrm{ad}}$ is the total energy of the surface slab + adsorbates and $E^{\mathrm{clean}}_{\mathrm{slab}}$ the total energy of the surface slab. Analogously, the energy for the adsorption of a single water molecule was calculated with

$$E_{\mathrm{bind,H_2O}} = E^{\mathrm{tot}}_{\mathrm{ad}} - E^{\mathrm{clean}}_{\mathrm{slab}} - E^{\mathrm{gas+ZPE}}_{\mathrm{H_2O}}. \tag{5.3}$$

Due to the instability of the OH molecule in the gas phase, the reference for the OH adsorption was expressed through the energies of gas phase H_2 and H_2O:

$$E_{\mathrm{bind,OH}} = E_{\mathrm{ad}}^{\mathrm{tot}} - E_{\mathrm{slab}}^{\mathrm{clean}} - \left(E_{\mathrm{H_2O}}^{\mathrm{gas+ZPE}} - \frac{1}{2} E_{\mathrm{H_2}}^{\mathrm{gas+ZPE}} \right), \tag{5.4}$$

For the adsorbed molecules, the ZPE on the surface was also taken into account. The energy barriers for diffusion and dissociation processes were determined using the climbing-image nudged-elastic-band method (CI-NEB) [99, 100] with a total number of seven images. The initial diffusion pathways were created by a linear interpolation between initial and final states and the forces were allowed to relax until the force convergence criterion of 0.01 eV/Å was met. The transition states were confirmed through the presence of only one imaginary frequency. By calculating the vibration frequencies within the harmonic approximation, the transition states were confirmed by the presence of only one imaginary frequency.

While the local maxima of a many-electron systems charge distribution occurs in most cases only at the positions of nuclei, it has been shown that clusters of alkali metals often exhibit non-nuclear maxima. The widely used localized charge partitioning according to Bader divides the electron cloud into non-overlapping compartments, which are separated by zero-flux surfaces and ideally contain only one nucleus . Due to non-atomic Bader compartments in materials with non-nuclear attractors, a Bader partitioning in such cases does not correspond to a division into atomic electron distributions, resulting in undefined net atomic charges. Taking into account nuclear and valence electrons, the net atomic charges were therefore assigned via density-derived electrostatic and chemical (DDEC6) atomic population analysis [96, 97] as it also provides trustworthy results even for materials with non-nuclear attractors .

5.4 Results and discussion

5.4.1 Hydrogen adsorption/absorption energies

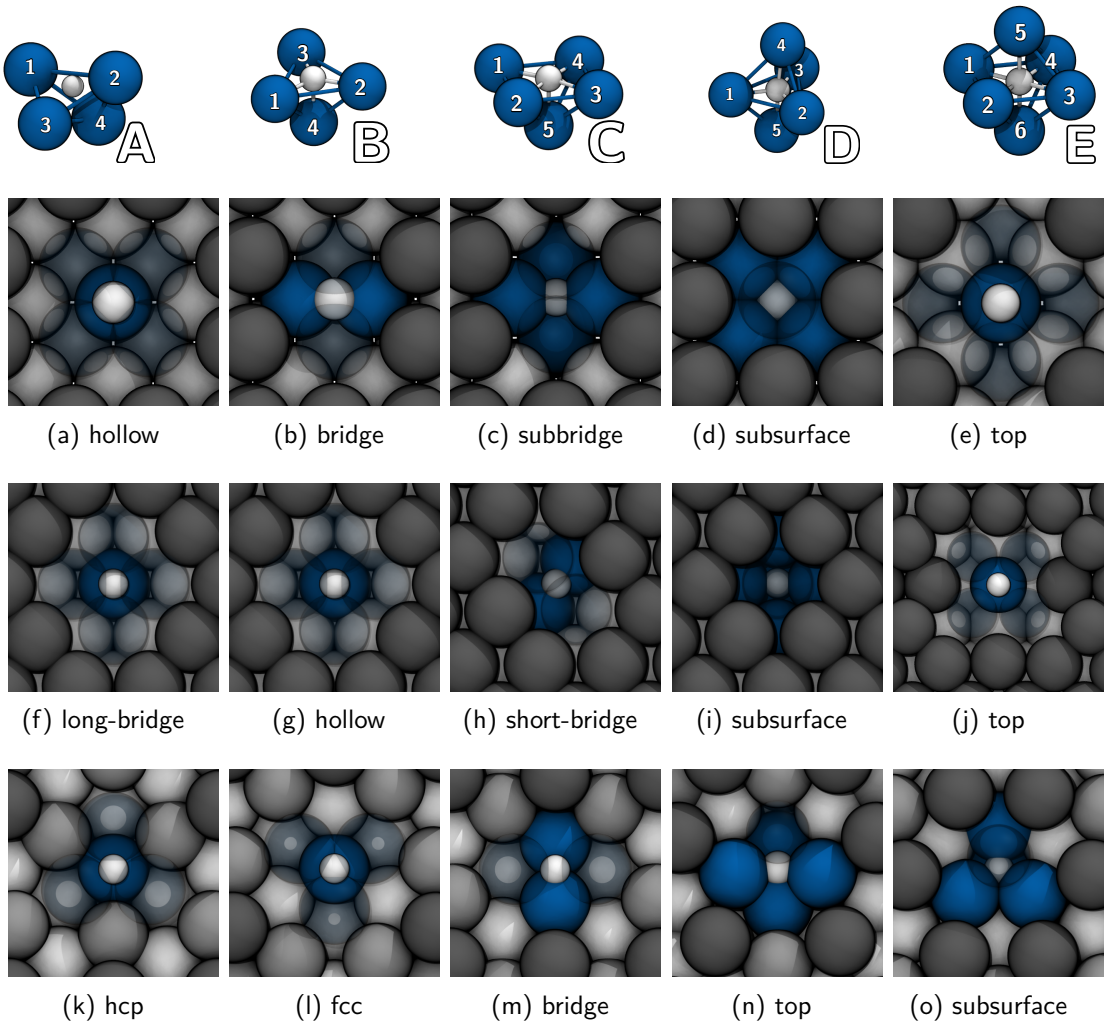

Figure 5.2. Surface structures of absorbed hydrogen on different adsorption sites on the low-index surfaces Li(100) in **(a)**−**(e)**, Li(110) in **(f)**−**(j)** and Li(111) in **(k)**−**(o)**. Lithium atoms of different layers are portrayed in different shades of grey. Hydrogen is shown in white and the coordinating lithium atoms in blue. The graphic above is an exemplary depiction of the different cluster-like coordinations, which were formed on the absorption of hydrogen on the different lithium surfaces.

Table 5.1 Binding energies per atom $E_{\mathrm{bind,H}}$ on the Li(100), Li(110) and Li(111) surface. The energies are referenced to a H_2 molecule in the gas phase and are reported in eV. The charge that was transferred to hydrogen on its absorption was analyzed within the DDEC6 charge methodology [96, 97] and is reported in e/atom.

(*hkl*)	Adsorption site	$E_{\mathrm{bind,H}}$	Type	$Q_{\mathrm{DDEC6,H}}$
	hollow	-0.67	**C**	-0.58
	bridge	-0.64	**A**	-0.67
Li(100)	*subbridge*	-0.52	**E**	-0.64
	subsurface	-0.48	**E**	-0.62
	top	0.27	**C**	-0.59
	hollow	-0.75	**C**	-0.60
	long-bridge	-0.75	**C**	-0.60
Li(110)	*short-bridge*	-0.49	**A**	-0.72
	subsurface	-0.58	**E**	-0.63
	top	-0.21	**C**	-0.58
	hcp	-0.89	**B**	-0.66
	fcc	-0.59	**B**	-0.67
Li(111)	*bridge*	-0.78	**A**	-0.66
	subsurface	-0.49	**C**	-0.67
	top	-0.78	**D**	-0.63

Since the moisture-induced corrosion of metallic lithium occurs through the cleavage of water molecules, we first investigated the interaction between monoatomic hydrogen and low-index lithium surfaces Li(100), Li(110) and Li(111). To characterize the effects of monoatomic hydrogen adsorption on the structure and stability of the lithium surfaces, we have examined the adsorption/absorption on the highly symmetric sites above and below the surfaces (*i.e.* subsurface). As can be seen in Fig. 5.2, the interaction of monoatomic hydrogen and metallic lithium led to the formation of cluster-like structures. An analogous formation of well-defined cluster structures on lithium has already been observed for oxygen in our previous studies [68]. In particular, adsorption at the corresponding *top* positions of all surfaces has shown a strong tendency to form square-pyramidal complexes in which the surrounding lithium atoms are pulled out of the surface plane. The binding energies in Table 5.1 show that almost all investigated structures are thermodynamically stable with respect to the respective clean lithium surfaces and molecular H_2 (in the gas phase). With a binding energy of 0.27 eV, $\mathrm{Li}(100) - \mathrm{H_{top}}$ turned out to be the only unstable structure,

that is, H-adsorption from H_2 is not likely. However, with atomic hydrogen as a reference, the $\mathrm{Li}(100) - \mathrm{H}_{\mathrm{top}}$ structure had a binding energy of -1.86 eV. Although being the thermodynamically least favoured structure, hydrogen in $\mathrm{Li}(100) - \mathrm{H}_{\mathrm{top}}$ had a similar five-fold, square-pyramidal, coordination as in $\mathrm{Li}(100) - \mathrm{H}_{\mathrm{hollow}}$, which (with -0.67 eV) is the most stable structure on Li(100). In comparison to $\mathrm{Li}(100) - \mathrm{H}_{\mathrm{hollow}}$, $\mathrm{Li}(100) - \mathrm{H}_{\mathrm{bridge}}$ had an almost identical binding energy of -0.64 eV. In this structure, hydrogen is surrounded by four lithium atoms in a tetrahedral arrangement, which was the lowest coordination for hydrogen in this study. With a very low energy difference of 0.03 eV, $\mathrm{Li}(100) - \mathrm{H}_{\mathrm{hollow}}$ and $\mathrm{Li}(100) - \mathrm{H}_{\mathrm{bridge}}$ were nearly degenerate. The *subsurface* and *subbridge* positions correspond to absorption sites under the Li(100) surface. The $\mathrm{Li}(100) - \mathrm{H}_{\mathrm{subbridge}}$ was by 0.12 eV less stable than $\mathrm{Li}(100) - \mathrm{H}_{\mathrm{bridge}}$. As hydrogen has been positioned below the surface in $\mathrm{Li}(100) - \mathrm{H}_{\mathrm{subbridge}}$, it is arranged in an octahedral, sixfold coordination, which was the highest coordination in this study. This coordination was also adopted in $\mathrm{Li}(100) - \mathrm{H}_{\mathrm{subsurface}}$, which had a binding energy of -0.49 eV. Interestingly enough, hydrogen in $\mathrm{Li}(100) - \mathrm{H}_{\mathrm{subbridge}}$ and $\mathrm{Li}(100) - \mathrm{H}_{\mathrm{subsurface}}$ is connected to the same number of lithium atoms as in rock-salt structured lithium hydride (LiH), which crystallizes in the cubic $\mathrm{Fm}\bar{3}\mathrm{m}$ spacegroup at ambient temperatures and pressures. The geometries of $\mathrm{Li}(100) - \mathrm{H}_{\mathrm{subsurface}}$ and $\mathrm{Li}(100) - \mathrm{H}_{\mathrm{subbridge}}$ thus already showed structural similarities to those in LiH, where a periodic mixture of edge- and corner-sharing Li/H octahedra builds up the crystal structure. With a small difference of only 0.04 eV compared to the *subsurface*, the *subbridge* is the most stable position below the Li(100) surface. However, adsorption on the surface into $\mathrm{Li}(100) - \mathrm{H}_{\mathrm{hollow}}$ is still by 0.15 eV more stable than below the surface in $\mathrm{Li}(100) - \mathrm{H}_{\mathrm{subbridge}}$.

Hydrogen adsorption in the *hollow* and *long-bridge* position on Li(110) resulted in the formation of the same structure, which in the following will only be referred to as $\mathrm{Li}(110) - \mathrm{H}_{\mathrm{long-bridge}}$. With a binding energy of -0.75 eV, the $\mathrm{Li}(110) - \mathrm{H}_{\mathrm{long-bridge}}$ is the most stable structure on Li(110). Here the absorbed hydrogen is once again located in a square pyramidal cluster. Although hydrogen occupied the same five-fold, square pyramidal coordination in the $\mathrm{Li}(110) - \mathrm{H}_{\mathrm{top}}$ structure, the adsorption on the *top* site was by 0.54 eV less stable than into the *long-bridge*. With a binding energy of -0.21 eV, the $\mathrm{Li}(110) - \mathrm{H}_{\mathrm{top}}$ is thus the least stable structure on Li(110). $\mathrm{Li}(110) - \mathrm{H}_{\mathrm{short-bridge}}$, where hydrogen was found in a tetrahedral coordination below

the surface, has a binding energy of -0.49 eV. Absorption into the $\mathrm{Li}(110) - \mathrm{H}_{\mathrm{subsurface}}$ structure resulted in a binding energy of -0.58 eV, making it the most stable structure under the Li(110) surface. In $\mathrm{Li}(110) - \mathrm{H}_{\mathrm{subsurface}}$ hydrogen is surrounded by six lithium atoms in an octahedral fashion. Compared to the thermodynamically most preferred $\mathrm{Li}(110) - \mathrm{H}_{\mathrm{long-bridge}}$, the storage of hydrogen below the surface was therefore only 0.17 eV less favourable. On Li(100) and Li(110), the respective lithium environment enforced the formation of similar coordination geometries for hydrogen.

The hexagonal packing of the Li(111) surface layer atoms on the other hand permitted the formation of trigonal pyramidal clusters on the adsorption at *hcp* and *fcc*, and a trigonal bipyramidal cluster for hydrogen below the Li(111) surface in the *subsurface* position. For Li(111), *hcp* adsorption has the strongest binding (-0.89 eV). Despite comparable coordination geometries, the absorption of hydrogen in $\mathrm{Li}(111) - \mathrm{H}_{\mathrm{hcp}}$ was by 0.30 eV preferred compared to $\mathrm{Li}(111) - \mathrm{H}_{\mathrm{fcc}}$. With respect to $\mathrm{Li}(111) - \mathrm{H}_{\mathrm{hcp}}$, the incorporation of hydrogen below the surface into the $\mathrm{Li}(111) - \mathrm{H}_{\mathrm{subsurface}}$ is by 0.40 eV less stable. On Li(111) adsorption at the *bridge* position again resulted in a fourfold coordinated tetrahedral environment, and when deposited on the *top* position on Li(111), the hydrogen atom slipped into a five-fold, square-pyramidal configuration. The configurations $\mathrm{Li}(111) - \mathrm{H}_{\mathrm{bridge}}$ and $\mathrm{Li}(111) - \mathrm{H}_{\mathrm{top}}$ each had a binding energy of -0.78 eV, and were with a difference of 0.11 eV compared to $\mathrm{Li}(111) - \mathrm{H}_{\mathrm{hcp}}$ the second most stable structures on Li(111). Due to lithium's low standard electrode potential, it was not surprising that adsorption/absorption occurred under the transfer of a high amount of negative charge to the hydrogen atom. As can be seen in Table 5.1, a DDEC6 analysis for the absorption complexes revealed that the charge of hydrogen at the metallic lithium surfaces is in a comparable order of magnitude to that within bulk-lithium-hydride in its rocksalt phase (the DDEC6 net-charge for hydrogen in LiH bulk was $+0.78\ e$/atom).

Under the inclusion of the surrounding lithium atoms, atomic hydrogen thus forms negatively charged, hydride-like centres on the lithium, which are also thermodynamically stable below the surface. With its concentrated negative charge, the absorbed monoatomic hydrogen consequently represents a potential target for intermolecular interactions.

5.4.2 Mobility of Hydrogen on Li(100) and Li(*bcc*)

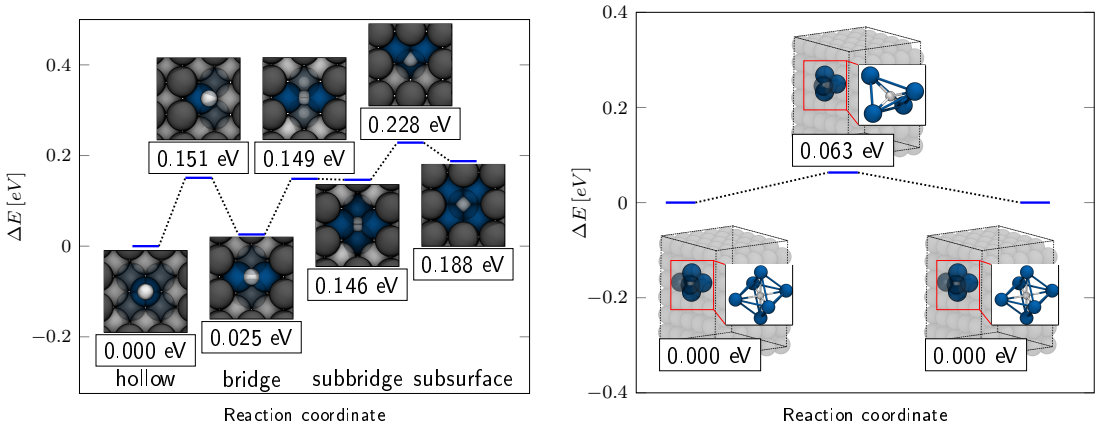

(a) Diffusion profile for an hydrogen atom on Li(100)

(b) Diffusion profile for an hydrogen atom through Li(bcc)-bulk

Figure 5.3. Energy profiles for the diffusion of a hydrogen atom on the Li(100) surface and in the bulk material. The energy profile in **(a)** shows the diffusion pathway on Li(100) from a *hollow* site into a neighbouring *subsurface* position, by crossing an adjacent *bridge* and *subbridge* position. The framed values indicate the relative energy in eV, which were related to the most stable *hollow* structure. The energy profile for the diffusion of a hydrogen atom through the Li(*bcc*)-bulk structure is shown in **(b)**. In bulk-lithium hydrogen diffuses from an octahedrally-coordinated environment via a tetrahedral transition state to an equivalent octahedrally-coordinated. Shown are the structures of the octahedrally coordinated initial and final configurations, as well as the tetrahedral transition state. The framed values indicate relative energies related to the octahedrally-coordinated structure.

Our investigations on Li(100) have shown that absorption in the *hollow* and *bridge* positions is almost degenerate, and that H adsorption below the surface is by only 0.14 eV less stable than on the surface. To evaluate the mobility of hydrogen on the surface and the embedding under the surface, the energy barriers for the diffusion of a hydrogen adatom between *hollow*, *bridge* and *subsurface* were determined. The energy profile for monoatomic surface diffusion is given in Fig. 5.3a, where the energies of the transition states are related to the energy of the most stable $\mathrm{Li}(100) - \mathrm{H}_{\mathrm{hollow}}$

structure. As can be seen from the diffusion barriers in Table 5.2, the movement of an adsorbed hydrogen atom is associated with low diffusion barriers. Starting from the *hollow* position, hydrogen can diffuse almost unhindered into the *bridge* position with a barrier of only 0.151 eV. With 0.126 eV for the reverse process diffusion from the *bridge* to a more stable, neighbouring *hollow* position is even easier. In the transition state, hydrogen is surrounded (in a trigonal fashion) by two lithium atoms from the surface and one from the second layer. Moving from the tetrahedron-like environment of the *bridge* position on the surface, hydrogen could penetrate into the surface by diffusing into the *subbridge* position. The entry into the *subbridge* position possesses a low barrier of merely 0.124 eV. Interestingly, with a small barrier of only 0.003 eV, the reverse process of the *subbridge* into the *bridge* position is almost barrier-free. Diffusion from *subbridge* into *subsurface* occurred via a barrier of 0.082 eV within a tetrahedral coordinated transition state. The reverse diffusion into the *subbridge* position is correspondingly lower with 0.040 eV. Although the positions above the Li(100) surface were thermodynamically more stable, storage of hydrogen in the bulk material is in principle possible from a thermodynamic point of view, due to extremely low barriers. We, therefore, investigated the diffusion of hydrogen within the bulk material, where the hydrogen atom can occupy octahedral cavities, which are basically a continuation of the *subbridge*/*subsurface* adsorption sites of Li(100). Here, in the transition state for the diffusion between the cavities, hydrogen is again surrounded by four lithium atoms and assumes a tetrahedron-like geometry. With a low barrier of 0.063 eV, atomic hydrogen can therefore not only migrate almost freely on the surface layer and penetrate the lattice by overcoming a modest activation barrier but also shows a very high degree of mobility in the bulk material.

To evaluate the presence of atomic hydrogen, we have studied the dissociation of molecular hydrogen on Li(100). As can be seen in Fig. 5.4 and Table 5.3, molecular hydrogen adsorbs only weakly with a binding energy of only -0.03 eV on the *top* position of Li(100). The low binding energy is also expressed by a comparatively low charge of 0.06 *e* per molecule, which is transferred from lithium to the adsorbed H_2 molecule. With 0.76 Å, the bond length is also close to that of an isolated molecule ($d_{\mathrm{H_2}} =$ 0.75 Å). From the *top* position, a pathway was found, where molecular hydrogen dissociated into two adjacent *bridge* positions. The dissociation takes place via a transition state, which lies 0.271 eV above the adsorbed hydrogen on the *top* position. In this transition state, molecular hydrogen has an increased bond length of 0.88 Å and

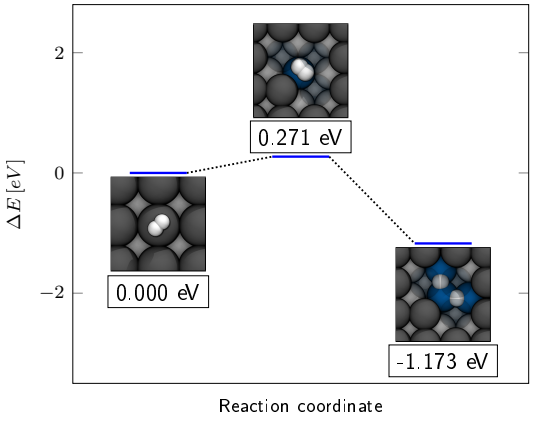

Figure 5.4. Energy profile for the dissociation of molecular hydrogen into two adjacent *bridge* positions on Li(100). The framed values indicate the relative energy related to the Li(100)-H_2 adsorption complex.

lies transversely in the corner of a *hollow* position. Dissociation leads to a structure, which is by 1.173 eV more stable than the initial structure. As the partially negatively charged, monoatomic hydrogen absorbate has high mobility on the lithium surface and in the bulk material it can rush over (and through) the material until it encounters other surface contaminants with which it can interact. Molecular H_2 exhibits a low dissociation barrier but may also desorb readily due to its weak binding to the Li(100) surface.

Table 5.2 ΔE_{back} and ΔE_{for} barriers in eV for the respective backward and forward diffusion/dissociation processes of hydrogen on the Li(100) surface and in Li(bcc) bulk.

Process			ΔE_{for}	ΔE_{back}
Li(100)-H_{hollow}	$\longrightarrow$	Li(100)-H_{bridge}	0.151	0.126
Li(100)-H_{bridge}	$\longrightarrow$	Li(100)-$H_{\mathrm{subbridge}}$	0.124	0.003
Li(100)-$H_{\mathrm{subbridge}}$	$\longrightarrow$	Li(100)-$H_{\mathrm{subsurface}}$	0.082	0.040
Li(100)-$H_{2,\mathrm{top}}$	$\longrightarrow$	Li(100)-$2H_{\mathrm{bridge,bridge}}$	0.271	1.444
Li(bcc)-$H_{\mathrm{bulk},1}$	$\longrightarrow$	Li(bcc)-$H_{\mathrm{bulk},2}$	0.063	0.063

5.4.3 Mobility and dissociation of OH on Li(100)

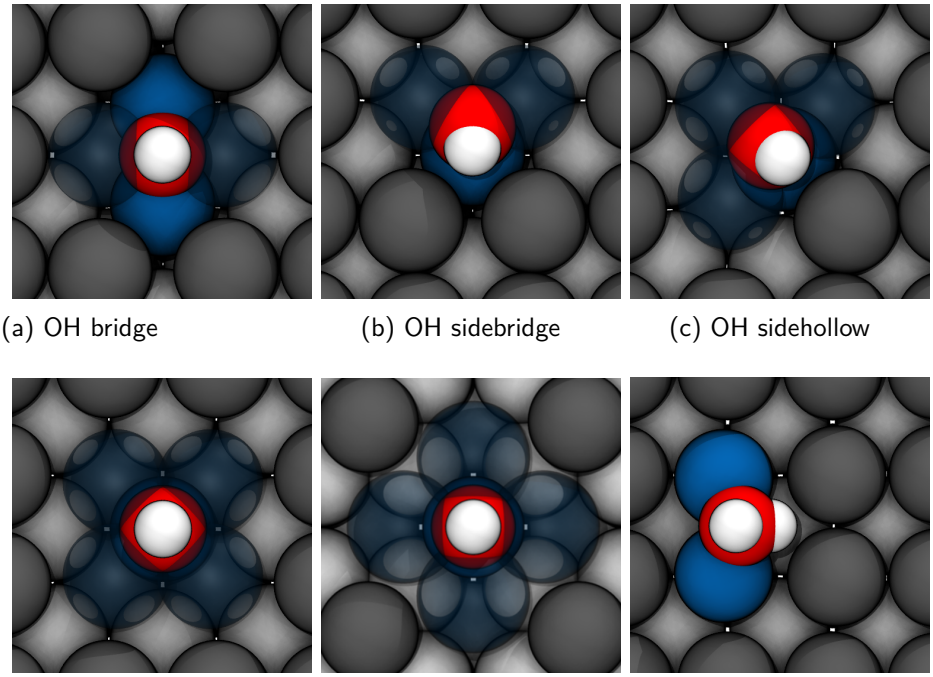

(a) OH bridge (b) OH sidebridge (c) OH sidehollow

(d) OH hollow (e) OH top (f) H_2O bridge

Figure 5.5. Top view of the different absorption complexes of an OH molecule in **(a)**−**(e)**, and **(f)** the adsorption structure of H_2O on Li(100). Hydrogen is shown in white, oxygen in red and the coordinating lithium atoms in blue.

To examine the essential interactions between lithium and an OH molecule, individual OH molecules were placed on the high symmetrical *hollow*, *bridge* and *top* adsorption sites of Li(100). Here, too, the formation of the *top* structure takes place by tearing out the four surrounding lithium atoms out of the surface plane. By investigating the energy profile for the diffusion of an OH molecule between *bridge* and *hollow*, two further local minima could be identified. In the following, these two minima are referred to as *sidebridge* and *sidehollow*. Together with *hollow*, *bridge* and *top* structures, they are shown in Fig. 5.5. Overall, with a binding energy of -0.96 eV, the *top* position is by far the least favourable site for the OH absorption. Except for $\mathrm{Li(100)-OH_{top}}$,

Table 5.3 Binding energies per molecule $E_{\mathrm{bind,mol.}}$ on Li(100). The energies were related to the respective molecular species in the gas phase and are reported in eV.

(*hkl*)	Adsorption site	$E_{\mathrm{bind,mol.}}$	Q_{DDEC6}	
Li(100)-H_2	*top*	-0.03	H_a: 0.03;	H_b: 0.03
	hollow	-2.08	O: -0.96;	H: 0.33
	bridge	-2.02	O: -1.03;	H: 0.33
Li(100)-OH	*top*	-0.96	O: -1.01;	H: 0.34
	sidebridge	-2.06	O: -1.09;	H: 0.34
	sidehollow	-2.09	O: -1.03;	H: 0.32
Li(100)-H_2O	*bridge*	-0.78	O: -0.77;	H_{up}: 0.37 H_{down}: 0.12

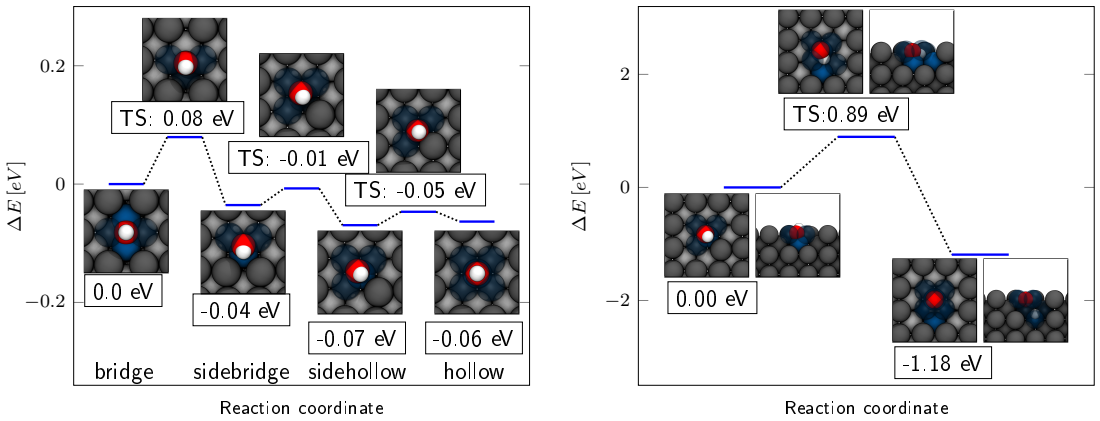

(a) Energy profile for the diffusion of an OH molecule on Li(100)

(b) Energy profile for the dissociation of an OH molecule on Li(100)

Figure 5.6. Energy profile for the diffusion of an OH molecule on Li(100) in **(a)**, which shows the transition from an OH-molecule in the *bridge* position towards the *hollow* site. In this diffusion process, the OH molecule passes through two local minima, which have been labelled as *sidebridge* and *sidehollow*. The framed values indicate the relative energy, which was related to the initial *bridge* structure. The energy profile for the dissociation of an OH molecule on Li(100) is shown in **(b)**. The pathway shows an OH molecule in the *sidehollow* position releasing its hydrogen atom to the opposite *bridge* position. The framed values indicate the relative energies, which are related to the undissociated OH *sidehollow* absorption complex.

the other absorption structures exhibit very small energy differences, as can be seen from the binding energies in Table 5.3. Unsurprisingly, the small energy differences are accompanied by an extremely flat energy profile with low diffusion barriers, which is shown in Fig. 5.6a. The energy barriers for the diffusion and dissociation of OH as well as water are summarized in Table A.4.

After $\mathrm{Li}(100) - \mathrm{OH}_{\mathrm{top}}$, the $\mathrm{Li}(100) - \mathrm{OH}_{\mathrm{bridge}}$ structure is the least stable structure, with a binding energy of -2.02 eV. In this configuration, the OH molecule is coordinated by a total of four lithium atoms. The diffusion into the 0.04 eV more stable *sidebridge* proceeds via a barrier of 0.08 eV. Here, the OH molecule changes its configuration from a fourfold to a threefold lithium coordination. Although the barrier for the reverse process is with 0.12 eV remarkably low, the process for the diffusion into the *sidehollow* position is preferred, with an even lower barrier of only 0.03 eV. In the *sidehollow* position, the OH molecule is surrounded by a total of four lithium atoms. From this position, the OH molecule could either diffuse back into the 0.03 eV less stable *sidebridge* via a barrier of 0.06 eV, or into the *hollow* position with a barrier of only 0.02 eV. In the *hollow* position, the OH molecule is surrounded by six lithium atoms. The *hollow* position is energetically nearly equal to the *sidehollow*, as they differ by only 0.01 eV. The low energy differences between the individual structures and the flat diffusion profile demonstrate an almost barrier-free transition between the structures and a high mobility of the OH molecule on Li(100).
The investigation of various processes for the decomposition of the OH molecule using the CI-NEB (climbing image-nudged elastic band) method has shown that dissociation into oxygen and hydrogen from one of the considered absorption compounds is preceded by diffusion into the *sidehollow* site. Here, the geometry of the *sidehollow* allows a simple dissociation of the H-atom into the 1.84 Å distant *bridge* position. In comparison, the closest unoccupied *bridge* position is 2.01 Å apart from the hydrogen atom in the *sidebridge* site. The actual dissociation process is therefore observed after the diffusion into the *sidehollow*. The dissociation of the OH molecule takes place through the release of the hydrogen atom into an adjacent *bridge* position via a barrier of 0.89 eV as shown in Fig. 5.6b. Particularly noteworthy is the high energy difference of 1.38 eV between the absorbed OH molecule and the dissociated complex. Despite a comparably high barrier, splitting of the OH molecule on the surface is thus (thermodynamically) associated with a high energy gain. The high energy difference is a result of hydrogen and oxygen atoms forming very stable complexes in their respective

hollow configurations. Through the attraction of the surrounding surface atoms, OH molecules form stable absorption complexes on the lithium surface, which lie in a similar stability range. Here, the low barriers for diffusion allow an almost unhindered movement of the OH molecule through the lithium surface. The dissociation of the OH molecule itself is exothermic, but the cleavage is associated with a (comparatively) high reaction barrier.

5.4.4 Mobility and dissociation of water on Li(100)

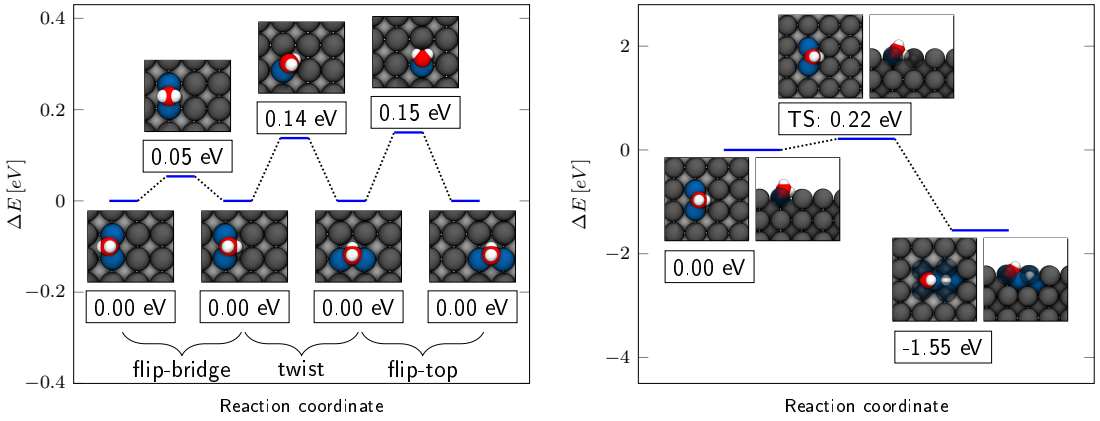

(a) Energy profile for the diffusion of H_2O on Li(100)

(b) Energy profile for the dissociation of H_2O on Li(100)

Figure 5.7. The energy profile in **(a)** shows the diffusion of a H_2O molecule on Li(100) from one *bridge* to another (via flip and twist mechanism) and the diffusion from a *bridge* position to a *top* position. The relative energies in the framed values are referred to the H_2O molecule in the Li(100) *bridge* position. The energy profile for the dissociation of an H_2O molecule on Li(100) is shown in **(b)**. The pathway shows a H_2O molecule in the *bridge* position releasing one of its hydrogen atoms into the opposite *bridge* position. The framed relative energies are related to the undissociated H_2O *bridge* adsorption complex.

On Li(100) the water molecule adsorbs on the *bridge* position (as shown in Fig. 5.5f), where it adsorbs with a binding energy of -0.77 eV. In this structure, one hydrogen (H_{up}) is directed away from the surface while the other one (H_{down}) points to a *hollow*

position on Li(100). The O−H bond length to H_{up} is with 0.98 Å very close to the bond length of 0.97 Å in the isolated water molecule. In contrast, the O−H bond length to H_{down} was slightly stretched to a value of 1.02 Å. Compared to the isolated molecule the H−O−H angle of the adsorbed water has widened slightly from 104.48° to 106.93°. Although both hydrogen atoms in the adsorbed water molecule are partially positively charged, the net charge for H_{down} is with 0.12 e/atom slightly lower than the 0.37 e/atom of H_{up}. The smaller positive charge of H_{down} can be explained by the proximity to the reducing lithium surface, which already could have increased its electron density. This can also be seen in Fig. 5.9h, where an increase of the electron density was noticed in front of the H_{down} atom. As in isolated water, oxygen was with -0.78 e/atom partially negatively charged. Here, the water molecule is slightly tilted in such a way that one hydrogen atom is minimally closer to the lithium surface. The positive interaction energies of two water molecules in the appendix indicates repulsive interactions at lower coverages, due to the water molecules attracting the lithium of their bridge positions, which causes a slight tension on the surface.

Like the OH molecule, water also showed a pronounced mobility on Li(100). As shown in Fig. 5.7a the diffusion from one *bridge* position to another took place by either a "*flip*" or "*twist*" mechanism. The reversal of a water molecule on a *bridge* position from one side to the other via the *flip* mechanism is nearly unhindered, as the barrier for this process is merely 0.05 eV high. Diffusion between two adjacent *bridge* positions via the *twist* mechanism followed a path with a barrier of 0.14 eV. In the *flip-top* mechanism, the water molecule moved out of the *bridge* position over an adjacent *top* position with a barrier of 0.15 eV.

The dissociation of the water molecule on the *bridge* position took place via the release of H_{down} into the opposite, unoccupied *bridge* position. In this process, the water molecule decomposed into an OH molecule in the *sidebridge* configuration and a hydrogen atom in the opposite *bridge* position. In Fig. 5.7b it can be seen from the depictions in the energy profile, that hydrogen was released in a tilting movement of water towards the *bridge* position. In comparison to the OH dissociation, the water decomposition is characterized by a particularly low barrier of 0.22 eV. The dissociated structure is 1.89 eV more stable than the water adsorption complex. This high gain in stability illustrates the strongly exothermic nature of the lithium/water reaction.

Like adsorbed hydrogen atoms and OH molecules, water can advance to other species on the surface due to its high mobility on Li(100) and react with them even before its

dissociation. However, the low dissociation barrier of water shows that dissociation of the water molecule under the formation of an adsorbed hydrogen atom H_ad and an OH molecule can occur similar to the Volmer process in the alkaline medium even without additional adsorbates as shown in equation 5.5:

$$H_2O + e^- \longrightarrow OH^- + H_{ad} \tag{5.5}$$

Table 5.4 ΔE_{back} and ΔE_{for} barriers in eV for the respective backwards and forward diffusion, dissociation and reaction processes of OH and H_2O molecules on Li(100).

Process			ΔE_{for}	ΔE_{back}
Li(100)-$OH_{bri.}$	$\rightarrow$	Li(100)-$OH_{sidebri.}$	0.08	0.12
Li(100)-$OH_{sidebri.}$	$\rightarrow$	Li(100)-$OH_{sidehol.}$	0.03	0.06
Li(100)-$OH_{sidehol.}$	$\rightarrow$	Li(100)-$OH_{hol.}$	0.02	0.01
Li(100)-$OH_{sidehol.}$	$\rightarrow$	Li(100)-$O_{hol.}$ + $H_{hol.}$	0.89	2.27
Li(100)-$OH_{sidehol.}$ + $H_{bri.}$	$\rightarrow$	Li(100)-$O_{hol.}$ + $H_{2,top}$	0.40	0.61
Li(100)-$H_2O_{bri.,1}$ (flip-bridge)	$\rightarrow$	Li(100)-$H_2O_{bri.,2}$	0.05	0.05
Li(100)-$H_2O_{bri.,1}$ (twist)	$\rightarrow$	Li(100)-$H_2O_{bri.,2}$	0.14	0.14
Li(100)-$H_2O_{bri.,1}$ (flip-top)	$\rightarrow$	Li(100)-$H_2O_{bri.,2}$	0.15	0.15
Li(100)-$H_2O_{bri.}$	$\rightarrow$	Li(100)-$OH_{sidebri.}$ + $H_{bri.}$	0.22	2.11
Li(100)-$H_2O_{bri.}$ + $H_{bri.}$	$\rightarrow$	Li(100)-$OH_{sidebri.}$ + $H_{2,top}$	0.06	0.66

5.4.5 Hydrogen evolution on Li(100)

A complete reaction of water with lithium leads to the formation of LiOH and H_2. Evidently, the remaining hydrogen atom must recombine with another hydrogen atom for H_2 evolution to occur. So far, our studies on the diffusion of different species have suggested a high mobility on Li(100) due to low diffusion barriers, and a low barrier for the dissociation of water. Due to the high mobility, it is therefore likely that the different species can meet on the surface, leading to the evolution of molecular hydrogen in case of suitable encounters. In the following, we have considered the development of H_2 through an absorbed hydrogen atom, which recombines with either an adsorbed OH or water molecule. In addition, we have also considered the recombination of two absorbed hydrogen atoms. The latter process effectively corresponds to the reversal of the energy profile for the hydrogen dissociation in Fig. 5.4. For the recombination of a

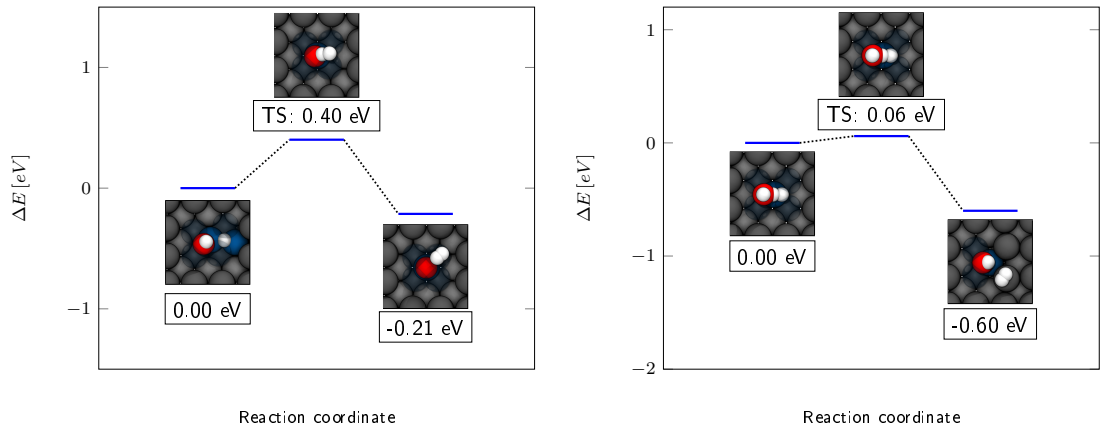

(a) Energy profile for the reaction of OH and a hydrogen atom on Li(100)

(b) Energy profile for the reaction of H_2O and a hydrogen atom on Li(100)

Figure 5.8. The energy profile in **(a)** shows the hydrogen evolution through the reaction of a hydrogen atom in the *bridge* position with an OH molecule and **(b)** with a H_2O molecule on Li(100). Both profiles show the dissociation of the respective molecule under the release of one of their hydrogen atoms towards the adsorbed hydrogen atom. The framed relative energies are related to the respective undissociated structures.

H atom with an OH molecule, atomic hydrogen $\mathrm{H_{bridge}}$ was positioned in the *bridge* position in front of an OH molecule in the *sidehollow*, as shown in Fig. 5.9c. The distance between $\mathrm{H_{OH}}$ in the OH molecule and the absorbed $\mathrm{H_{bridge}}$ was 2.83 Å. Fig. 5.9g shows, that the positively charged $\mathrm{H_{OH}}$ stands directly opposite to the partially negatively charged $\mathrm{H_{bridge}}$. The respective DDEC6 charges were 0.36 e/atom for $\mathrm{H_{OH}}$ and -0.72 e/atom for $\mathrm{H_{bridge}}$. In the final structure in Fig. 5.9k the hydrogen molecule was located on the corner atom of an absorbed oxygen atom which was absorbed in the *hollow* position. The adsorption energy of H_2 on the oxygen absorption complex was with -0.03 eV equally low as on pure lithium. The recombination of $\mathrm{H_{bridge}}$ and $\mathrm{H_{OH}}$ to molecular hydrogen took place as shown in Fig. 5.8a via a barrier of 0.40 eV. Thus, the barrier for the recombination was by 0.49 eV lower than the decomposition of the OH molecule on the lithium surface. From a thermodynamic point of view, the formation of H_2 through OH and absorbed hydrogen resulted in a stability gain. Since the adsorbed H_2 molecule had a negligibly low adsorption energy, the final structure was mainly stabilized through a $\mathrm{Li(100) - O_{hollow}}$ complex. The hydrogen evolution through the water molecule was investigated with the structure shown in

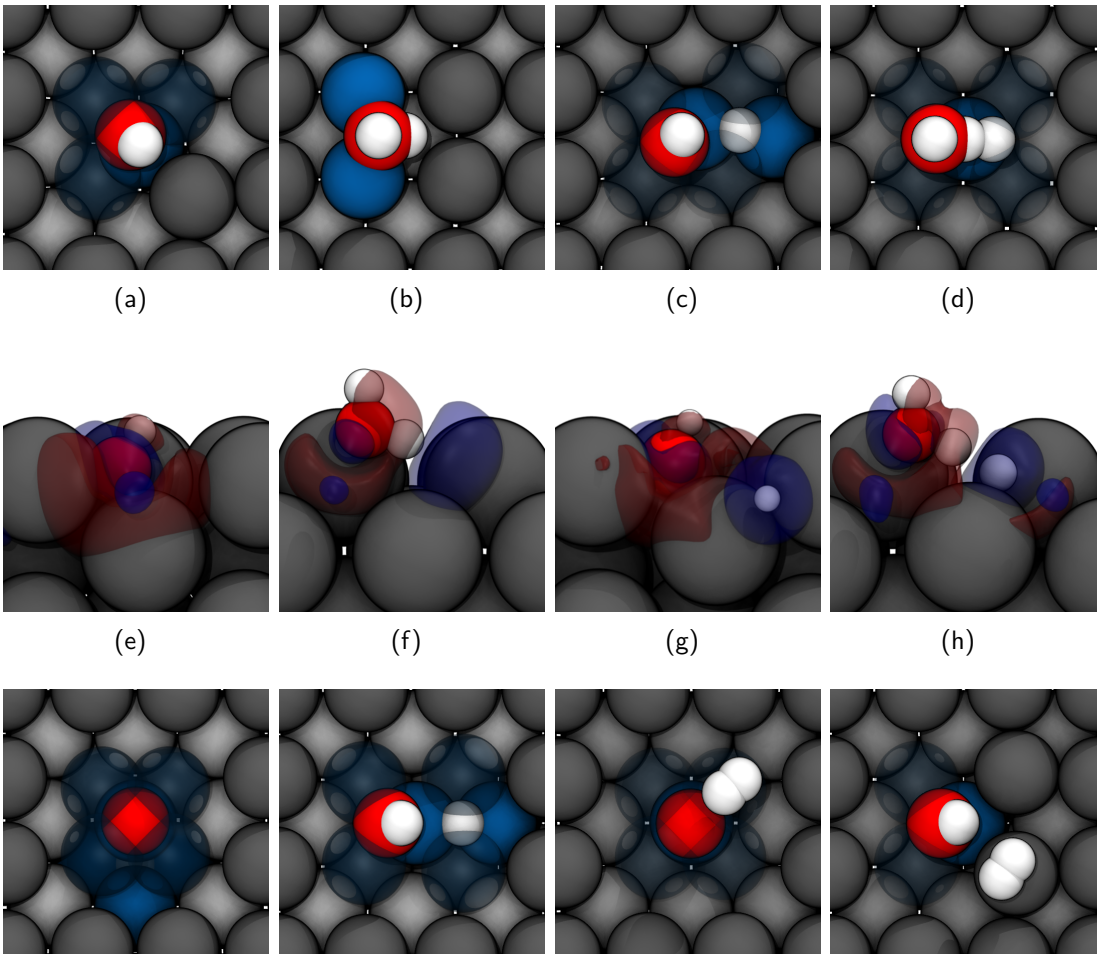

Figure 5.9. Top view of the undissociated adsorption/absorption complexes of OH and H_2O on Li(100) in **(a)**−**(b)** and the respective complexes in the presence of a hydrogen atom in **(c)**−**(d)**. The figures in **(e)**−**(h)** show the charge density difference isosurfaces of the corresponding undissociated structures. Blue regions indicate an increase and red regions a decrease in electron density. The illustrations **(i)**−**(j)** show the top view of the dissociated OH and water molecule on Li(100) and **(k)**−**(l)** the corresponding structures in the presence of the generated H_2 molecule.

Fig. 5.9d. In this configuration, the hydrogen atom $\mathrm{H_{bridge}}$ was absorbed laterally from the normal *bridge* position and shifted towards the adsorbed water molecule on the opposite *bridge* position. The distance between $\mathrm{H_{bridge}}$ and the downward-facing hydrogen atom $\mathrm{H_{water}}$ of the adsorbed water molecule was therefore only 1.29 Å.

Analogous to the corresponding OH structure, a partially positively charged $\mathrm{H_{water}}$ and a partially negatively charged $\mathrm{H_{bridge}}$ were located opposite to each other in this structure. For $\mathrm{H_{water}}$ and $\mathrm{H_{bridge}}$ net charges of 0.31 e/atom and -0.56 e/atom were found respectively. In the final structure in Fig. 5.9l the OH molecule was in the *sidebridge* configuration and the hydrogen molecule with only -0.02 eV weakly bound to an opposing *top* position. Remarkable was the extremely low barrier of 0.06 eV for the dissociation of the water molecule under the formation of molecular hydrogen. This barrier was thus 0.16 eV lower than the already low barrier for the pure dissociation of the water molecule. As can be seen in the appendix, the analogous process with an H atom on the side also exhibits with 0.14 eV a lower barrier for the cleavage of water. The thermodynamic gain in stability of 0.60 eV was in this case also mainly due to the formation of a $\mathrm{Li(100) - OH_{sidebridge}}$ complex. Compared to the simple cleavage of H_2O and OH, the recombination processes showed significantly lower barriers. An analysis of the charge distribution has shown, that this can be explained by the fact that during recombination a negatively charged hydrogen faced a partially positively charged hydrogen in the molecule, as it is shown in Figs. 5.9g and 5.9h. Both during hydrogen development via an OH or water molecule, a thermodynamic driving force exists via the formation of stable surface complexes. Investigating the energy path for the H_2 dissociation from Fig. 5.4 clarifies that the recombination of two absorbed hydrogen atoms is unlikely.

A hydrogen evolution reaction (HER) through absorbed hydrogen atoms $\mathrm{H_{ab}}$ according to a homolytic, Tafel-like mechanism as shown in equation 5.6 can therefore be excluded as the main mechanism for the HER:

$$\mathrm{H_{ab} + H_{ab} \longrightarrow H_2} \tag{5.6}$$

Instead of the Tafel process, a Heyrovsky-like step according to equation 5.7 turns out to be the decisive process for the H_2 development on Li(100):

$$\mathrm{H_2O + H_{ab} \longrightarrow OH^- + H_2} \tag{5.7}$$

During initial degradation, the recombination reactions of OH or water with an adsorbed hydrogen can therefore be seen as the cause of the HER. Due to the low reaction barrier of the recombination reactions, it is likely that the partially negatively charged hydrogen

centres can be regarded as reaction centres of hydrogen development. Therefore, an increased hydrogen concentration on the surface (*e.g.*, due to the preceding cleavage of OH or water molecules) would result in an enhanced hydrogen evolution.

5.5 Conclusion

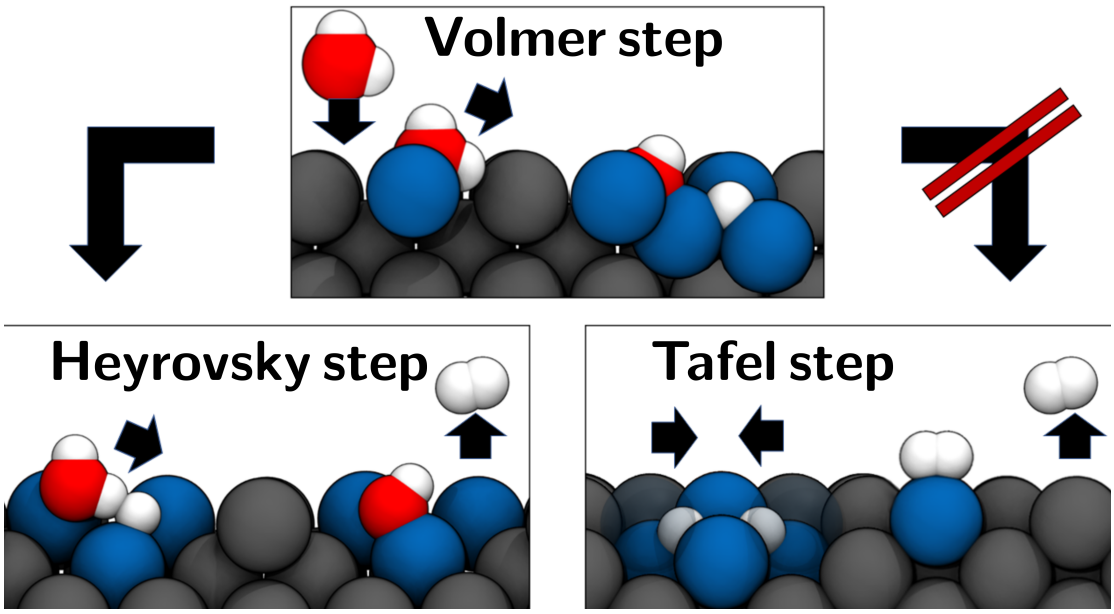

Figure 5.10. Schematic representation of the steps in the HER on Li(100). In a Volmer-like step, a water molecule adsorbs on the lithium surface and dissociates to form an adsorbed hydrogen atom and OH molecule. Analogous to the Heyrovsky mechanism in an alkaline medium, another water molecule attacks the adsorbed hydrogen atom in the next step, forming an OH and H_2 molecule. In comparison, a recombination of two adsorbed hydrogen atoms according to the Tafel mechanism is unlikely.

In this work, we performed periodic density functional theory calculations to investigate the basic principles of water-induced lithium corrosion. The studies on the interaction between monoatomic hydrogen and the low-index surfaces Li(100), Li(110), and Li(111) have shown that hydrogen absorbs under the formation of cluster-like structures under a high negative charge transfer from lithium to the absorbate. Given the low differences in binding energy for different adsorption sites on and below the surface, our studies

have shown that diffusion of hydrogen on Li(100) and in Li-(*bcc*) bulk is characterized by high mobility. While monoatomic hydrogen is absorbed by the lithium surface, molecular hydrogen is only weakly adsorbed on the top position on Li(100) without significant charge transfer. The investigation of OH adsorption on Li(100) has shown that OH forms clusters, which are extremely stable from a thermodynamic point of view. Except for the $\mathrm{Li}(100) - \mathrm{OH}_{\mathrm{top}}$ structure (which still has a high binding energy of -0.96 eV) all OH absorption complexes exhibit very low energy differences and consequently shallow diffusion profiles with low barriers. Likewise, water molecules can move with a high mobility, via "flip" or "twist" mechanisms. Starting from a $\mathrm{Li}(100) - \mathrm{OH}_{\mathrm{bridge}}$ structure, a dissociation is possible according to a Volmer-like mechanism via the release of a hydrogen atom to an adjacent bridge position via a barrier of only 0.22 eV. Compared to OH, water is thermodynamically less stable (due to a much lower binding energy) and shows a significantly lower dissociation barrier. By forming different surface clusters on Li(100), the cleavage of the investigated molecules leads in all cases to a considerable gain in stability. From a thermodynamic point of view, the recombination of two absorbed hydrogen atoms via a Tafel process can therefore be excluded as a major source for hydrogen evolution, as illustrated in Fig. 5.10. Due to the surface clusters that are formed next to the weakly adsorbed H_2 molecule, the H_2 development via recombination of a hydrogen atom with either an OH or water molecule, on the other hand, leads to a gain in stability. Here, the barriers for hydrogen development analogous to the Heyrovsky mechanism in an alkaline medium via OH or water are considerably lower than the corresponding simple dissociation processes. The reason for the lower barriers can be found in the fact that the negatively charged hydrogen adsorbates are opposed to a partially positively charged hydrogen when they encounter an OH or water molecule on Li(100). The strong lowering of the dissociation barrier implies that there is a self-supporting effect for the cleavage of OH and water molecules when more hydrogen adsorbates are present on the lithium surface (*i.e.*, higher coverages). Due to the lower reaction barrier, water is to be seen as the main source of the hydrogen evolution reaction.

By breaking down the initial water-induced corrosion into individual steps, the foundation for a more systematic approach to the development of the metallic lithium anode may be facilitated. While most approaches to protect and delay water-induced corrosion of the anode follow the strategy of keeping the reactants away from the surface through low levels of humidity and/or coating of the surface, the identification of the negatively

charged hydrogen adsorbates as reaction centres may offer an additional means of control. Since these centres are crucial components in the Heyrovsky-type cleavage, new design principles could aim at chemically or sterically blocking the negatively charged hydrogen centres from further reacting. As fundamental experimental studies have already shown, the presence of water can have a significant effect on the reaction of lithium with other atmospheric gases such as O_2 or N_2.In particular, the formation of Li_3N must be mentioned here, which is highly enhanced by the presence of water.Since the respective degradation mechanisms with water are not known, further studies on water-induced degradation can possibly help to clarify these mechanisms and thus enable a more controlled pretreatment. While solvent effects are irrelevant during cell production, they have a decisive effect within a battery. However, a more advanced simulation should be carried out with the aid of an explicit solvent model since the decomposition of the electrolyte will have a decisive influence on the course of the reaction.

Acknowledgements

This work was supported by the German Research Foundation (DFG) under Project ID 390874152 (POLiS Cluster of Excellence) as well as the priority program SPP-2248. The authors acknowledge support by the High Performance and Cloud Computing Group at the Zentrum fur Datenverarbeitung of the University of Tübingen, the state of Baden-Württemberg through bwHPC and the German Research Foundation (DFG) through grant no INST 37/935-1 FUGG. Open Access funding enabled and organized by Projekt DEAL.

6

ReaxFF guided simulation of lithium anode oxidation

Matthias van den Borg [1, 2], Daniel Gaissmaier[1, 3, 4], Florian Fiesinger[1,], Edwin Knobbe[2] and Timo Jacob[1, 3, 4]

To be submitted.

[1] Institute of Electrochemistry, Ulm University, Albert-Einstein-Allee 47, D-89081 Ulm, Germany
[2] BMW Group, 80809 Munich
[3] Helmholtz-Institute Ulm (HIU) for Electrochemical Energy Storage, Helmholtzstr. 11, 89081 Ulm, Germany
[4] Karlsruhe Institute of Technology (KIT), P.O. Box 3640, 76021 Karlsruhe, Germany

6.1 Abstract

The availability of stable Li metal anodes is crucial for the successful implementation of many promising next-generation energy storage systems (*e.g.* Li-S or Li-air batteries). A crucial factor that determines the realization of these systems is the understanding and control of the passivating boundary layer that forms at the Li anode. For characterizing the first steps of Li degradation through O_2 impurities, we optimized ReaxFF force field parameters for the Li-O interaction, which is capable of portraying the transition from metallic lithium to Li_2O. Using Grand-Canical-Monte-Carlo (GCMC) simulations, the oxidation of lithium nanoparticles is used to illustrate the complete oxidation process from metallic lithium to the formation of amorphous suboxide structures to a crystalline Li_2O nanoparticle.

6.2 Introduction

Since their commercial introduction in the early 1990s [13], Li-ion batteries (LIBs) have advanced to become a key component for electric vehicles by offering a favourable combination of high energy and power density. Despite their successful implementation, however, it is questionable whether LIBs will meet the high requirements for next-generation energy storage systems in the future, as LIBs are slowly approaching the theoretical values of their anode/cathode materials. Ideally, modern batteries would utilize metallic lithium as anode material, as it is considered to be the ultimate negative electrode with respect to its high theoretical capacity (3862 mA h g^{-1}), high standard electrode potential [-3.040 V vs. standard hydrogen electrode (SHE)] and its low specific weight (0.53 gcm^{-3}) [13, 14, 24, 25]. The anode could be used, for example, in all-solid-state batteries (ASSBs), which have the potential to significantly exceed the safety performance, energy density, lifetime, and operating temperature range of today's LIBs. Being the core component of forthcoming technologies such as the Li-S or Li-air batteries, the Li-metal anode even offers the prospect of energy storage systems with a theoretical energy density of 550 Wh kg^{-1} with a sulfur cathode [69–72] and as much as 12 kWh kg^{-1} with an air cathode [73–77]. The success of these potentially revolutionary energy storage systems is therefore strongly intertwined with the development of stable Li-metal anodes. In particular, the growth of dendrites, the high reactivity of lithium, and associated problems are, however, slowing down the

advancement and commercialization of the aforementioned battery technologies and turning the processing and handling of Li metal anodes into a formidable challenge. During charging and discharging, uncontrolled deposition can lead to the growth of needle-like lithium dendrites [150], which results in poor cycle efficiency and poses a high risk for a short circuit.

The dendrite formation within a battery, however, can hardly be considered independently of the solid electrolyte interphase (SEI) covering the surface of the lithium anode. The SEI is a passivation layer that forms at the interface of the anode and the electrolyte as the electrolyte is oxidized by lithium. Although the SEI protects against further degradation, cracks in the SEI can lead to further electrolyte decomposition, which is associated with a loss of active material and a reduction in Coulomb efficiency. In addition to the reaction with the electrolyte, the performance of the electrode is also affected by the penetration of atmospheric impurities into the battery cell, via small amounts in the electrolyte or on the metal itself, which can lead to unforeseen corrosion of the anode. For example, the lithium surface may already be contaminated with diverse impurities from the atmosphere as a consequence of different processing conditions.

Due to the high reactivity of metallic lithium, adsorption processes and reactions with impurities are difficult to access experimentally on an atomic level. To gain atomistic insights, basic processes of lithium degradation can be made accessible through the simulation of basic model systems using density functional theory. For example, Koch *et. al* and Etxebarria *et. al* have investigated the initial effects of gas-treatment strategies [83] or contaminants of pristine lithium metal through atmospheric gases [84] with DFT. Accordingly, in our previous DFT study on the fundamental mechanisms of lithium oxidation [68], we showed that the absorption of oxygen on low-index Li surfaces occurs under the formation of coordinated cluster structures, which we identified as lithium suboxides. In this study, a thermodynamic evaluation via a phase diagram revealed that the absorption structures are energetically more stable than the pristine lithium surfaces even up to extremely low pressures. At the same time, the absorption complexes must be regarded as metastable structures, since lithium bulk oxide (bulk-Li_2O) has proven to be the thermodynamically more stable structure over the entire pressure range. While DFT calculations can show that a transformation of the absorption structures to bulk-Li_2O must occur from a thermodynamic point of view, the transformation process itself remains difficult to capture using conventional quantum mechanical methods,

as these are computationally expensive and therefore only limited to short simulation times and small systems of a few hundred atoms.

In this context, the bond-order-based reactive force field (ReaxFF) has emerged as a promising method as it overcomes these limitations and enables reactive simulation at an atomic level for large-scale systems (up to 100.000 atoms) over an extended period of time ($\sim$ns). ReaxFF has already been successfully applied to a variety of different battery materials and has been used to study electrodes and electrolytes for lithium and post-lithium systems. Consequently, several parameter sets are available for the description of the Li-Li and Li-O interactions, which have been trained for application in either electrolyte or bulk systems. With the goal of improving the description of fractures in Li_2O, O'Hearn *et al.* optimized Li-O parameters [151] using the atom-condensed Kohn-Sham density functional theory (DFT) approximated to a second order (ACKS2) charge model [152, 153]. However, the training sets for the mentioned Li-Li and Li-O parameters have not yet included neither self-diffusion processes on the low-index surfaces of metallic lithium, nor data reflecting the transition from metallic lithium to Li_2O. Therefore, to simulate thermodynamically and kinetically induced surface growth phenomena on metallic Li- and Na electrodes, we have recently optimized Li-Li and Na-Na parameters using the *KVIK* optimization routine [154].

In the present study, we provide a reactive force field to describe the process of Li anode degradation induced through oxygen impurities at a molecular scale. Building on our DFT results and the optimized Li-Li parameters for the surface growth phenomena [68, 89, 117, 154], we reoptimized a reactive ReaxFF-Li/O force field that correctly predicted the transformation to bulk-$\mathrm{Li_2O}$. The comprehensive training set comprised a plethora of bulk, surface, and absorption energies calculated at the DFT level. Using the oxidation of Li nanoparticles via a Grand Canonical Monte Carlo simulation (GCMC) and subsequent simulated thermal annealing via molecular dynamics (MD), we present the complete oxidation process from metallic lithium via the formation of suboxides, to amorphous lithium oxide, to a crystalline Li_2O nanoparticle.

6.3 Computational details

6.3.1 ReaxFF parameterisation and calculations

All reactive force field calculations in this work were performed using ReaxFF as implemented in the Amsterdam Modeling Suite 2021 [155]. To efficiently model atomic charges and linear response properties, charges were distributed according to the atom-condensed Kohn-Sham density functional theory approximated to second order (ACKS2) scheme [152, 153]. The O-O parameters are based on the force field in Ref. [156, 157] were adapted for the use with ACKS2. The Li-Li parameters were optimized using the KVIK training approach, which along with the method was presented in our previous work [154]. The KVIK optimization routine was developed for efficient training of ReaxFF force fields and was also applied to optimize the Li-O parameters presented in this work. The training set for the optimization of Li-O parameters consists entirely of DFT calculations and includes bulk, surface, and adsorption/absorption structures. The optimized ReaxFF parameter set for the description of Li-O interactions is provided in the Appendix.

6.3.2 DFT calculations

DFT calculations were performed using the periodic Vienna *ab initio* simulation package (VASP). For the core electrons projector augmented wave (PAW) potentials with valence states of 2*s* for lithium and 2*s*2*p* for oxygen [86–88] were used with an energy cutoff of 400 eV. The Bayesian error estimation functional with van der Waals correlation (BEEF-vdW) [60] was used as exchange-correlation functional [60], since it provided excellent agreement with experimental data for metallic Li systems and showed a significantly improved value for the binding energy of an oxygen molecule compared to the very popular and widely used PBE functional [90]. For periodic systems, a Gaussian smearing of 0.2 eV was used, while the molecular O_2 reference was calculated with a smaller smearing of 0.01 eV. Based on a convergence study, supercells with eleven layers for Li(100) and Li(110) and seventeen layers for Li(111) were chosen for the metallic lithium surfaces. To simulate bulk behaviour, the coordinates of the two lowest layers were constrained to the bulk structure of *bcc*-lithium (a=3.40 Å), while the coordinates of the remaining surface layers and oxygen adsorbates were fully optimized

until the force convergence criterion of 0.005 eV/Å was met. A detailed description of the absorption complexes used to optimize and validate the ReaxFF parameters can be found in our study on the initial oxidation of metallic lithium anodes [68].

6.3.3 ReaxFF GCMC

To model the oxidation of lithium nanoparticles, we combine ReaxFF with the Grand Canonical Monte Carlo (GCMC) approach within a μVT ensemble as implemented in the AMS-ReaxFF implementation of the Amsterdam Modeling Suite 2021 [155, 158]. The GCMC method allows the generation and investigation of thermodynamic equilibrium structures at a defined oxygen chemical potential $\mu_{\mathrm{O}}(T, P)$ based on a stochastic approach. In a GCMC simulation, several trial moves are performed in which a particle (in this case an oxygen atom) is either inserted, removed or displaced. After a Monte Carlo (MC) move, the random geometry is optimized with the ReaxFF potential. Based on the optimized energy of the geometry, the Boltzmann probabilities P to either accept or reject the respective step are determined through

$$P_{\mathrm{insert}}^{\mathrm{accept}} = \min\left[1, \frac{V_{\mathrm{acc}}}{\Lambda^3(N+1)} \exp\left(-\frac{E_{\mathrm{new}} - E_{\mathrm{old}} - \mu_{\mathrm{O}}(T,P)}{k_{\mathrm{B}}\mathrm{T}}\right)\right], \tag{6.1}$$

$$P_{\mathrm{remove}}^{\mathrm{accept}} = \min\left[1, \frac{N\Lambda^3}{V_{\mathrm{acc}}} \exp\left(-\frac{E_{\mathrm{new}} - E_{\mathrm{old}} - \mu_{\mathrm{O}}(T,P)}{k_{\mathrm{B}}\mathrm{T}}\right)\right], \tag{6.2}$$

$$P_{\mathrm{displace}}^{\mathrm{accept}} = \min\left[1, \exp\left(-\frac{E_{\mathrm{new}} - E_{\mathrm{old}}}{k_{\mathrm{B}}\mathrm{T}}\right)\right]. \tag{6.3}$$

Here Λ denotes the thermal de Broglie wavelength of the exchanged particle, N the number of exchangeable particles of the system (before the MC move) and $E_{\mathrm{new}} - E_{\mathrm{old}}$ the difference of the total energy of the old structure before and the new structure after the MC move. V_{acc} denotes the accessible volume, which is determined by the atomic radius r of the respective species and the difference between the fixed total volume V of the system and the occupied volume V_{occ} through

$$V_{\mathrm{acc}} = V - V_{\mathrm{occ}} = V - N\frac{4}{3}\pi r^3. \tag{6.4}$$

The oxidation of the nanoparticles was studied under ambient conditions at T= 300 K and an oxygen partial pressure of $p_{\mathrm{O}} = 0.21$ atm. Using the equation

$$\begin{aligned}\mu_{\mathrm{O}}(T,p) &= \frac{1}{2}\,\mu_{\mathrm{O_2}}\,(T,p) \\ &= \frac{1}{2}\left[\mu_{\mathrm{O_2,exp}}(T,p^0) + k_{\mathrm{B}}\mathrm{T}\,\ln\left(\frac{p}{p^0}\right) - E_{\mathrm{O_2}}^{\mathrm{diss}}\right]\end{aligned} \tag{6.5}$$

the chemical potential of a single O atom was set to $\mu_{\mathrm{O}} = 3.13$ eV. In this context, $\mu_{\mathrm{O_2,exp}}$ denotes the experimental chemical oxygen potential at T and p^0 as reported in standard thermodynamic tables [118]. $E_{\mathrm{O_2}}^{\mathrm{diss}}$ is the bond dissociation energy of $\mathrm{O_2}$ at 0 K and was calculated with ReaxFF $\left(E_{\mathrm{O_2}}^{\mathrm{diss}} = 5.59\ \mathrm{eV}\right)$. To investigate the influence of different crystal facets and edges on the oxidation of lithium nanoparticles within the framework of a coupled ReaxFF/GCMC approach, different shapes of nanoparticles of approximately 1000 atoms were used as an initial structure for the GCMC simulations. The equilibrium shape of the nanoparticles was generated via a potential-dependent Wulff construction as described in our previous work [154].

6.3.4 Settings for molecular dynamics

For the recrystallization of the lithium nanoparticles reactive Molecular dynamics (MD) simulations were performed with the AMS-ReaxFF implementation of the Amsterdam Modeling Suite 2021. For the numerical integration of the equations of motion, the Velocity-Verlet algorithm with a time step of 0.25 fs was used. The simulations were performed within an NVT ensemble coupled to a Nosé-Hoover (NHC) thermostat with a damping constant τ of 100 fs.

6.4 Results and discussion

6.4.1 Optimization and validation of Li-O parameters

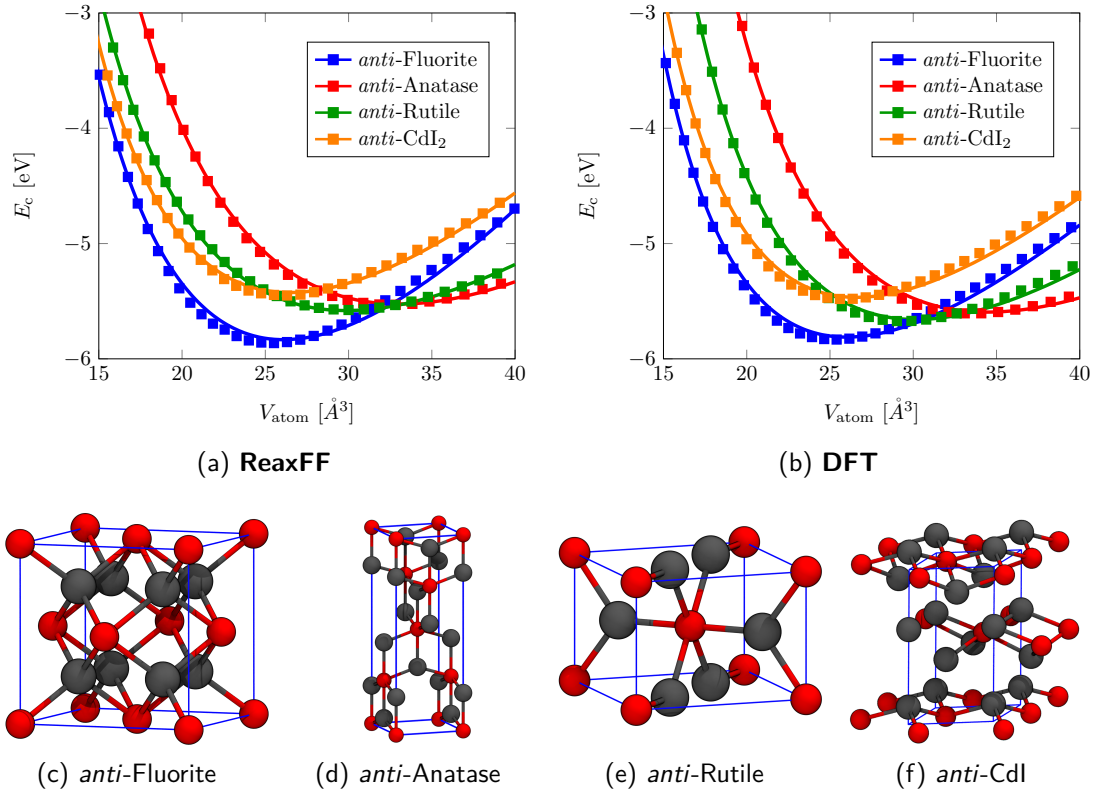

(a) **ReaxFF** (b) **DFT**

(c) *anti*-Fluorite (d) *anti*-Anatase (e) *anti*-Rutile (f) *anti*-CdI

Figure 6.1. Equations of state for different bulk phases calculated with ReaxFF in **(a)** and DFT in **(b)** and the respective ReaxFF optimized crystal structures in **(c)**-**(d)**. Lithium atoms are represented as grey and oxygen atoms as red spheres.

In the following, the data calculated with ReaxFF for different bulk and surface systems are compared with the DFT target values to validate the trained Li-O interactions. The training set for the empirical force field parameters was based on the DFT presented in this section and the optimization was performed within the KVIK framework. A detailed description of the *KVIK* optimiser and validation of the Li-Li metal interactions, can be found in our previous work [154].

Table 6.1 Comparison of lattice constants a_0 and c_0 in Å, formation energies E_F in eV and bulk modulus B_0 in GPa for $\mathrm{Li_2O}$ bulk phases, obtained from ReaxFF and DFT. The formation energies were calculated using equation 6.6 and the experimental values for the *anti*-fluorite phase are taken from [159].

System	Space group	Property	ReaxFF	DFT	Expt.
anti-Fluorite	$\mathrm{Fm\bar{3}m}$	a_0	4.67	4.66	4.62
		E_F	-5.86	-5.83	-6.21
		B_0	79	74	75
anti-Anatase	$\mathrm{I4_1/amd}$	a_0	3.66	3.61	
		c_0	9.76	10.11	
		E_F	-5.52	-5.59	
		B_0	53	55	
anti-Rutile	$\mathrm{P4_2/mnm}$	a_0	4.41	4.33	
		c_0	3.08	3.10	
		E_F	-5.58	-5.66	
		B_0	52	64	
anti-$\mathrm{CdI_2}$	$\mathrm{P6_3mc}$	a_0	3.19	3.19	
		c_0	5.95	5.79	
		E_F	-5.45	-5.47	
		B_0	66	71	

For training and evaluation of the bulk properties, various crystal systems with an $\mathrm{A_2B}$ formula were used. The systems shown are all *anti*-structures since the positions of the anion and cation are reversed compared to the name-giving salt. At ambient conditions, $\mathrm{Li_2O}$ crystallizes in the cubic $\mathrm{Fm\bar{3}m}$ space group and adopts an *anti*-fluorite structure. This configuration is characterized by the arrangement of $\mathrm{O^{2-}}$ ions in a face-centred cubic (*fcc*) sublattice with $\mathrm{Li^+}$ ions in tetrahedral interstitial sites as shown in Fig. 6.1c. Experimental data are only available for $\mathrm{Li_2O}$ in the *anti*-fluorite phase, while the other phases are model systems selected to give a broad overview of the configuration space through varying bond distances, geometries, and coordination environments. Accordingly, the *anti*-fluorite phase was given the strongest weighting in the training of the potential. The optimization was based on structural, energetic, and uniform volumetric compression and expansion properties of the bulk phases. Formation energies for bulk phases were calculated using the following equation:

$$E_\mathrm{F} = \frac{1}{N}\left[E^\mathrm{bulk}_\mathrm{Li_2O} - 2N \cdot E^\mathrm{bulk}_\mathrm{Li,bcc} - \frac{N}{2} \cdot \left(E^\mathrm{gas}_\mathrm{O_2} + E^\mathrm{ZPE}_\mathrm{O_2}\right)\right] \tag{6.6}$$

In this equation, $E^{\mathrm{bulk}}_{\mathrm{Li_2O}}$ refers to the energy of one of the $\mathrm{Li_2O}$ bulk systems, $E^{\mathrm{bulk}}_{\mathrm{Li,bcc}}$ to the energy of a single Li atom in the body-centred cubic (*bcc*) bulk structure (which is lithium's most stable phase under standard conditions) $E^{\mathrm{gas}}_{\mathrm{O_2}}$ to the total energy of an $\mathrm{O_2}$ gas-phase molecule, and $E^{\mathrm{ZPE}}_{\mathrm{O_2}}$ to the zero-point energy correction as calculated within the harmonic approximation. N is the number of $\mathrm{Li_2O}$ units within the $\mathrm{Li_2O}$ crystal phase. An overview of bulk properties calculated with ReaxFF and DFT can be found in Table 6.1. The respective lattice constants (a_0, c_0) and formation energies (E_{F}) were obtained from the corresponding cell and geometry optimized structure. As can be seen in Fig. 6.1, our parameterized potential function shows excellent agreement with the DFT target data. The ReaxFF potential is not only able to correctly reproduce the same energetic order of the bulk phases but also shows, like the DFT data, a transition from *anti*-Fluorite to *anti*-Rutile (32 $\mathrm{Å}^3$ to 33 $\mathrm{Å}^3$) and a transition to *anti*-Anatase ($>$ 33 $\mathrm{Å}^3$). A comparison of the calculated properties of the bulk phases in Tab. 6.1 shows, that the values for the *anti*-fluorite phase agree almost exactly with the DFT values. The lattice constant and bulk modulus also match the experimental values almost perfectly, whereas the theoretical formation energy is much lower than the experimental value. The mismatch is due to the DFT dataset, where the formation energy is also underestimated, as too low formation energies for oxides due to overbinding of the O_2 molecule are a notorious problem of DFT. The binding energies of the remaining bulk phases also show nearly exact agreement with the DFT values and thus reflect the corresponding relative stabilities. Deviations can be found for the lattice constants. Here the maximum deviation was found for the *anti*-Anatase phase, where the deviation of the c_0 value is 0.35 Å. However, this deviation is less than 4% of the DFT value. The deviations of the values from the bulk modulus are also within a reasonable range and are at most 7% with respect to the DFT value.

Surface energies were included in the training via different stoichiometric terminations of the most stable *anti*-Fluorite phase. The surface energies $\gamma_{\mathrm{Li_2O}}$ were determined by equation 6.7:

$$\gamma_{\mathrm{Li_2O}} = \frac{1}{2A}\left(E^{\mathrm{slab}}_{\mathrm{Li_2O}} - N \cdot E^{\mathrm{bulk}}_{\mathrm{Li_2O}}\right) \tag{6.7}$$

Here, A is the surface area of the slab, $E^{\mathrm{slab}}_{\mathrm{Li_2O}}$ the energy of the slab, N the number of $\mathrm{Li_2O}$ fragments in the slab and $E^{\mathrm{bulk}}_{\mathrm{Li_2O}}$ the bulk energy per $\mathrm{Li_2O}$ unit formula. For the $E^{\mathrm{bulk}}_{\mathrm{Li_2O}}$ reference the energy of the *anti*-fluorite phase was selected. Given that the $\mathrm{Li_2O}$

Table 6.2 Calculated surface energies (γ) for low-index Li_2O-surfaces in meV.

Surface	surface name	ReaxFF	BEEF-vdW	PBE[119]	PBE-D3 + U[160]
Li_2O-(100)	stoichi-1	147	97	-	
	stoichi-2	118	75	75	102
Li_2O-(110)	stoichi	113	58	56	77
Li_2O-(111)	stoichi	88	32	30	54

surfaces in this work were solely symmetric surface labs, the area A was multiplied by two. In Tab. 6.2 ReaxFF values are compared with own DFT values and those from other works[119, 160]. The nomenclature of the surfaces follows that of [119].

As can be seen, the absolute surface energies are significantly higher than the corresponding values of our DFT calculations. However, it can also be seen that the absolute values show significant differences depending on which exchange-correlation functional was used. All methods, nonetheless, reflect the same relative stability of the surfaces. As with all DFT calculations, the optimized interatomic potential identifies the Li_2O-(111) as the most stable surface and reproduces the stability order of the different terminations.

To reflect the interaction with metallic lithium via ReaxFF, geometries and binding energies of monoatomic O on different high-symmetry adsorption sites of the low-indexed metallic lithium surfaces Li(100), Li(110), and Li(111) were included in the training. For the adsorption/absorption structures, the binding energies were referenced to the gas-phase energy of O_2 and calculated via

$$E_{\mathrm{bind}} = \frac{1}{N_{\mathrm{ads}}} \left[E_{\mathrm{ad}}^{\mathrm{tot}} - E_{\mathrm{slab}}^{\mathrm{clean}} - \frac{N_{\mathrm{ads}}}{2} \left(E_{\mathrm{O_2}}^{\mathrm{gas}} + E_{\mathrm{O_2}}^{\mathrm{ZPE}} \right) \right]. \tag{6.8}$$

$E_{\mathrm{ad}}^{\mathrm{tot}}$ is the total energy of geometry-optimized Li surface with the absorbed oxygen, $E_{\mathrm{slab}}^{\mathrm{clean}}$ the total energy of the surface slab and N_{ads} the number of absorbed oxygen atoms. As we have shown in our previous work on the initial oxidation of lithium surfaces, the strongly exothermic absorption of oxygen occurs under considerable rearrangement of the metallic lithium surface. In this process, oxygen forms symmetrical suboxide cluster structures on the lithium surface. While the formation of bonds between lithium and oxygen leads to a thermodynamic stabilization of the system due to their strong ionic character, the rearrangement of the lithium surface is associated with a

Table 6.3 Calculated ReaxFF and DFT binding energies in eV for the absorption of an oxygen atom on the high-symmetry adsorption sites of (6x6) (100), (4x6) (110) and (4x8) (111) lithium surfaces. The DFT values are taken from our previous work [68].

(*hkl*)	Adsorption side	ReaxFF	DFT
(100)	*hollow*	-5.35	-5.59
	bridge	-5.70	-5.48
	subsurface	-5.71	-5.35
	top	-4.29	-4.32
(110)	*long-bridge*	-5.55	-5.75
	short-bridge	-5.45	-5.28
	subsurface	-5.78	-5.43
	top	-4.75	-5.00
(111)	*hcp*	-5.23	-5.40
	fcc	-5.65	-5.22
	bridge	-5.52	-5.20
	subsurface	-5.76	-5.33
	top	-5.06	-5.14

destabilization of the system. The magnitude of the binding energy is determined by the sum of the stabilizing effects caused by the formation of the absorption complex and the destabilization caused by the related rearrangement. As a comparison of the binding energies calculated with ReaxFF and DFT in Tab. 6.3 shows, our force field generally overestimates the stability of the structures in which oxygen is located below the surface. Therefore, the most stable structure in all ReaxFF calculations is erroneously the respective *subsurface* absorption complex. Furthermore, it can be observed that absorption complexes with a similar cluster configuration exhibit a comparable high binding energy. For example, ReaxFF calculates almost the same binding energy for absorption into the *bridge* and *subsurface* positions on Li(100), since oxygen is present in both positions in an octahedral coordination environment, which was with six lithium atoms the highest coordination we observed. This undesirable description is caused by the fact that the optimized potential prefers absorption complexes with higher coordination due to the stabilization of bulk-$\mathrm{Li_2O}$, where a single oxygen is surrounded by eight lithium ions. Similar difficulties were encountered in optimizing the Mg-O interactions in our previous study [161]. While the binding energy in DFT is

composed of the aforementioned stabilizing and destabilizing effects of bond formation and reorganization of the surface, it is determined almost solely through bond formation in ReaxFF. Due to marginally different bond lengths and angles of the surface clusters, the addition of angle energy terms to the potential did not lead to an improvement of the stability order. We have therefore traded off the stability order of the binding energies in favour of improving the stability of bulk-$\mathrm{Li_2O}$ to allow a description of oxide formation. For the absorption structures, we have therefore focused on properly representing the coordination geometries of the surface clusters, reflecting the relative instability of the *top* positions, and ensuring an overall reasonable order of magnitude for the binding energies with respect to the DFT data. As can be seen in Tab. 6.3, the binding energies obtained with the optimized parameters are all lower than the formation energy of *anti*-fluorite (-5.86 eV).

6.4.2 Oxidation of lithium nanoparticles

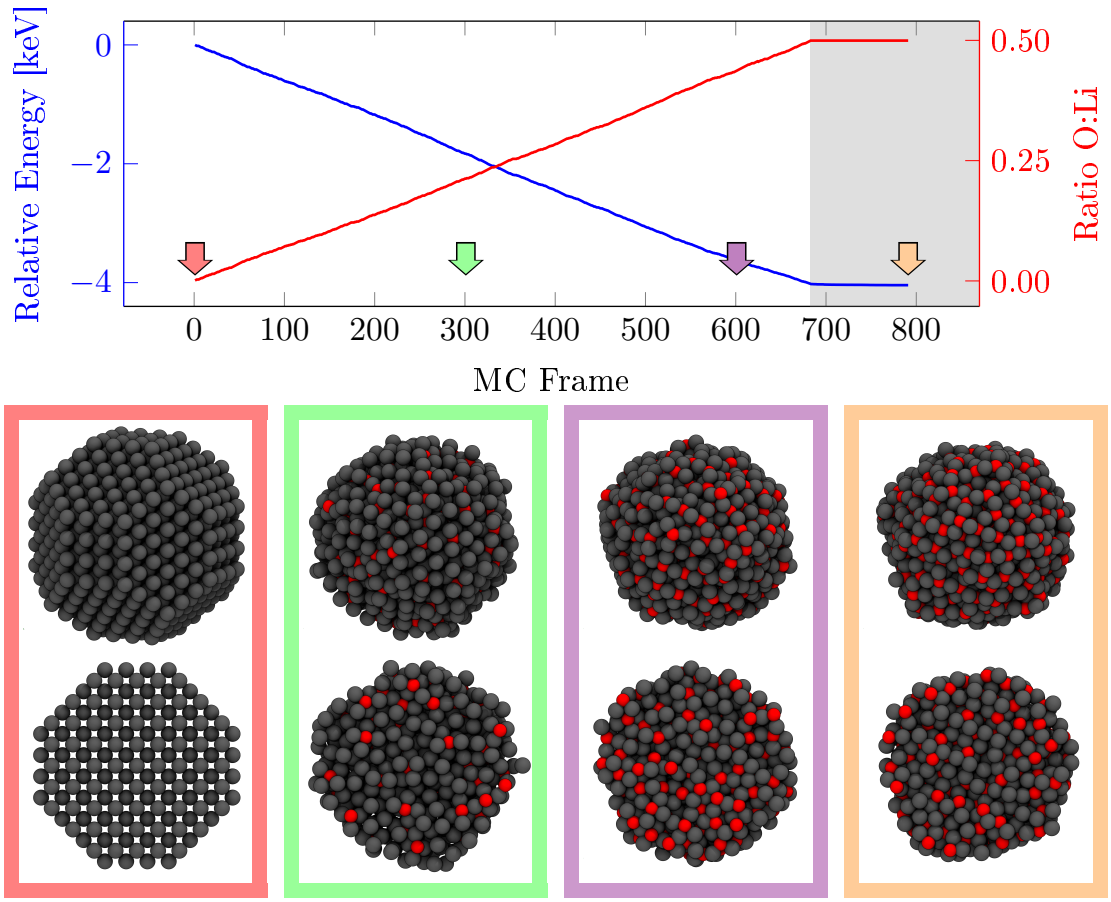

Figure 6.2. Overview of the different stages of GCMC simulated oxidation of the pristine lithium nanoparticle at 300 K and 0.21 atm. In the grey area, equilibration of the nanoparticle was performed at a fixed Li:O ratio of 2:1.

To investigate the influence of different crystal facets and edges on the oxidation process, we have investigated three differently shaped lithium nanoparticles using the thermodynamically driven coupled ReaxFF/GCMC approach. The equilibrium shape of the three nanoparticles (size 1000 atoms) was generated from a potential-dependent Wulff construction. Starting from pristine lithium nanoparticles, in the GCMC simulation oxygen atoms were successively introduced into the systems at a temperature of 300K and an oxygen partial pressure of 0.21 atm. The oxidation of Li is illustrated by the lithium nanoparticle under neutral conditions, which will be referred to

in the following. The results for the two other particles indicate an equivalent behaviour during oxidation. As can be seen in Fig. 6.2, the oxygen atoms are absorbed uniformly on the surface as well as inside the nanoparticle at the beginning of the reaction, forming suboxidic lithium compounds. With increasing oxygen content, an increasingly strong restructuring and amorphization of the nanoparticle can be observed. As DFT calculations have already shown, molecular O_2 is not stable in the presence of metallic lithium, since its dissociation and absorption on the surface takes place virtually without any barrier. Therefore, it is not surprising that during the initial oxidation process, no structure was observed on which an O_2 molecule was adsorbed on the nanoparticle. It was only with advanced oxidation after a Li:O ratio of approximately 2:1 was reached, that O_2 adsorbed on the nanoparticle's surface. As the GCMC simulation progressed, the surface consequently was covered with more and more O_2 molecules from this stage onwards. To optimize the structure, we allowed additional MC steps at a fixed Li:O ratio of 2:1, where the movement of O was allowed, but additional insertion or removal moves were prohibited. The MC moves were allowed until the relative energy converged to a constant value (as can be seen in the illustration) and the structure was at a (local) thermodynamic minimum. Despite this optimization, however, this structure still maintained an amorphous character.

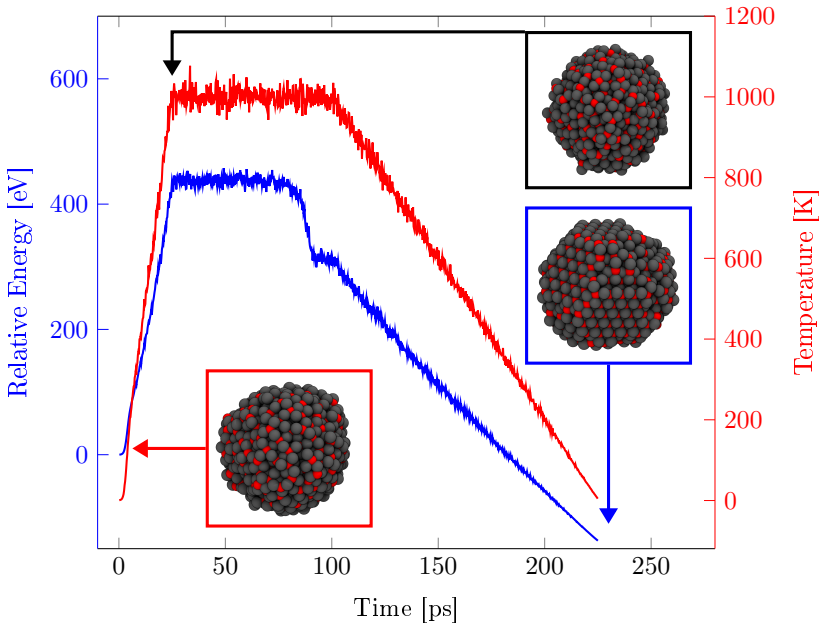

Figure 6.3. Recrystallization of an amorphous Li_2O nanoparticle into the *anti*-fluorite phase through simulated thermal annealing at 1000 K in an NVT ensemble.

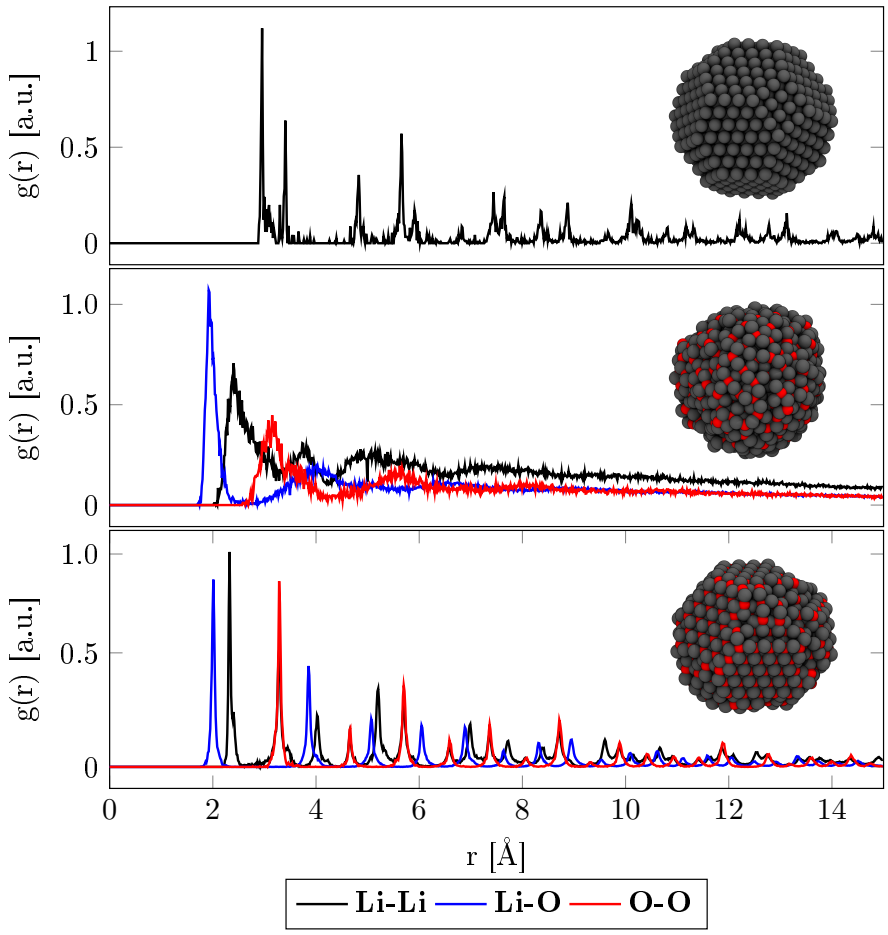

Figure 6.4. Radial distribution functions (RDFs) for pure lithium, an amorphous (before annealing), and a crystalline (after annealing) Li_2O nanoparticle.

For the recrystallization of the nanoparticle, we performed simulated thermal annealing via MD simulation. As shown in Fig 6.3, the particle was heated at a rate of 40 Kps^{-1} to 1000 K, where the temperature was held constant for 75 ps. The system was then slowly cooled to 1K at a rate of 8 Kps^{-1} . The recrystallization in Fig. 6.3 can be recognized by the sudden decrease of the relative energy (at constant temperature) since the potential energy of the nanoparticle decreases due to the gain in stability caused by the recrystallization.

For the different stages of oxidation, a radial distribution function (RDF) was used to investigate the distribution and bonds of the atomic species within the nanoparticles. In Fig. 6.4, the amorphous character of the particle before annealing can be seen, while the discrete peaks reveal the crystalline nature of the particle after annealing.

In the RDF of the recrystallized particles, the maxima of the peaks indicate the same interatomic distances as in the bulk structure of the Li_2O *anti*-Fluorite (Li-Li: 2.33 Å , O-O: 3.28 Å , Li-O: 2.01 Å). Most of the surfaces of the *anti*-fluorite particle correspond to the stable "stoichi" variant of the Li_2O-(111) termination.

Using Debye's formula [162], the powder XRD spectrum was determined via the interatomic distances for the pristine and oxidized lithium nanoparticles before and after annealing. To calculate the spectrum, the wavelength of a Cu-K-α radiation (1.54 Å) and the numerical Hartree-Fock X-ray scattering factors for the elements lithium and oxygen from [163] were used. As can be seen in Fig. 6.5 the pattern indicates the amorphous nature of the particle before annealing, as due to a missing long-range order only a single broad peak is visible in this case. After annealing, several well-defined diffraction peaks are observed. These peaks have been assigned the Miller index of the corresponding atomic plane in accordance with the experimental powder XRD spectra in Ref. [164]. The position of the peaks is in good agreement with the experimental measurement.

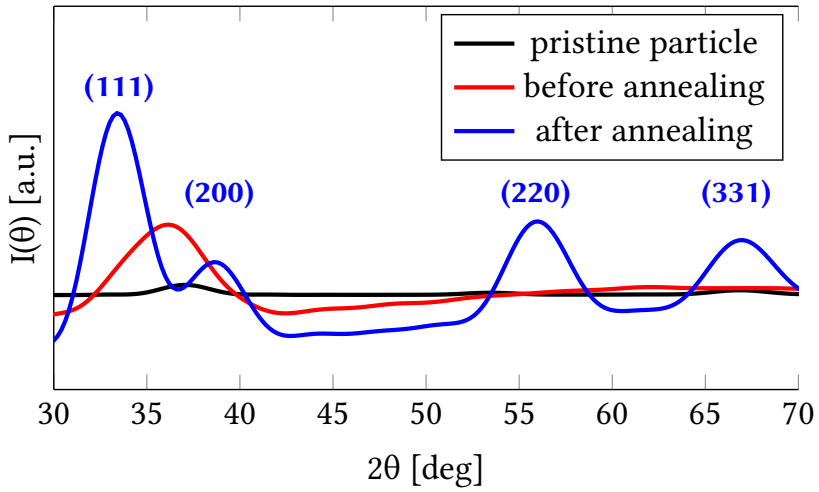

Figure 6.5. Simulated powder XRD pattern of a pure lithium particle (black), and an oxidized particle before (red) and after annealing (blue). The intensities I(θ) are given in arbitrary units and 2θ refers to the incidence angle of the Cu-K-α radiation. The annealed Li_2O particle diffraction peaks were assigned the Miller index of the corresponding atomic plane in analogy to Ref. [164]

6.5 Conclusion

In this work, the Li-O interaction was reoptimized for a ReaxFF force field to describe the oxygen-induced degradation of metallic lithium anodes. Based on our force field for describing the metallic properties of lithium, the parameters for the lithium-oxygen interactions were trained on various bulk and surface properties using the KVIK optimizer. The interatomic potential can reliably reproduce these properties and exhibits a significantly improved stability ratio of bulk to binding energies than previous force fields. Using GCMC simulations on metallic Li nanoparticles, we were able to model the oxidation process of metallic lithium to crystalline Li_2O. Initially, oxidation took place via the formation of suboxidic cluster structures known from our previous DFT studies. With increasing oxygen concentration, the formation of an amorphous structure was observed until a Li:O ratio of 2:1 was reached and molecular O_2 adsorbed on the oxidized particle surface. In agreement with the predictions from the DFT phase diagram, the amorphous Li_2O particle could be transferred to its thermodynamic minimum, the crystalline *anti*-fluorite phase structure, using MD simulated thermal annealing. Most of the particle surface of the cluster here consists of the "stoichi" variant of the Li_2O-(111) surface, which is also the most stable termination in DFT calculations presented in this and other studies. Furthermore, the powder XRD spectrum modelled via Debye's formula shows excellent agreement between theory and experiment. By optimizing the solid-state properties, the presented force field can simulate the oxidation and passivation of the lithium anode and provide a good basis for the SEI simulation through the extension of further parameters. In combination with the optimized Li/Li interactions from our prior work, the reactive force field can now be used to study inhomogeneous metal deposition (i.e., dendrite growth) through a passivating oxide layer, thanks to the addition of the optimized Li-O parameters.

7

Further work

The following chapter summarizes further research projects, where a detailed presentation of the results is provided in the respective publications.

Style, numbering and citations have been adapted to ensure a consistent presentation throughout the work.

7.1 Microscopic Properties of Na and Li-A First Principle Study of Metal Battery Anode Materials

Daniel Gaissmaier[1, 2, 3], Matthias van den Borg[1], Donato Fantauzzi [2, 3, 4] and Timo Jacob[1, 2, 3], *ChemSusChem* **2020**, *13*, 771-783.

Reproduced from Ref. [89] under the CC BY-NC-ND 4.0 licence [141] and with the authors' permission.

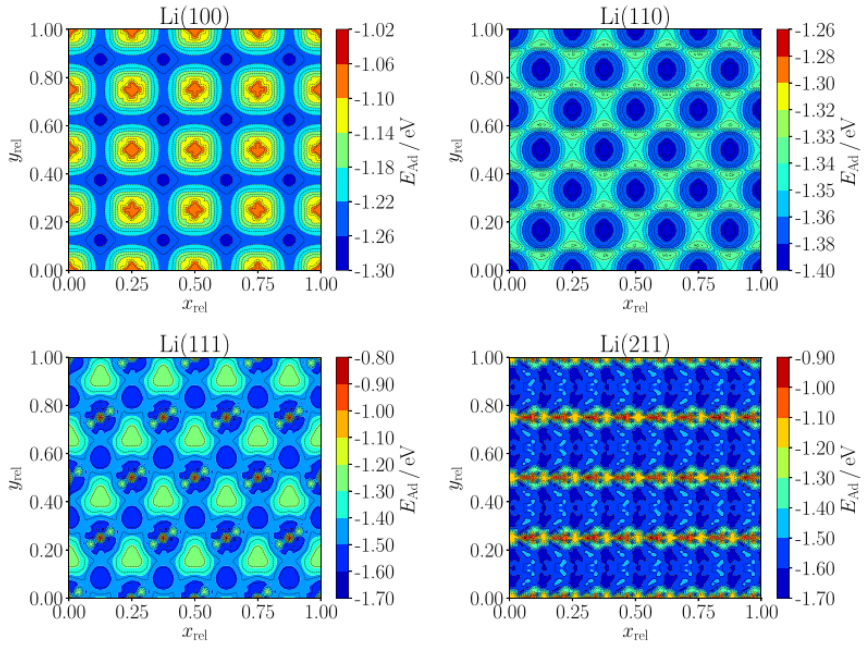

Figure 7.1. Calculated PES (DFT-PBE) for the (4 x 4) Li(100), (4 x 6) Li(110), (4 x 4) Li(111), and (4 x 8) Li(211) surface unit cells. The relative coordinates are given in relation to the supercell

Due to the theoretical high specific capacity (3860 mAh/g) and the low standard electrode potential (-3.040 V vs. standard hydrogen electrode), rechargeable lithium

[1] Institute of Electrochemistry, Ulm University, Albert-Einstein-Allee 47, D-89081 Ulm, Germany
[2] Helmholtz-Institute Ulm (HIU) for Electrochemical Energy Storage, Helmholtzstr. 11, 89081 Ulm, Germany
[3] Karlsruhe Institute of Technology (KIT), P.O. Box 3640, 76021 Karlsruhe, Germany

metal batteries are considered as excellent energy storage systems. Unfortunately, security concerns related to dendrite formation during charge/discharge cycles still hinder the commercial use of Li metal-based batteries. Using density functional theory, we have studied the bulk and surface properties of metallic lithium at an atomistic level. In this process, bcc Li(100) proved to be the most stable metallic lithium surface. Subsequently, possible self-diffusion mechanisms on perfect and imperfect Li(100) surfaces were examined. For this purpose, nudged elastic band calculations were performed to characterize the respective diffusion processes and to determine the relevant pre-exponential factors and activation barriers. On the basis of the acquired data, it became possible to derive activation temperatures and reaction rates for the respective processes, which are useful for experimental verification as well as for the implementation in long-scale kinetic Monte Carlo simulations.

7.2 First-Principles Studies on the Atomistic Properties of Metallic Magnesium as Anode Material in Magnesium-Ion Batteries

Florian Fiesinger [1] Daniel Gaissmaier[1, 2, 3], Matthias van den Borg[1] and Timo Jacob[1, 2, 3],
ChemSusChem **2022**, *15*, e202200414.

Reproduced from Ref. [165] under the CC BY-NC-ND 4.0 licence [141] and with the authors' permission.

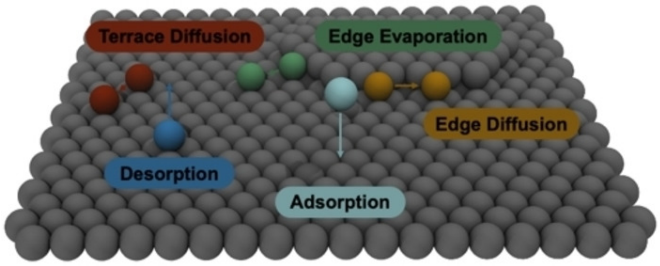

Figure 7.2. Schematic representation of a Mg(0001) surface and different possible self-diffusion processes.

Rechargeable magnesium-ion batteries (MIBs) are a promising alternative to commercial lithium-ion batteries (LIBs). They are safer to handle, environmentally more friendly, and provide a five-time higher volumetric capacity (3832 mA h cm^{-3}) than commercialized LIBs. However, the formation of a passivation layer on metallic Mg electrodes is still a major challenge towards their commercialization. Using density functional theory, the atomistic properties of metallic magnesium, such as bulk, surface, and adsorption properties, were examined. Well-selected self-diffusion processes on perfect and imperfect Mg surfaces were investigated to better understand the initial surface growth phenomena. Subsequently, rate constants and activation temperatures of crucial diffusion processes on Mg(0001) and Mg(1011)were determined, providing preliminary insights into the surface kinetics of metallic Mg electrodes.

[1] Institute of Electrochemistry, Ulm University, Albert-Einstein-Allee 47, D-89081 Ulm, Germany
[2] Helmholtz-Institute Ulm (HIU) for Electrochemical Energy Storage, Helmholtzstr. 11, 89081 Ulm, Germany
[3] Karlsruhe Institute of Technology (KIT), P.O. Box 3640, 76021 Karlsruhe, Germany

7.3 KVIK Optimiser - An Enhanced ReaxFF Force Field Training Approach

Daniel Gaissmaier [1,2,3], Matthias van den Borg [1], Donato Fantauzzi [2,3,4] and Timo Jacob[1,2,3], ChemRxiv **2022**, DOI 10.26434/chemrxiv-2022-lrsjd.

Reproduced from Ref. [154] under the CC BY-NC-ND 4.0 licence [141] and with the authors' permission.

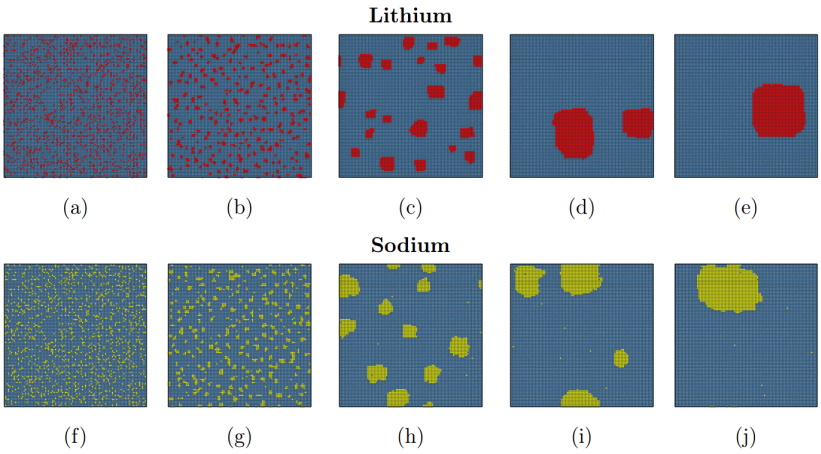

Figure 7.3. Snapshots of the initial nucleation and aggregation processes on 100x100 Li(100) (red, (a)-(e)) and 100x100 Na(100) (yellow, (f)-(j)) at 200 K and a surface coverage of 0.125 ML. The initial configuration was generated by a random distribution of adatoms on the respective surface. Hopping and exchange processes were considered for both systems, and the number of adatoms was kept fixed during the simulation.

In this work, we demonstrate the superior exploration capabilities of the population based methods over the sequential one-parameter parabolic interpolation (SOPPI) approach to optimise ReaxFF force field parameters. Evolutionary algorithms (EAs) are heuristic-based approaches using a population of concurrent models in the search space

[1] Institute of Electrochemistry, Ulm University, Albert-Einstein-Allee 47, D-89081 Ulm, Germany
[2] Helmholtz-Institute Ulm (HIU) for Electrochemical Energy Storage, Helmholtzstr. 11, 89081 Ulm, Germany
[3] Karlsruhe Institute of Technology (KIT), P.O. Box 3640, 76021 Karlsruhe, Germany
[4] Faculty of Physical Sciences, University of Iceland VR-III, 107 Reykjavík, Iceland

to evolve towards the global best through stochastic operations. The parallelisation of EAs scales almost linearly, and no differentiable objective function is required. These methods were tested for their search performance and convergence behaviour on different multi-dimensional, multimodal benchmark functions. The developed KVIK (Icelandic for: dynamic, in motion) optimisation framework features an extended training routine designed to parameterise solid-state systems efficiently. The optimisation routine was applied to train a reactive force field potential for metallic lithium and sodium and their interaction parameters. The KVIK-optimised ReaxFF potential function parameter set reproduces relative energy results from the Density Functional Theory (DFT) reference data set within the standard deviation range established using the error estimation routine provided by the BEEF-vdW density functional. Finally, thermodynamically and kinetically driven surface growth phenomena on metallic Li- and Na-electrodes were investigated using coupled ReaxFF/Monte Carlo (MC) approaches.

7.4 Development of a Mg/O ReaxFF Potential to describe the Passivation Processes in Magnesium-Ion Batteries

Florian Fiesinger [1] Daniel Gaissmaier[1, 2, 3], Matthias van den Borg[1], Julian Beßner[1], Adri C. T. van Duin [4] and Timo Jacob[1, 2, 3], *ChemSusChem* **2023**, *16*, e202201821.

Reproduced from Ref. [161] under the CC BY-NC-ND 4.0 licence [141] and with the authors' permission.

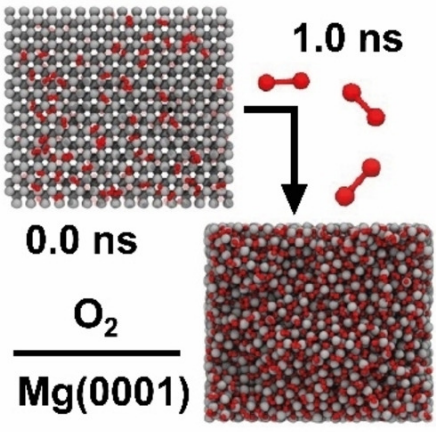

Figure 7.4. Schematic representation of the oxidation process of a Mg(0001) surface.

One of the key challenges preventing the breakthrough of magnesium-ion batteries (MIB) is the formation of a passivating boundary layer at the Mg anode. To describe the initial steps of Mg anode degradation by O_2 impurities, we have developed a Mg/O ReaxFF reactive force field description capable of accurately modelling the bulk, surface, adsorption, and diffusion properties of both metallic Mg and the salt MgO. We show that O_2 immediately dissociates upon first contact with the Mg anode

[1] Institute of Electrochemistry, Ulm University, Albert-Einstein-Allee 47, D-89081 Ulm, Germany
[2] Helmholtz-Institute Ulm (HIU) for Electrochemical Energy Storage, Helmholtzstr. 11, 89081 Ulm, Germany
[3] Karlsruhe Institute of Technology (KIT), P.O. Box 3640, 76021 Karlsruhe, Germany
[4] Department of Mechanical and Nuclear Engineering, Pennsylvania State University, University Park, PA 16801, USA

(modelled as Mg(0001), Mg(1010), and Mg(1011)), heating the surface to several 1000 K. The high temperature assists the further oxidation and forms a rocksalt interphase intersected by several grain boundaries. Among the Mg surface terminations, Mg(1010) is the most reactive, forming a MgO layer with a thickness of up to 25 Å. We also demonstrate the recrystallization of an amorphous MgO particle, which is obtained by performing grand canonical Monte Carlo simulations, into the rocksalt structure by thermal annealing at elevated temperatures. Our force field can be used to model the ongoing reactions in Mg-air batteries and constitutes an important step towards modelling the solid-electrolyte interface formation at the Mg anode.

7.5 Cornforth–Evans transition states in stereocontrolled allylborations of epoxy aldehydes

Robert R. A. Freund [1], Matthias van den Borg[2], Daniel Gaissmaier[2, 3, 4], Robin Schlosser[1], Timo Jacob[2, 3, 4] and Hans-Dieter Arndt[1], Chem.Eur.J. **2020**, *26*, 8639-8650

Reproduced from Ref. [166] under the CC BY-NC-ND 4.0 licence [141] and with the authors' permission.

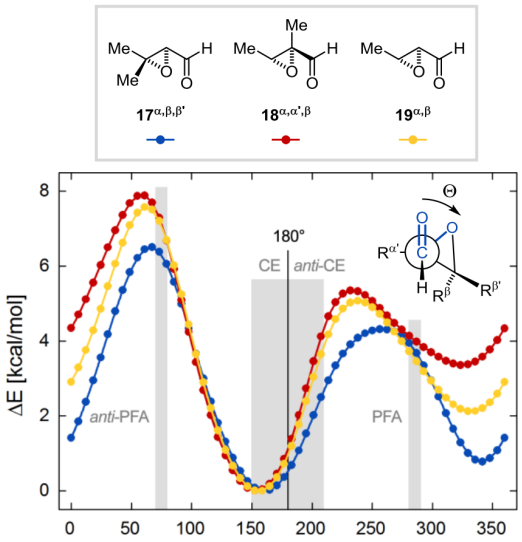

Figure 7.5. Computed rotational energy profile of simplified α,β-epoxy aldehydes. Level of theory: B3LYP-D3(BJ)/cc-pVDZ (vacuum). Grey areas show the possible range of conformations associated with the respective stereoinduction model for nucleophile addition to the carbonyl (PFA: 285$\pm$ 5°, anti-PFA: 75 $\pm$ 5°, CE: 165 $\pm$ 15°, anti-CE: 195 $\pm$ 15°).

[1] Institut für Organische Chemie und Makromolekulare Chemie Friedrich-Schiller-Universität Jena Humboldtstr. 10 07743 Jena Germany
[2] Institute of Electrochemistry, Ulm University, Albert-Einstein-Allee 47, D-89081 Ulm, Germany
[3] Helmholtz-Institute Ulm (HIU) for Electrochemical Energy Storage, Helmholtzstr. 11, 89081 Ulm, Germany
[4] Karlsruhe Institute of Technology (KIT), P.O. Box 3640, 76021 Karlsruhe, Germany

Allylboration reactions rank among the most reliable tools in organic synthesis. Herein, we report a general synthesis of trifunctionalized allylboronates and systematic investigations of their stereocontrolled transformations with substituted aldehyde substrates, in order to efficiently access diverse, highly substituted target substrates. A peculiar transition in stereocontrol was observed from the polar Felkin–Anh (PFA) to the Cornforth–Evans (CE) model for alkoxy- and epoxy-substituted aldehydes. CE-type transition states were uniformly identified as minima in advanced, DFT-based computational studies of allylboration reactions of epoxy aldehydes, conforming well to the experimental data, and highlighting the underestimated relevance of this model. Furthermore, a mechanism-based rationale for the substitution pattern of the epoxide was delineated that ensures high levels of stereocontrol and renders α,β-epoxy aldehydes generally applicable substrates for target synthesis.

7.6 Multifunctional Polyoxometalate Platforms for Supramolecular Light-Driven Hydrogen Evolution

Salam Maloul [1], Matthias van den Borg[2], Carolin Müller [3,4], Linda Zedler [4], Alexander K. Mengele [1] Daniel Gaissmaier [2,5,6] Timo Jacob[2,5,6], Sven Rau [1] Benjamin Dietzek-Ivansic [3,4] and Carsten Streb [1], Chem. Eur. J. **2021**, *27*, 16846-16852

Reproduced from Ref. [167] under the CC BY-NC-ND 4.0 licence [141] and with the authors' permission.

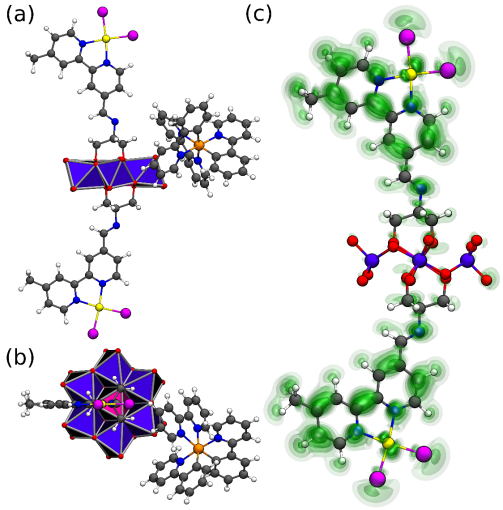

Figure 7.6. Energetically most favoured interaction sites between PS and POMPtI in (a) side view and (b) top view; (c) representation of the Fukui function calculated for the one-electron reduced POM-PtCl, shown as charge-difference plot. The iso-surfaces correspond to electron-accepting regions where an additional electron will be located (as indicated by the Fukui function). Regions with higher values are marked in darker shades of green.

[1] Institute of Inorganic Chemistry I Ulm University Albert-Einstein-Allee 11, D-89081 Ulm, Germany
[2] Institute of Electrochemistry, Ulm University, Albert-Einstein-Allee 47, D-89081 Ulm, Germany
[3] Institute of Physical Chemistry Friedrich Schiller University Jena Helmholtzweg 4, 07743 Jena (Germany)
[4] Leibniz Institute of Photonic Technologies (IPHT) Albert-Einstein-Straße 9, 07745 Jena (Germany)
[5] Helmholtz-Institute Ulm (HIU) for Electrochemical Energy Storage, Helmholtzstr. 11, 89081 Ulm, Germany
[6] Karlsruhe Institute of Technology (KIT), P.O. Box 3640, 76021 Karlsruhe, Germany

Multifunctional supramolecular systems are a central research topic in light-driven solar energy conversion. Here, we report a polyoxometalate (POM)-based supramolecular dyad, where two platinum-complex hydrogen evolution catalysts are covalently anchored to an Anderson polyoxomolybdate anion. Supramolecular electrostatic coupling of the system to an iridium photosensitizer enables visible light-driven hydrogen evolution. Combined theory and experiment demonstrate the multifunctionality of the POM, which acts as photosensitizer/catalyst-binding site and facilitates light-induced charge transfer and catalytic turnover. Chemical modification of the Pt-catalyst site leads to increased hydrogen evolution reactivity. Mechanistic studies shed light on the role of the individual components and provide a molecular understanding of the interactions which govern stability and reactivity. The system could serve as a blueprint for multifunctional polyoxometalates in energy conversion and storage.

8

Summary and Outlook

The work presented in this thesis aimed to develop a deeper understanding of the initial degradation phenomena on the metallic Li electrode induced by the impurities O_2, N_2 and H_2O from the atmosphere. Since the studies of lithium anodes are often conducted without detailed knowledge of the contamination and their morphological and electronic impact on the pristine lithium surfaces, a significant part of this work has been devoted to the study of fundamental degradation processes via *ab-initio* methods. Based on these findings, a multiscale approach for the oxidation of metallic lithium was developed to model the ongoing processes on different time and length scales.

Firstly, periodic density functional theory (DFT) was used to study the basic mechanisms of lithium oxidation by simulating the absorption of monoatomic and molecular oxygen on the low-index Li(100), Li(110) and Li(111) surfaces. As the calculations showed, the absorption was associated with a high negative charge transfer from the lithium surface to the adsorbate under the formation of coordinated cluster structures. Charge analyses revealed, that oxygen in these clusters carries a negative charge of the same order of magnitude as an oxide ion in bulk-Li_2O. On account of the surplus of lithium relative to the absorbed oxygen at the surface, the clusters belong to the class of suboxides. The geometry of the lithium suboxide clusters bears a strong resemblance to those of the heavier alkali metals rubidium and caesium, which are the only alkali metal suboxides that have been experimentally observed. Through a combined analysis

of the projected density of states (PDOS) and the sum of bond orders (SBO), we were able to identify the interaction between lithium and oxygen and the polar covalent to the ionic character of the bonds within the cluster structures. With no detectable dissociation barrier, the metal-rich clusters formed analogously upon contact between molecular oxygen and the lithium surface.
Thermodynamic analysis of oxygen absorption at highly symmetric adsorption sites on and below the surface has shown that clusters under the surface exhibit similar stability as those on top of it. As NEB calculations have demonstrated, the diffusion of oxygen between the highly symmetric adsorption sites and within the bulk material is associated with a flat potential energy surface. In this context, the low barriers for diffusion across the surface and bulk material imply not only a high mobility of oxygen but also its rapid penetration into the bulk material. To examine the impact of coverage dependence and simulate the initial oxidation process, higher oxygen coverages (up to 1 ML) were evaluated on different sites of the Li(100) and Li(110) surfaces. At higher coverages, there were not enough lithium atoms on the surface to form an ordered arrangement of cluster structures. Consequently, the lithium atoms were simultaneously attracted by several oxygen atoms, leading to larger rearrangements and a disordered surface structure. A thermodynamic classification of the most stable surface structures via a phase diagram has shown that the oxidized surfaces are energetically more stable than the pure lithium surface up to extremely low and experimentally virtually unrealizable pressures. Despite their relative stability with respect to the pristine lithium surface, oxidized surfaces must be regarded as metastable structures since bulk bulk-Li_2O is thermodynamically more stable over the entire range of chemical potentials.

To explore the processes underlying the formation of lithium nitride, analogous DFT calculations were performed for the absorption of nitrogen. With regard to the studies on initial lithium oxidation, several common characteristics were found for the absorption of monoatomic nitrogen, as it also interacted with the lithium on the surface to form characteristic cluster structures. Likewise, the absorbed nitrogen possessed a high negative charge, which was close to that of the nitride ion in bulk-Li_3N. Due to the higher negative charge, monoatomic nitrogen formed a bond with several lithium atoms during absorption on the surface and formed cluster structures with higher coordination compared to oxygen. The tendency of nitrogen to form higher coordination geometries meant that absorption below the surface was more stable from a thermodynamic point of view since a larger number of lithium bonding partners were available here.

Furthermore, for nitrogen, the interaction with lithium and the metallic character of the cluster structures was also detected by an analysis of the PDOS. Despite the strongly exothermic character of nitrogen absorption, the binding energies are much lower compared to oxygen. In comparison, monoatomic nitrogen exhibits significantly lower diffusion barriers and therefore a pronounced mobility and capability to quickly diffuse through the lithium material.
Major differences became evident in the examination of the molecular species, as molecular nitrogen did not dissociate immediately upon contact with the metallic lithium surface, but formed cluster-like compounds while retaining the stable N-N bond. The calculation of energy profiles for different diffusion and dissociation processes suggested that cleavage of the N_2 bond will preferentially occur after diffusion below the surface, as the dissociation barrier was significantly lower in this case.
A rearrangement of the surface under formation of disordered structures was also observed for higher nitrogen coverages. The thermodynamic evaluation via a phase diagram has again demonstrated that a pristine lithium surface can only be achieved under theoretical pressures. With respect to bulk Li_3N, the absorption structures are metastable for nitrogen as well.

Since lithium is known to react violently with water under the release of molecular hydrogen, adsorption/absorption structures as well as diffusion and dissociation processes of hydrogen, OH and H_2O were examined with DFT to study elemental degradation processes on metallic lithium surfaces. Again, the adsorption of monoatomic hydrogen on lithium also took place under the formation of cluster-like structures. Of the monoatomic species, hydrogen exhibited the lowest binding energies and the highest mobility on the surface and in the Li(bcc)-bulk material. Without significant charge transfer, molecular hydrogen is only weakly absorbed on the lithium surface. On Li(100), OH formed thermodynamically stable cluster structures with low energy differences, resulting in a correspondingly flat diffusion profile with low barriers. High mobility via "flip" or "twist" mechanisms was also observed for the diffusion of water molecules on Li(100).
Compared to OH dissociation, the process was favoured. Here, the Li(100)-H_2O bridge structure dissociated via a Volmer step with a low barrier, leading to a considerable gain in stability. By comparing the energy profiles of different processes, the recombination of two absorbed hydrogen atoms via a Tafel process was excluded as a source for hydrogen development. Instead, a process analogous to the Heyrovsky mechanism in

the alkaline medium was identified as the main origin of hydrogen evolution. This process showed a significantly lower dissociation barrier and implied a self-supporting effect for the cleavage of OH and water molecules at a higher coverage of hydrogen absorbates on the lithium surface.

To investigate lithium oxidation on a larger time and length scale, the data set based exclusively on DFT calculations was used to optimize the Li-O parameters for an interatomic ReaxFF potential via the KVIK optimizer. By using GCMC simulations on metallic lithium nanoparticles as a model system, it was possible to further investigate oxidation processes on a metallic lithium anode. The optimized reactive force field forms a basis for further in-depth studies of degradation phenomena at metallic lithium electrodes in batteries. By extending and adapting existing parameter sets, detailed studies are possible for the ongoing processes at the electrode-electrolyte interface. However, even without extending the parameters, the force field could provide new insights into the dendritic growth of lithium at the atomistic level. As we have shown in another study via a combined ReaxFF/kMC approach, the dendrite growth of metallic lithium is not related to an intrinsic property to form inhomogeneous surface morphologies. Since dendrite growth can thus not be detected without considering other factors, the developed force field may be used to study the influence of an oxygen-containing lithium phase on inhomogeneous lithium deposition.

A

Appendix

A.1 Theoretical studies on the initial oxidation of metallic lithium anodes

Reference systems

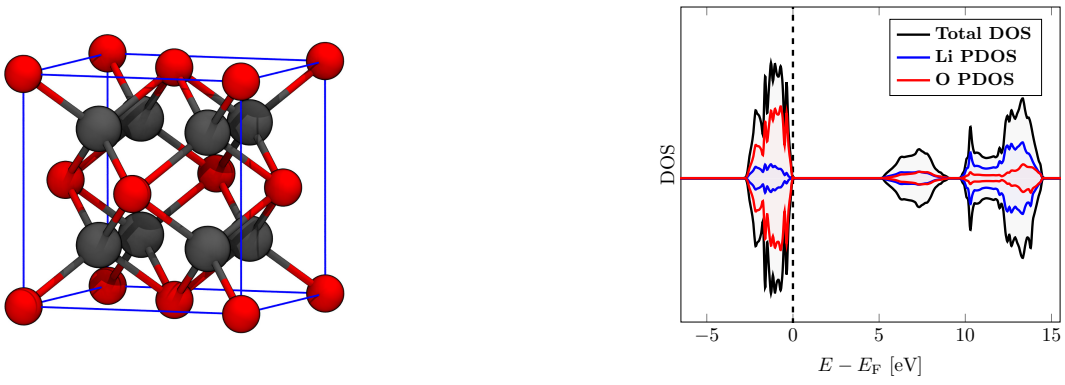

(a) (b)

Figure A.1. Unit cell for bulk-Li_2O shown in **(a)**. The lithium and oxygen atoms are represented by grey and red spheres, respectively. In **(b)** the total density of states (TDOS) for bulk-Li_2O is shown in black. The partial density of states (PDOS) of lithium is shown in blue and in red for oxygen.

Table A.1 Calculated and experimental values for O_2, Li(bcc) and Li_2O. For O_2 the bond distance (d_{O_2}) is reported in $\mathrm{\AA}$, dissociation energy $\left(E^{\mathrm{gas}}_{\mathrm{Diss},O_2}\right)$ in eV. Lattice constants (a) are reported in $\mathrm{\AA}$, cohesive energy (E_{c}) and formation energy (E_{F}) in eV, surface energies $\left(\gamma_{\mathrm{Li(hkl)}}\right)$ in $\mathrm{J \cdot m^{-2}}$ and bulk moduli (B) in GPa. The PBE and BEEF-vdW values for Li(bcc) correspond to those reported in Ref. [117] and [89].

System	Phys. const.	PBE	BEEF-vdW	Expt.
O_2	d_{O_2}	1.23	1.23	1.21 [168]
	$E^{\mathrm{gas}}_{\mathrm{Diss},O_2}$	-5.97	-5.42	-5.12 [118]
Li(bcc)	a	3.44	3.40	3.45 [169]
	E_{c}	-1.61	-1.66	-1.67 [169]
	B	13.92	15.43	13.90 [169]
	$\gamma_{\mathrm{Li}(100)}$	0.47	0.58	—
	$\gamma_{\mathrm{Li}(110)}$	0.50	0.62	0.52 [170], 0.53 [171]
	$\gamma_{\mathrm{Li}(111)}$	0.54	0.65	—
Li_2O	a	4.63	4.64	4.62 [159]
	E_{F}	-5.64	-5.75	-6.21 [118]
	B	72.07	75.50	75.00 [159]

Coverage-dependent absorption on Li(110)

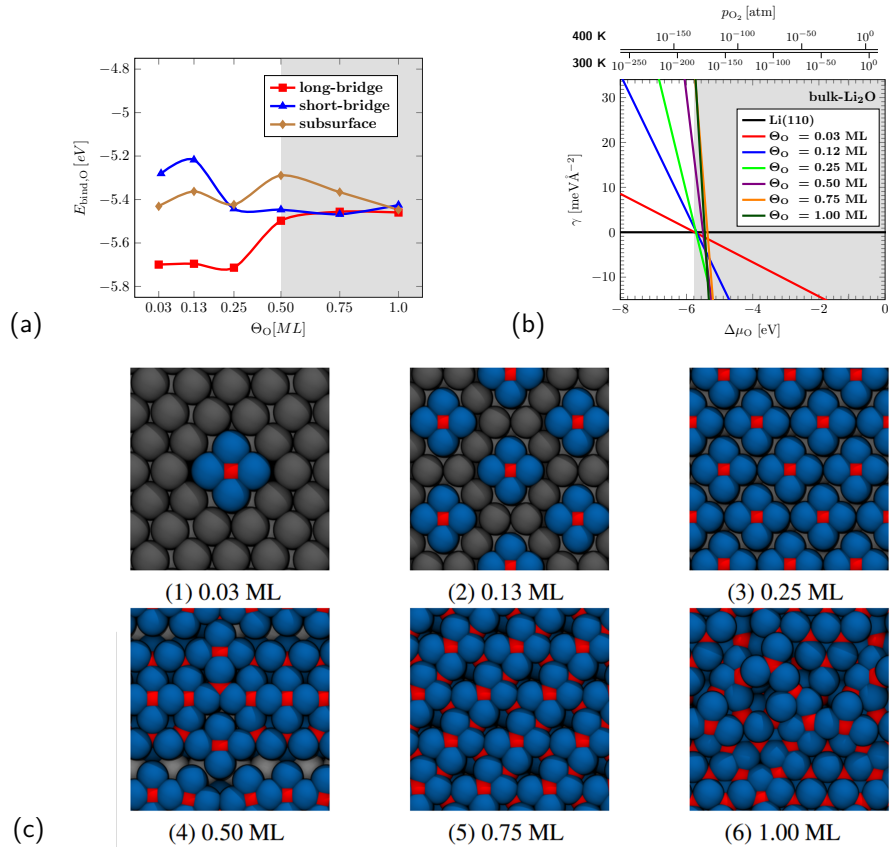

Figure A.2. Binding energies per oxygen atom $E_{\mathrm{bind,O}}$ in eV as a function of the oxygen coverage Θ_O shown in **(a)**. The grey area represents the range, where a strong reorganisation of the Li(110) surface structure to an amorphous arrangement was observed. In **(b)** a phase diagram for the surface oxidation of Li(110) as a function of the oxygen chemical potential is shown. For fixed temperatures of 300 K and 400 K the chemical potential has been translated to the corresponding pressures. The grey area resembles the oxygen-rich environment, where the Li_2O bulk oxide results as the most stable phase. In **(c)** sections of the most stable Li(110) surfaces at different oxygen coverages Θ_O are shown.

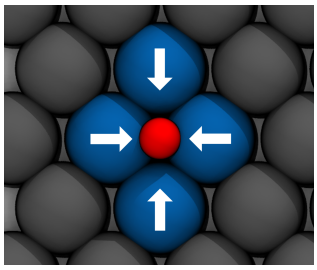

(a) long-bridge at $\Theta_O < 0.50$ ML.

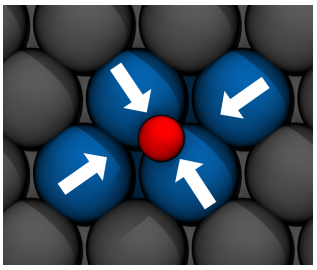

(b) short-bridge at $\Theta_O < 0.50$ ML.

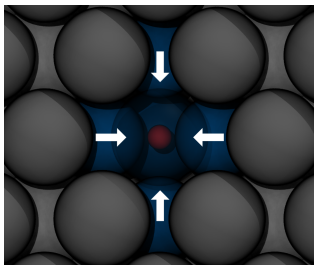

(c) subsurface at $\Theta_O < 0.50$ ML.

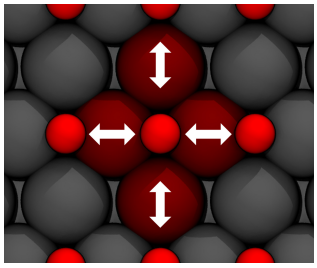

(d) long-bridge at $\Theta_O > 0.50$ ML.

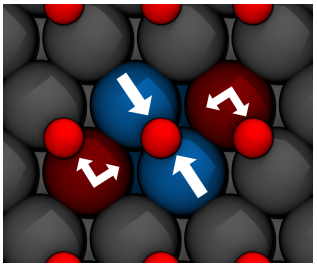

(e) short-bridge at $\Theta_O > 0.50$ ML.

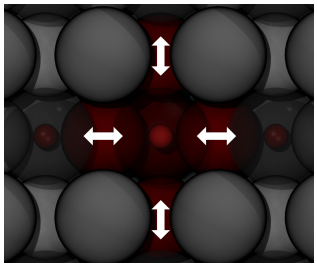

(f) subsurface at $\Theta_O > 0.50$ ML.

Figure A.3. Schematic illustration of cluster formation on Li(110), which caused rearrangements on the surface at higher coverages. The blue symbols represent the attraction of Li atoms towards oxygen at lower coverages, leading to the formation of an ordered arrangement of clusters. The red symbols depict the attraction towards several oxygen atoms at higher coverages, which lead to a reorganisation of the surface.

Table A.2 Binding energies per atom $E_{\mathrm{bind,O}}$ on the Li(110) surface as a function of the oxygen coverage Θ_O in monolayers (ML) for different arrangements of the high-symmetry adsorption sites. The energies are referenced to molecular O_2 in gas phase and are reported in eV.

Θ_O (ML)	$E_{\mathrm{bind,O}}$ (eV)		
	long-bridge	*short-bridge*	*subsurface*
0.03	-5.75	-5.28	-5.43
0.13	-5.70	-5.21	-5.36
0.25	-5.71	-5.44	-5.42
0.50	-5.50	-5.45	-5.29
0.75	-5.46	-5.47	-5.36
1.00	-5.46	-5.43	-5.44

Density of states for Li(110) absorption structures

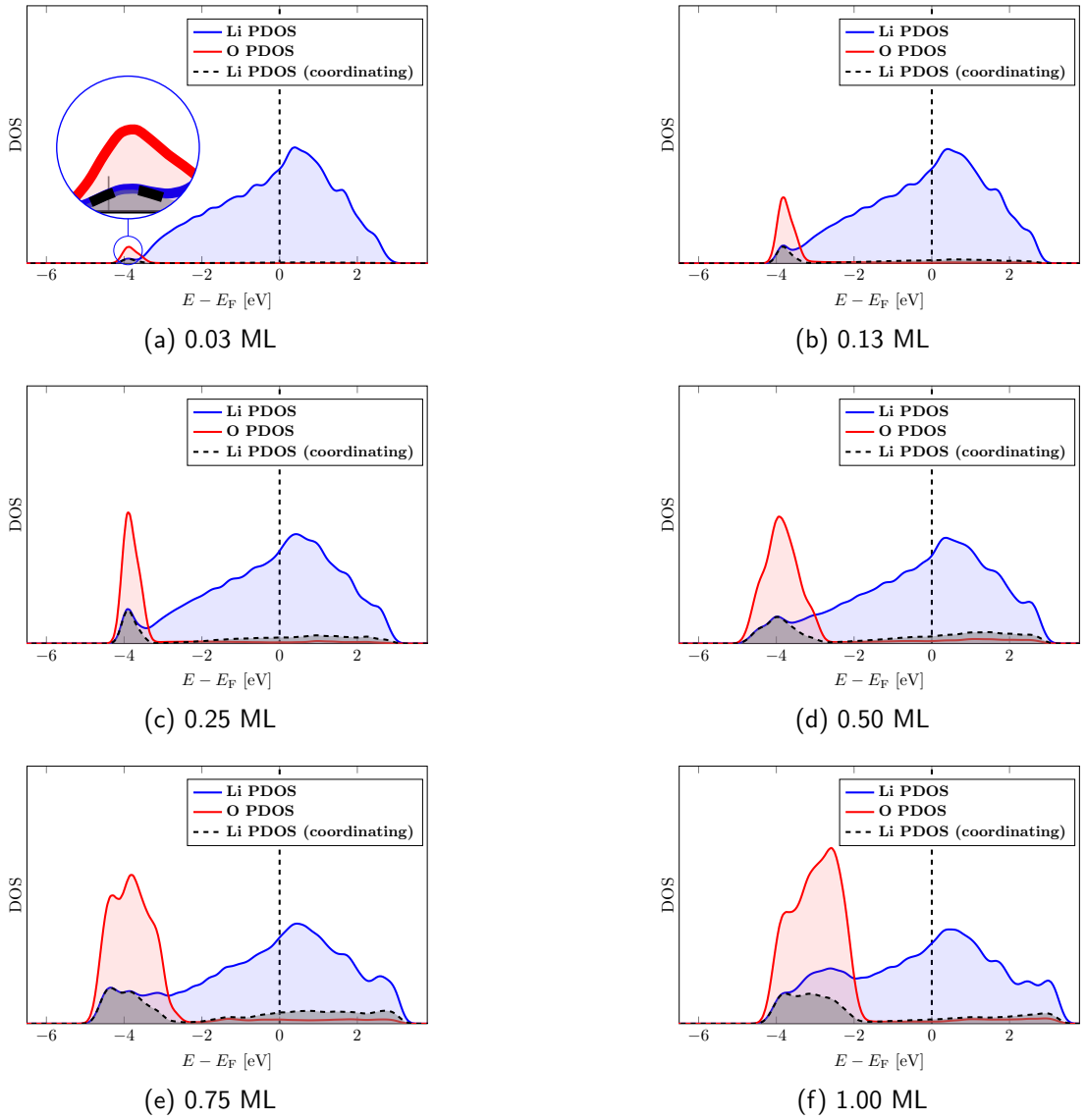

(a) 0.03 ML (b) 0.13 ML

(c) 0.25 ML (d) 0.50 ML

(e) 0.75 ML (f) 1.00 ML

Figure A.4. Projected density of states (PDOS) for the most stable Li(100) absorption structures at different oxygen coverages Θ_O. Shown are the averaged PDOS of all lithium (blue) and oxygen (red) atoms. The states that belong to a lithium atom coordinating an oxygen atom are represented by a black dashed line.

A.2 A first principle study on the initial nitride formation on lithium metal

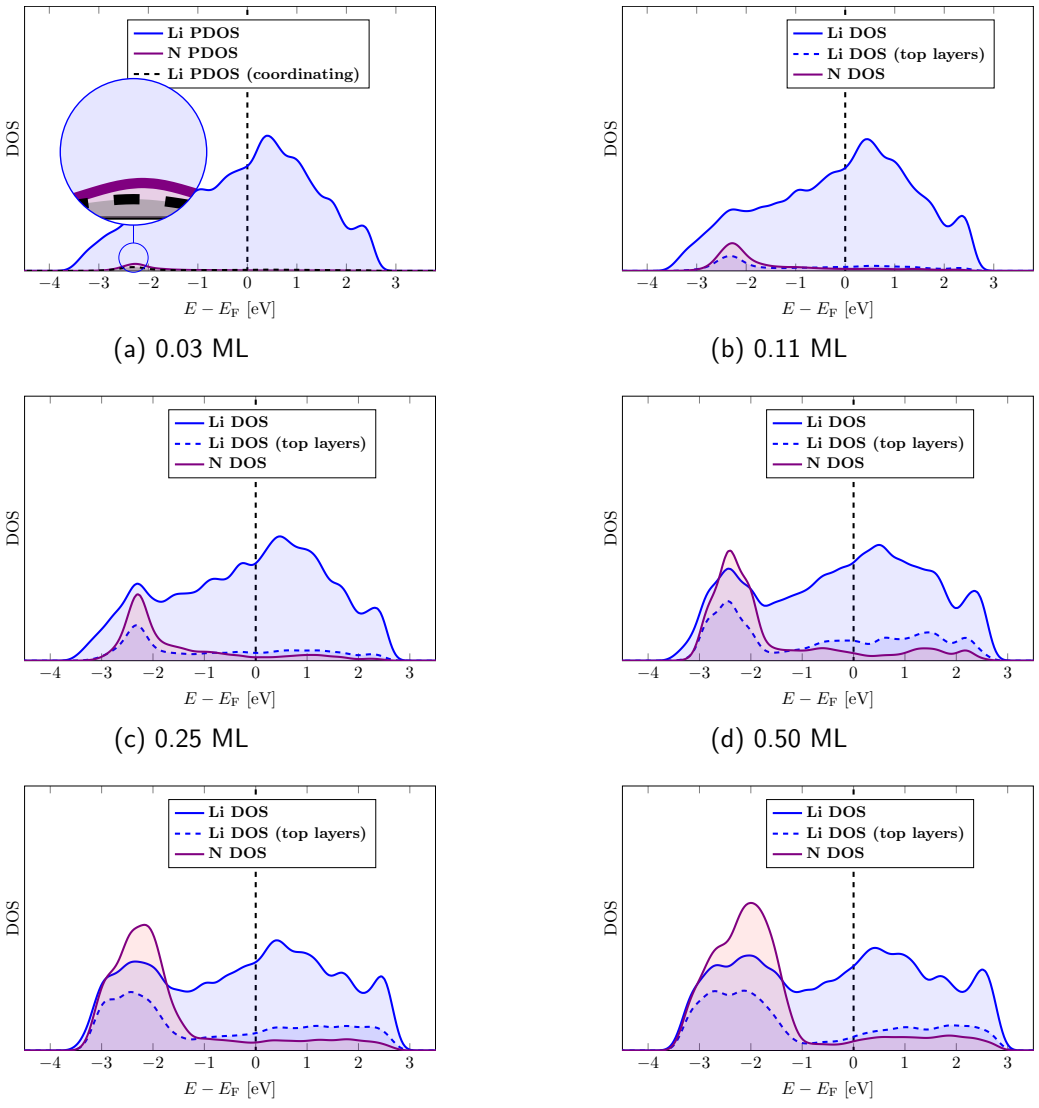

(a) 0.03 ML (b) 0.11 ML

(c) 0.25 ML (d) 0.50 ML

(e) 0.75 ML (f) 1.00 ML

Figure A.5. Projected density of states (PDOS) for the most stable Li(100) absorption structures at different nitrogen coverages Θ_N. Shown are the averaged PDOS of all lithium (blue) and nitrogen (purple) atoms. The dashed lines display the states which can be attributed to nitrogen coordinating lithium atoms of the top layers.

A.3 Atomistic studies on water-induced lithium corrosion

Convergence studies

Table A.3 Convergence study for the energy cutoff and number of k-points. Shown are the binding energies per molecule $E_{bind,mol}$ on Li(100) for the respective settings. The Li(100)-$H_2O_{bri.}$ structure corresponds to a Li(100) surface with a single water molecule on the bridge position. On the Li(100)-$OH_{sidebri.}$ + $H_{bri.}$ structure the water molecule dissociated in a OH molecule in the *sidebridge* and a H atom in the *bridge* position. The energies were related to a single water molecule in the gas phase and are reported in eV.

Structure	***k***-points	300 eV	400 eV	500 eV
Li(100)-$H_2O_{bri.}$	2x2x1	-0.788	-0.777	-0.780
	3x3x1	-0.788	-0.777	-0.780
	4x4x1	-0.788	-0.777	-0.780
	5x5x1	-0.788	-0.777	-0.780
	6x6x1	-0.788	-0.777	-0.780
	7x7x1	-0.788	-0.777	-0.780
Li(100)-$OH_{sidebri.}$ + $H_{bri.}$	2x2x1	-0.788	-0.777	-0.780
	3x3x1	-0.788	-0.777	-0.780
	4x4x1	-0.788	-0.777	-0.780
	5x5x1	-0.788	-0.777	-0.780
	6x6x1	-0.788	-0.777	-0.780
	7x7x1	-0.788	-0.777	-0.780

Barriers and frequency analysis of transition states

Table A.4 ΔE_{back} and ΔE_{for} barriers in eV for the respective backward and forward diffusion, dissociation and reaction processes of OH and H_2O molecules on Li(100).

Process			ΔE_{for}	ΔE_{back}
Li(100)-H_{hollow}	$\rightarrow$	Li(100)-H_{bridge}	0.151	0.126
Li(100)-H_{bridge}	$\rightarrow$	Li(100)-$H_{\mathrm{subbridge}}$	0.124	0.003
Li(100)-$H_{\mathrm{subbridge}}$	$\rightarrow$	Li(100)-$H_{\mathrm{subsurface}}$	0.082	0.040
Li(100)-$H_{2,\mathrm{top}}$	$\rightarrow$	Li(100)-2$H_{\mathrm{bridge,bridge}}$	0.271	1.444
Li(bcc)-$H_{\mathrm{bulk},1}$	$\longrightarrow$	Li(bcc)-$H_{\mathrm{bulk},2}$	0.063	0.063
Li(100)-$OH_{\mathrm{bri.}}$	$\rightarrow$	Li(100)-$OH_{\mathrm{sidebri.}}$	0.08	0.12
Li(100)-$OH_{\mathrm{sidebri.}}$	$\rightarrow$	Li(100)-$OH_{\mathrm{sidehol.}}$	0.03	0.06
Li(100)-$OH_{\mathrm{sidehol.}}$	$\rightarrow$	Li(100)-$OH_{\mathrm{hol.}}$	0.02	0.01
Li(100)-$OH_{\mathrm{sidehol.}}$	$\rightarrow$	Li(100)-$O_{\mathrm{hol.}}$ + $H_{\mathrm{hol.}}$	0.89	2.27
Li(100)-$OH_{\mathrm{sidehol.}}$ + $H_{\mathrm{bri.}}$	$\rightarrow$	Li(100)-$O_{\mathrm{hol.}}$ + $H_{2,\mathrm{top}}$	0.40	0.61
Li(100)-$H_2O_{\mathrm{bri.},1}$ (flip-bridge)	$\rightarrow$	Li(100)-$H_2O_{\mathrm{bri.},2}$	0.05	0.05
Li(100)-$H_2O_{\mathrm{bri.},1}$ (twist)	$\rightarrow$	Li(100)-$H_2O_{\mathrm{bri.},2}$	0.14	0.14
Li(100)-$H_2O_{\mathrm{bri.},1}$ (flip-top)	$\rightarrow$	Li(100)-$H_2O_{\mathrm{bri.},2}$	0.15	0.15
Li(100)-$H_2O_{\mathrm{bri.}}$	$\rightarrow$	Li(100)-$OH_{\mathrm{sidebri.}}$ + $H_{\mathrm{bri.}}$	0.22	2.11
Li(100)-$H_2O_{\mathrm{bri.}}$ + $H_{\mathrm{bri.}}$ (front)	$\rightarrow$	Li(100)-$OH_{\mathrm{sidebri.}}$ + $H_{2,\mathrm{top}}$	0.06	0.66
Li(100)-$H_2O_{\mathrm{bri.}}$ + $H_{\mathrm{bri.}}$ (side)	$\rightarrow$	Li(100)-$OH_{\mathrm{sidebri.}}$ + $H_{2,\mathrm{top}}$	0.14	0.89

Adsorbate-adsorbate interactions

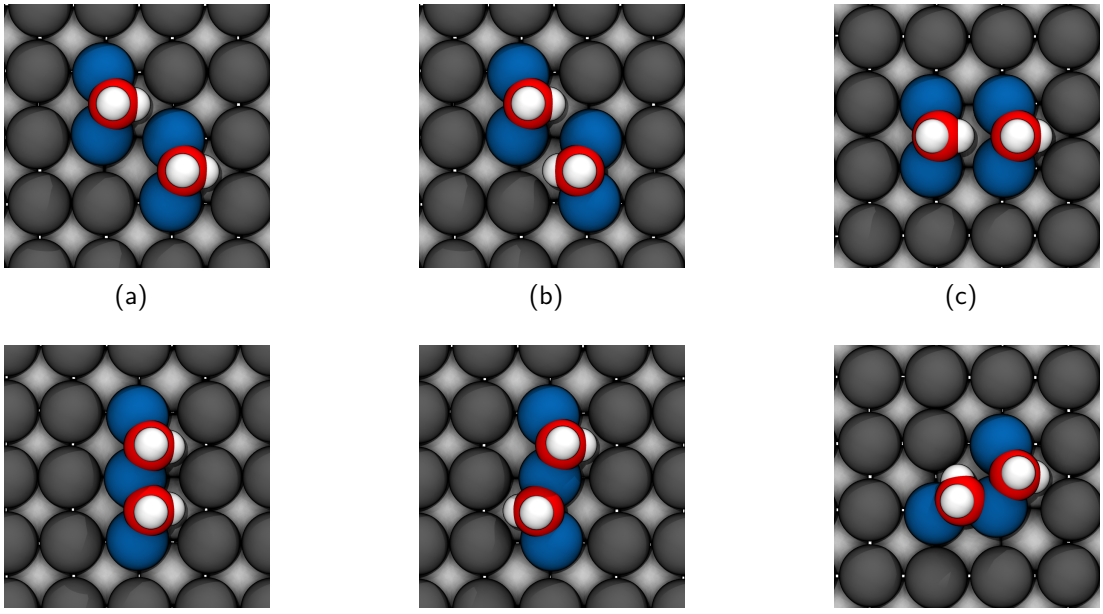

Figure A.6. Top view of the different arrangements of H_2O dimers on Li(100) in **(a)**-**(f)**. Hydrogen is shown in white, oxygen in red and the coordinating lithium atoms in blue.

Table A.5 Binding energies per H_2O molecule $E^{\mathrm{dim}}_{\mathrm{bind,mol}}$ for the respective arrangements of a water dimer on Li(100) shown in A.6. The energies were related to water in the gas phase and are reported in eV. The interaction energy E_{Int} refers to the difference of the binding energy of the water dimers towards the one of a single water molecule $E^{\mathrm{sing}}_{\mathrm{bind,mol}}$ and is reported in meV: $E_{\mathrm{Int}} = E^{\mathrm{dim}}_{\mathrm{bind,mol}} - E^{\mathrm{sing}}_{\mathrm{bind,mol}}$.

	Structure	$E^{\mathrm{dim}}_{\mathrm{bind,mol}}$	E_{Int}
Li(100)-$H_2O_{\mathrm{bri.}}$	**(a)**	-0.706	71
	(b)	-0.767	10
	(c)	-0.763	14
	(d)	-0.767	10
	(e)	-0.771	5
	(f)	-0.729	48

A.4 ReaxFF guided simulation of lithium anode oxidation

ReaxFF parameter set

Listing A.1. Overview of the ReaxFF parameter set for the description of Li-Li, and Li-O interactions.

```
[ ereaxff acks2 ] Reactive MD-force field: M. van den Borg (2023) - Li/O FF
 41       ! Number of general parameters
   50.0000 !Overcoordination parameter
    9.5469 !Overcoordination parameter
    1.6725 !Valency angle conjugation parameter
    1.7224 !Triple bond stabilisation parameter
    6.8702 !Triple bond stabilisation parameter
   54.6742 !C2-correction
    1.0588 !Undercoordination parameter
    4.6000 !Triple bond stabilisation parameter
   12.1176 !Undercoordination parameter
   13.3056 !Undercoordination parameter
  -34.5448 !Triple bond stabilization energy
    0.0000 !Lower Taper-radius
   10.0000 !Upper Taper-radius
    2.8793 !Not used
   20.0000 !Valency undercoordination
    6.0891 !Valency angle/lone pair parameter
    1.0563 !Valency angle
    2.0384 !Valency angle parameter
    6.1431 !Not used
    6.9290 !Double bond/angle parameter
    0.3989 !Double bond/angle parameter: overcoord
    3.9954 !Double bond/angle parameter: overcoord
   -2.4837 !Not used
    8.5385 !Torsion/BO parameter
    6.7491 !Torsion overcoordination
    0.1414 !Torsion overcoordination
    1.0000 !Conjugation 0 (not used)
    1.1348 !Conjugation
    1.5591 !vdWaals shielding
    0.1000 !Cutoff for bond order (*100)
    1.7602 !Valency angle conjugation parameter
    0.6991 !Overcoordination parameter
   50.0000 !Overcoordination parameter
    1.8512 !Valency/lone pair parameter
  548.6451 !ACKS2 softness parameter
   20.0000 !Scale factor (d) in dispersion (LJ)
    5.0000 !Gauss exponent for explicit electrons
    0.0000 !1: disable undecoord term in val angle
```

```
   0.7903 !Valency angle conjugation parameter
   0.0000 !1: triple bond stabilization for all bonds
   5.7000 !eReax taper radius for electrons and holes
 2    ! Nr of atoms; cov.r; valency;a.m;Rvdw;Evdw;gammaEEM;cov.r2;#
           alfa;gammavdW;valency;Eunder;Eover;chiEEM;etaEEM;n.u.
           cov r3;Elp;Heat inc.;n.u.;n.u.;n.u.;n.u.
           ov/un;val1;n.u.;val3,vval4
Li   1.9770   1.0000   6.9410   2.0696   0.4697   0.9521  -0.1000   1.0000
     8.7307   1.2115   1.0000   0.0000   0.2000  -3.0000  10.0241   6.0000
    -1.0000   0.0000  37.5000   5.4409   6.9107   0.1973   6.5000   0.0000
    -7.8851   2.2989   0.0138   1.0000   2.8103   0.0000   0.0000   0.0000
O    1.2450   2.0000  15.9990   2.3890   0.1000   1.0898   1.0548   6.0000
     9.7300  13.8449   4.0000  37.5000 116.0768   8.5000   8.3122   2.0000
     0.9049   0.4056  59.0626   3.5027   0.7640   0.0021   3.2927   0.0000
    -3.5500   2.9000   1.0493   4.0000   2.9225   0.0000   0.0000   0.0000
 3      ! Nr of bonds; Edis1;LPpen;n.u.;pbe1;pbo5;13corr;pbo6
                       pbe2;pbo3;pbo4;Etrip;pbo1;pbo2;ovcorr
 1  1  40.3642   0.0000   0.0000   0.6418   0.3000   0.0000  26.0000   0.4599
       0.1316   0.0000  12.0000   1.0000  -0.0862   4.6470   0.0000   0.0000
 2  2 142.2858 145.0000  50.8293   0.2506  -0.1000   1.0000  29.7503   0.6051
       0.3451  -0.1055   9.0000   1.0000  -0.1225   5.5000   1.0000   0.0000
 1  2  74.5683  -0.0200   0.0000  -0.2205   0.3000   0.0000   6.0000   0.1833
       1.8153  -0.2500  11.9965   1.0000  -0.2648   4.1482   0.0000   0.0000
 1    ! Nr of off-diagonal terms; Ediss;Ro;gamma;rsigma;rpi;rpi2
 1  2   0.0232   2.4481  11.2060   1.5941   0.0000   0.0000
 1     ! Nr of angles;at1;at2;at3;Thetao,o;ka;kb;pv1;pv2
 2  2  2  80.7324  30.4554   0.9953   0.0000   1.6310  50.0000   1.0783
 2    ! Nr of torsions;at1;at2;at3;at4;;V1;V2;V3;V2(BO);vconj;n.u;n
 2  2  2  2  -2.5000  -4.0000   1.0000  -2.5000  -1.0000   0.0000   0.0000
 0  2  2  0   0.5511  25.4150   1.1330  -5.1903  -1.0000   0.0000   0.0000
 0    !H-bonds
```

List of abbreviations

ACKS2	atom-condensed Kohn-Sham density functional theory approximated to second order
BEEF-vdW	Bayesian error estimation functional with van der Waals correlation
CI-NEB	climbing image-nudged elastic band
CE	Coulombic efficiency
DFT	density functional theory
DOS	density of states
EOS	equation of states
GCMC	grand canonical Monte Carlo
GGA	generalised gradient approximation
GHG	greenhouse gases
kMC	kinetic Monte Carlo
LDA	local density approximation
LSDA	local spin density approximation
LIB	lithium-ion battery
MC	Monte Carlo
MD	molecular dynamics
NEB	nudged elastic band
PDOS	projected density of states
RDF	radial distribution function
SBO	sum of bond orders
SCF	self-consistent field
SE	Schrödinger equation
SEI	solid electrolyte interphase
SHE	standard hydrogen electrode
VASP	Vienna Ab initio Simulation Package
XRD	X-ray diffraction

Bibliography

[1] IPCC, *Climate Change 2021: The Physical Science Basis. Contribution of Working Group I to the Sixth Assessment Report of the Intergovernmental Panel on Climate Change*, Cambridge University Press, Cambridge, United Kingdom and New York, NY, USA, 2021.

[2] IPCC, *Climate Change 2022: Impacts, Adaptation and Vulnerability. Contribution of Working Group II to the Sixth Assessment Report of the Intergovernmental Panel on Climate Change*, Cambridge University Press, Cambridge, UK and New York, USA, 2022.

[3] A. Weisheimer and T. N. Palmer, *Geophys. Res. Lett.*, 2005, **32**, 1–5.

[4] Y. Hirabayashi, S. Kanae, S. Emori, T. Oki and M. Kimoto, *Hydrological Sciences Journal*, 2008, **53**, 754–772.

[5] C. D. Allen, A. K. Macalady, H. Chenchouni, D. Bachelet, N. McDowell, M. Vennetier, T. Kitzberger, A. Rigling, D. D. Breshears, E. H. Hogg, P. Gonzalez, R. Fensham, Z. Zhang, J. Castro, N. Demidova, J. H. Lim, G. Allard, S. W. Running, A. Semerci and N. Cobb, *For. Ecol. Manag.*, 2010, **259**, 660–684.

[6] A. Hunt and P. Watkiss, *Climatic Change*, 2011, **104**, 13–49.

[7] V. W. Keener, J. J. Marra, M. L. Finucane, D. Spooner and M. H. Smith, *Climate Change and Pacific Islands: Indicators and Impacts. Report for The 2012 Pacific Islands Regional Climate Assessment*, Washington, DC: Island Press, 2012.

[8] J. L. Hatfield and J. H. Prueger, *Weather Clim. Extrem.*, 2015, **10**, 4–10.

[9] A. Ali and O. Erenstein, *Clim. Risk Manag.*, 2017, **16**, 183–194.

[10] X. Guo, Z. Zhang, X. Zhang, M. Bi and P. Das, *Environ. Res. Lett.*, 2023, **18**, 064035.

[11] EPA, *Inventory of U.S. Greenhouse Gas Emissions and Sinks: 1990-2022*, U.S. Environmental Protection Agency, 2024.

[12] J. Morfeldt, S. Davidsson Kurland and D. J. Johansson, *Transp. Res. D*, 2021, **95**, 102807.

[13] J. M. Tarascon and M. Armand, *Nature*, 2001, **414**, 359–367.

[14] N. Nitta, F. Wu, J. T. Lee and G. Yushin, *Mater. Today*, 2015, **18**, 252–264.

[15] T. Kim, W. Song, D.-Y. Son, L. K. Ono and Y. Qi, *J. Mater. Chem. A*, 2019, **7**, 2942–2964.

[16] Y. Chen, Y. Kang, Y. Zhao, L. Wang, J. Liu, Y. Li, Z. Liang, X. He, X. Li, N. Tavajohi and B. Li, *J. Energy Chem.*, 2021, **59**, 83–99.

[17] A. Manthiram, *Nat. Commun.*, 2020, **11**, 1550.

[18] M. B. Armand, in *Intercalation Electrodes*, ed. D. W. Murphy, J. Broadhead and B. C. H. Steele, Springer US, Boston, MA, 1980, pp. 145–161.

[19] A. Mauger, C. M. Julien, J. B. Goodenough and K. Zaghib, *J. Electrochem. Soc.*, 2020, **167**, 070507.

[20] E. C. Evarts, *Nature*, 2015, **526**, S93–S95.

[21] T. Liu, J. P. Vivek, E. W. Zhao, J. Lei, N. Garcia-Araez and C. P. Grey, *Chem. Rev.*, 2020, **120**, 6558–6625.

[22] P. G. Bruce, S. A. Freunberger, L. J. Hardwick and J.-M. Tarascon, *Nat. Mater.*, 2012, **11**, 19–29.

[23] B. S. van Schalkwijk, *Advances in Lithium-Ion Batteries*, Kluwer Academic Publishers, 2002.

[24] M. Winter, J. O. Besenhard, M. E. Spahr and P. Novak, *Adv. Mater.*, 1998, **10**, 725–763.

[25] M. Winter, *Z. Phys. Chem*, 2009, **223**, 1395–1406.

[26] J.-g. Z. Wu and X. Wesley, *Lithium Metal Anodes and Rechargeable Lithium Metal Batteries Ji-Guang Zhang, Wu Xu, and Wesley A. Henderson*, Springer Series in Materials Science, p. 857.

[27] R. Wang, W. Cui, F. Chu and F. Wu, *J. Energy Chem.*, 2020, **48**, 145–159.

[28] B. Liu, J. G. Zhang and W. Xu, *Joule*, 2018, **2**, 833–845.

[29] B. Acebedo, M. C. Morant-Miñana, E. Gonzalo, I. Ruiz de Larramendi, A. Villaverde, J. Rikarte and L. Fallarino, *Adv. Energy Mater.*, 2023, **13**, 2203744.

[30] E. Peled, *J. Electrochem. Soc.*, 1979, **126**, 2047–2051.

[31] O. G. E. Peled and G. Ardel, *J. Electrochem. Soc.*, 1997, **144**, L208.

[32] J. B. Goodenough and Y. Kim, *Chem. Mater*, 2010, **22**, 587–603.

[33] D. Aurbach and A. Zaban, *J. Electroanal. Chem.*, 1993, **348**, 155–179.

[34] D. Aurbach, B. Markovsky, A. Shechter and Y. Ein-Eli, *J. Electrochem. Soc.*, 1996, **143**, 3809–3820.

[35] J. Vettera, P.Novak, M. R. Wagner, C.Veit, K.-C. Möller, J. O. Besenhard, M. Winter, M. Wohlfahrt-Mehrens, C. Vogler and A. Hammouche, *J. Power Sources*, 2005, **147**, 269–281.

[36] X. Cheng, R. Zhang, C. Zhao, F. Wei, J. Zhang and Q. Zhang, *Adv. Sci.*, 2016, **3**, 1500213.

[37] G. Bieker, M. Winter and P. Bieker, *Phys. Chem. Chem. Phys.*, 2015, **17**, 8670–8679.

[38] A. Ramasubramanian, V. Yurkiv, T. Foroozan, M. Ragone, R. Shahbazian-Yassar and F. Mashayek, *ACS Appl. Energy Mater.*, 2020, **11**, 10560–10567.

[39] Q. Liu, H. Wang, C. Jiang and Y. Tang, *Energy Storage Mater.*, 2019, **23**, 566–586.

[40] P. Jankowski, W. Wieczorek and P. Johansson, *Energy Storage Mater.*, 2019, **20**, 108–117.

[41] G. Wang, X. Xiong, D. Xie, X. Fu, X. Ma, Y. Li, Y. Liu, Z. Lin, C. Yang and M. Liu, *Energy Storage Mater.*, 2019, **23**, 701–706.

[42] Y. Li and S. Guo, *Matter*, 2021, **4**, 1142–1188.

[43] E. K. Johnson and W. N. Hubbard, *J. Chem. Thermodyn.*, 1975, **7**, 781–786.

[44] W. McLean, J. A. Schultz, L. G. Pedersen and R. C. Jarnagin, *Surf. Sci.*, 1979, **83**, 354–366.

[45] J. R. Hoenigman and R. G. Keil, *Surf. Sci.*, 1984, **18**, 207–222.

[46] K. R. Zavadil and N. R. Armstrong, *Surf. Sci.*, 1990, **230**, 47–60.

[47] H. Takeshita and H. Watanabe, *J. Nucl. Mater.*, 1993, **207**, 92–97.

[48] G. Zhuang, Y. Chen and P. N. R. Jr., *Surf. Sci.*, 1998, **418**, 139–149.

[49] M. Wu, Z. Wen, Y. Liu, X. Wang and L. Huang, *J. Power Sources*, 2011, **196**, 8091–8097.

[50] K. J. Harry, D. T. Hallinan, D. Y. Parkinson, A. A. MacDowell and N. P. Balsara, *Nat. Mater.*, **13**, 69–73.

[51] P. Hohenberg and W. Kohn, *Phys. Rev. B*, **136**, 864–871.

[52] W. Kohn and L. J. Sham, *Phys. Rev. A*, 1965, **140**, 1133–1138.

[53] A. C. T. van Duin, S. Dasgupta, F. Lorant and W. A. G. III, *Journal of Physical Chemistry A*, 2001, **105**, 9396–9409.

[54] E. Schrödinger, *Phys. Rev.*, 1926, **28**, 1049.

[55] M. Born and J. R. Oppenheimer, *Ann. Phys.*, 1927, **84**, 457.

[56] A. Groß, *Theoretical Surface Science*, Springer Berlin Heidelberg, 2nd edn, 2009.

[57] D. M. Ceperley and B. Alder, *Phys. Rev. Lett.*, 1980, **45**, 566.

[58] M. Ernzerhof, J. P. Perdew and K. Burke, *Int. J. Quantum Chem.*, 1997, **64**, 285–295.

[59] J. P. Perdew, K. Burke and M. Ernzerhof, *Phys. Rev. Lett.*, 1996, **77**, 3865.

[60] J. Wellendorff, K. T. Lundgaard, A. Mogelhoj, V. Petzold, D. D. Landis, J. K. Norskov, T. Bligaard and K. W. Jacobsen, *Phys. Rev. B*, 2012, **85**, 235149.

[61] M. J. Field, *A Practical Introduction to the Simulation of Molecular Systems.*, Cambridge University Press, 2nd edn, 2007.

[62] L. Pauling, *J. Am. Chem. Soc.*, 1947, **69**, 542–553.

[63] J. Tersoff, *Phys. Rev. B*, 1988, **37**, 6991–7000.

[64] D. W. Brenner, *Phys. Rev. B*, 1990, **15**, 9459–9471.

[65] B. Kirchhoff, L. Braunwarth, C. Jung, H. Jonsson, D. Fantauzzi and T. Jacob, *Small*, 2020, **16**, 1905159.

[66] B. Kirchhoff, C. Jung, H. Jonsson, D. Fantauzzi and T. Jacob, *J. Phys. Chem. C*, 2022, **126**, 6773.

[67] K. Kleiner, A. Comas-Vives, M. Naderian, J. E. Mueller, D. Fantauzzi, M. Mesgar, J. A. Keith, J. Anton and T. Jacob, *Adv. Phys. Chem.*, 2011, **2011**, 252591.

[68] M. van den Borg, Fantauzzi, D. Gaissmaier, D. Fantauzzi, E. Knobbe and T. Jacob, *Appl. Surf. Sci.*, **555**, 149447.

[69] R. D. Rauh, K. M. Abraham, G. F. Pearson, J. K. Surprenant and S. B. Brummer, *J. Electrochem. Soc*, 1979, **126**, 523.

[70] A. Manthiram, Y. Fu, S.-H. Chung, C. Zu and Y.-S. Su, *Chem Rev.*, 2014, **114**, 11751–11787.

[71] Y. Yang, M. T. McDowell, A. Jackson, J. J. Cha, S. S. Hong and Y. Cui, *Nano Lett.*, 2010, **10**, 1486–1491.

[72] M.-K. Song, E. J. Cairns and Y. Zhang, *Nanoscale*, 2013, **5**, 2186–2204.

[73] B. D. McCloskey, D. S. Bethune, R. M. Shelby, G. Girishkumar and A. C. Luntz, *J. Phys. Chem. Lett*, 2011, **2**, 1161–1166.

[74] X. Z. Richard Padbury, *J. Power Sources*, 2011, **196**, 4436–4444.

[75] P. G. Bruce, S. A. Freunberger, L. J. Hardwick and J.-M. Tarascon, *Nat. Mater.*, 2012, **11**, 19–29.

[76] J.Read, *J. Electrochem. Soc.*, 2002, **149**, A1190–A1195.

[77] J. Christensen, P. Albertus, R. S. Sanchez-Carrera, T. Lohmann, B. Kozinsky, R. Liedtke, J. Ahmed and A. Kojic, *J. Electrochem. Soc.*, 2012, **159**, R1–R30.

[78] Z. Takehara, *J. Power Sources*, 1997, **68**, 82–86.

[79] D. Aurbach, Y. Gofer, Z. Lu, A. Schechter, O. Chusid, H. Gizbar, Y. Cohen, V. Ashkenazi, M. Moshkovich, R. Turgeman and E. Levi, *J. Power Sources*, 2001, **97**, 28–32.

[80] J. Becking, A. Gröbmeyer, M. Kolek, U. Rodehorst, S. Schulze, M. Winter, P. Bieker and M. C. Stan, *Adv. Mater. Interfaces*, 2017, **4**, 1700166.

[81] B. Scrosati and J. Garche, *J. Power Sources*, 2010, **195**, 2419–2430.

[82] D. Ensling, A. Thissen and W. Jaegermann, *Appl. Surf. Sci.*, 2008, **255**, 4355–4704.

[83] S. L. Koch, B. J. Morgan, S. Passerini and G. Teobaldi, *J. Power Sources*, 2015, **296**, 150–161.

[84] A. Etxebarria, S. L. Koch, O. Bondarchuk, S. Passerini, G. Teobaldi and M. A. Munoz-Marquez, *Adv. Mater.*, 2020, **10**, 2000520.

[85] X. Lua and X. Liao, *J. Materiomics*, 2020, **6**, 692–701.

[86] G. Kresse and J. Hafner, *Phys. Rev. B*, 1993, **47**, 558(R).

[87] G. Kresse and J. Furthmueller, *Phys. Rev. B*, 1996, **54**, 11169.

[88] G. Kresse and Furthmueller, *Computational Materials Science*, 1996, **6**, 11169.

[89] D. Gaissmaier, M. van den Borg, D. Fantauzzi and T. Jacob, *ChemSusChem.*, 2019, **13**, 771–783.

[90] John P. Perdew Kieron Burke and M. Ernzerhof, *Phys. Rev. Lett.*, 1996, **77**, 3865.

[91] S. Grimme, J. Antony, S. Ehrlich and H. Krieg, *J. Chem. Phys.*, 2010, **132**, 154104.

[92] Y.-X. Yu, *J. Phys. Chem. C*, 2019, **123**, 205–213.

[93] J. H. Li, J. Wu and Y. X. Yu, *J. Phys. Chem. C*, 2020, **124**, 9089–9098.

[94] R. Bader, *Atoms in Molecules: A Quantum Theory*, Oxford University Press, Oxford, 1990.

[95] G. Henkelman, A. Arnaldsson and H. Jonsson, *Comput. Mater. Sci.*, 2006, **36**, 354–360.

[96] T. A. Manz and N. G. Limas, *RSC Adv.*, 2016, **6**, 47771–47801.

[97] N. G. Limas and T. A. Manz, *RSC Adv.*, 2016, **6**, 45727–45747.

[98] T. A. Manz, *RSC Adv.*, 2017, **72**, 45552–45581.

[99] G. Henkelman and H. Jonsson, *J. Chem. Phys*, 2000, **113**, 9978–9985.

[100] G. Henkelman, B. P. Uberuaga and H. Jonsson, *J. Chem. Phys*, 2000, **113**, 9901–9904.

[101] H. J. Monkhorst and J. D. Pack, *Phys. Rev. B*, 1976, **13**, 5188.

[102] K. Reuter. and M. Scheffler, *Phys. Rev. B*, 2001, **65**, 35406.

[103] A. Simon, *Coord. Chem. Rev.*, 1997, **163**, 253–270.

[104] G. Ebbinghaus and A. Simon, *Chem. Phys.*, 1979, **43**, 117–133.

[105] A. Simon, *Z. Anorg. Allg. Chem.*, 1973, **395**, 301–319.

[106] A. Simon, *Z. Anorg. Allg. Chem.*, 1976, **422**, 208–218.

[107] E. Gmelin, A. Simon, W. Braemer and R. Villar, *J. Chem. Phys.*, 1982, **76**, 6256–6261.

[108] S. Arndt, *Handbook of Solid State Chemistry*, Wiley-VCH„ 2017, vol. 6.

[109] F. Finocchi and C. Noguera, *Phys. Rev. B*, 1996, **53**, 4989–4998.

[110] K. C. Lau, R. S. Assary, P. Redfern, J. Greeley and L. A. Curtiss, *J. Phys. Chem.*, 2012, **116**, 23890–23896.

[111] F. Finocchi and C. Noguera, *Phys. Rev. B*, 1998, **57**, 11464–14646.

[112] R. O. Jones, A. I. Lichtenstein and J. Hutter, *J. Chem. Phys.*, 1996, **106**, 4566.

[113] P. v. R. Schleyer, Wuerthwein, E. Ulrich and J. A. Pople, *J. Am. Chem. Soc.*, 1982, **104**, 5839–5841.

[114] M. Gutowski and J. Simons, *J. Phys. Chem.*, 1994, **98**, 8326–8330.

[115] C. H. Wu, *Chemical Physics Letters*, 1987, **139**, 357–359.

[116] C. Brechignac, P. Cahuzac, F. Carlier, M. de Frutos, J. Leygnier and J. P. Roux, *J. Chem. Phys.*, 1993, **99**, 6848–6855.

[117] D. Gaissmaier, D. Fantauzzi and T. Jacob, *J. Chem. Phys.*, 2019, **150**, 41723.

[118] M. W. Chase, *NIST-JANAF Thermochemical Tables*, American Institute of Physics, 4th edn, 1998.

[119] M. D. Radin, J. F. Rodriguez, F. Tian and D. J. Siegel, *J. Am. Chem. Soc.*, 2012, **134**, 1093–1103.

[120] B. A.Boukamp and R. A.Huggins, *Mater. Res. Bull.*, **13**, 23–32.

[121] T. Lapp, S. Skaarup and A. Hooper, *Solid State Ion.*, 1983.

[122] A. Rabenau, *Solid State Ion.*, 1982, **6**, 277–293.

[123] P. Chen, Z. Xiong, J. Luo, J. Lin and K. L. Tan, *Nature*, 2002, **420**, 302–304.

[124] Y. Nakamori, G. Kitahara, K. Miwa, S. Towata and S. Orimo, *Appl. Phys. A*, 2005, **80**, 1–3.

[125] D. H. Gregory, *Coord. Chem. Rev.*, 2001, **215**, 301–345.

[126] G. V. Vajenine, X. Wang, I. Efthimiopoulos, S. Karmakar, K. Syassen and M. Hanfland, *Phys. Rev. B*, 2009, **79**, 224107.

[127] G. V. Vajenine, *Inorg. Chem.*, 2007, **46**, 5146–5148.

[128] D. Fischer and M. Jansen, *Angew. Chem., Int. Ed.*, 2002, **41**, 1755–1756.

[129] D. Fischer, Z. Cancarevic, J. C. Schön and M. Jansen, *Z. anorg. allg. Chem.*, 2004, **630**, 156–160.

[130] E. Zintl and G. Brauer, *Z. Elektrochem. Angew. Phys. Chem.*, 1935, **41**, 102.

[131] A. Rabenau and H. Schulz, *J. Less-Common Met.*, 1976, **50**, 155–159.

[132] A. Lazicki, B. Maddox, W. J. Evans, C.-S. Yoo, A. K. McMahan, W. E. Pickett, R. T. Scalettar, M. Y. Hu and P. Chow, *Phys. Rev. Lett.*, 2005, **95**, 165503.

[133] C. C. Addison and B. M. Davies, *J. Chem. Soc. A*, 1969, **0**, 1831–1832.

[134] M. G. Down, P. Hubberstey and R. J. Pulham, *J. Chem. Soc., Dalton Trans.*, 1975, **14**, 1490–1492.

[135] S. Ishiyama, Y. Baba, R. Fujiib, M. Nakamurab and Y. Imahori, *Nucl. Instrum. Methods Phys. Res., B*, 2012, **293**, 42–47.

[136] M. van den Borg, D. Gaissmaier, D. Fantauzzi, E. Knobbe and T. Jacob, *ChemSusChem*, 2022, **15**, e202101765.

[137] T. Ludwig, A. R. Singh and J. K. Nørskov, *J. Phys. Chem. C*, 2020, **124**, 26368–26378.

[138] E. Kaxiras, Y. Bar-Yam and J. D. Joannopoulos, *Phys. Rev. B*, 1987, **35**, 9625.

[139] M. Scheffler and J. Dabrowski, *Phil. Mag. A.*, 1988, **58**, 107–121.

[140] G.-X. Qian, R. M. Martin and D. J. Chadi, *Phys. Rev. B*, **38**, 7649–7663.

[141] *https://creativecommons.org/licenses/by-nc-nd/4.0/*.

[142] M. Armand and J. M. Tarascon, *Nature*, 2008, **451**, 652–657.

[143] A. Varzi, R. Raccichini, S. Passerini and B. Scrosati, *J. Mater. Chem. A*, 2016, **4**, 17251–17259.

[144] D. Andre, S.-J. Kim, P. Lamp, S. F. Lux, F. Maglia, O. Paschos and B. Stiaszny, *J. Mater. Chem. A*, 2015, **3**, 6709–6732.

[145] J. Janek and W. G. Zeier, *Nat. Energy*, 2016, **1**, 16141.

[146] K. Mizushima, P. C. Jones, P. J. Wiseman and J. B. Goodenough, *Solid State Ion.*, 1981, **3**, 171–174.

[147] D. Guyornard and J.-M. Tarascon, *Adv. Mater.*, 1994, **6**, 408–412.

[148] D. Aurbach, I. Weissman, A. Zaban and O. Chusid, *Electrochim. Acta*, 1994, **39**, 51–71.

[149] D. Aurbach, I. Weissman, A. Zaban and P. Dan, *Electrochim. Acta*, 1999, **45**, 1135–1140.

[150] Y. Lu, Z. Tu and L. A. Archer, *Nat. Mater.*, 2014, **13**, 961–969.

[151] K. A. O'Hearn, M. W. Swift, J. Liu, I. Magoulas, P. Piecuch, A. C. T. van Duin, H. M. Aktulga and Y. Qi, *J. Chem. Phys.*, **153**, 08410.

[152] T. Verstraelen, P. W. Ayers, V. V. Speybroeck and M. Waroquier, *J. Chem. Theory Comput.*, 2013, **138**, 74108.

[153] M. M. Islam, G. Kolesov, T. Verstraelen, E. Kaxiras and A. C. T. van Duin, *J. Chem. Theory Comput.*, 2016, **12**, 3463–3472.

[154] D. Gaissmaier, M. van den Borg, D. Fantauzzi and T. Jacob, *ChemRxiv*, 2022.

[155] R. Rüger, M. Franchini, T. Trnka, A. Yakovlev, E. van Lenthe, P. Philipsen, T. van Vuren, B. Klumpers and T. Soini, *AMS 2021, SCM, Vrije Universiteit,*.

[156] D. Raymand, A. C. T. van Duin, W. D. Spangberg and and K. Hermansson, *Surf. Sci.*, 2010, **604**, 741–752.

[157] A. C. T. van Duin, K. J. C. Zou, V. Bryantsev and W. A. G. III, *A ReaxFF Reactive Force-field for Proton Transfer Reactions in Bulk Water and its Applications to Heterogeneous Catalysis*, Computational Catalysis (The Royal Society of Chemistry), 2014, pp. 223–243.

[158] T. P. Senftle, R. J. Meyer, M. J. Janik and A. C. T. van Duin, *J. Chem. Phys.*, 2013, **139**, 044109.

[159] K. Kunc, I. Loa, A. Grzechnik and K. Syassen, *physica status solidi (b)*, 2005, **242**, 1857–1863.

[160] B. R. Didar, L. Yashina and A. Groß, *ACS applied materials & interfaces*, 2021, **13**, 24984–24994.

[161] F. Fiesinger, D. Gaissmaier, M. van den Borg, J. Beßner, A. C. T. van Duin and T. Jacob, *ChemSusChem.*, 2023, **16**, e202201821.

[162] P. Debye, *Ann. Phys.*, 1915, **351**, 809–823.

[163] D. T. Cromer and J. B. Mann, *Acta Cryst*, 1968, **24**, 321–324.

[164] S. Indris, P. Heitjans, H. E. Roman and A. Bunde, *Phys. Rev. Lett.*, **84**, 2889–2892.

[165] F. Fiesinger, D. Gaissmaier, M. van den Borg and T. Jacob, *ChemSusChem.*, 2022, **15**, e202200414.

[166] R. R. A. Freund, M. van den Borg, D. Gaissmaier, R. Schlosser, T. Jacob and H.-D. Arndt, *Chem. Eur. J.*, 2020, **26**, 8639–8650.

[167] S. Maloul, M. van den Borg, C. Müller, L. Zedler, A. K. Mengele, D. Gaissmaier, T. Jacob, S. Rau, B. Dietzek-Ivanšić and C. Streb, *Chem. Eur. J*, 2021, **27**, 16846–16852.

[168] K. P. Huber and G. Herzberg, *Molecular Spectra and Molecular Structure. IV. Constants of Diatomic Molecules*, Van Nostrand Reinhold Co., 2nd edn, 1979.

[169] G. I. Csonka, J. P., Perdew, A. Ruzsinszky, P. H. T. Philipsen, S. Lebègue, J. Paier, O. A. Vydrov and J. G. Ángyán, *Phys. Rev. B*, 2009, **79**, 354.

[170] W. R. Tyson and W. A. Miller, *Surf. Sci.*, 1977, **62**, 267–276.

[171] L. Vitosa, A. V. Rubana, H. L. Skrivera and J. Kollar, *Surf. Sci.*, 1998, **411**, 186–202.

List of Figures

2.1 Schematic representation of the different methods in computational chemistry within their different length and time scales and the respective possible applications. 9
2.2 Illustration of the bond length/bond order relation exemplified for a C-C bond. Reprinted (adapted) with permission from [53] (*Copyright 2001 American Chemical Society*). 21
2.3 Scheme for the classification of ReaxFF in the multiscale hierarchy. . 24

3.1 Adsorption sites on the low-index surfaces. Li(100) in **(a)** : hollow (h), bridge (b), subsurface (s) and top (t), Li(110) in **(b)**: long-bridge (lb), hollow (h), short-bridge (sb), subsurface (s) and top (t)) and Li(111) in **(c)**: hcp, fcc, bridge (b), subsurface (s) and top (t). Depending on the layer, the lithium atoms are illustrated in different shades of grey. In **(d)** an exemplary illustration of the surface structure of the Li(100) surface after monoatomic absorption and a summary of the occurring clusters. The coordinating lithium atoms are shown in blue and oxygen in red. 32
3.2 Surface structures of absorbed oxygen on Li(100) on the respective adsorption sites. For illustration purposes the coordinating lithium atoms are shown in blue and oxygen is represented with the same colour code from Fig 3.1. 36
3.3 Absorption structures of dissociated O_2 on Li(100). The molecular oxygen dissociated in structures in which it was present in a combination of the observed clusters from Fig. 3.1. The labelling of the structures refers to the corresponding adsorption sites on Li(100). 37

3.4 Energy profiles for the surface and bulk diffusion of oxygen obtained using NEB calculations. The energy profile in **(a)** shows the diffusion from a *hollow* site to a neighbouring *bridge* site via an intermediate local minima (*lm*), followed by a diffusion to an adjacent *subsurface* position on the Li(100) surface. The blue path represents the monoatomic path, while the red path represents the equivalent diffusion from structure *h1h2* to *h1s1* by passing *h1b2* from Fig. 3.3. The framed values indicate the relative energy related to the most stable *hollow* (and *h1h2*) structure in eV. The diffusion profile for an oxygen atom through the bulk-Li(bcc) structure is shown in **(b)**. The framed values indicate the relative energy in eV related to the most stable structure. The diffusion takes place from a position in the bulk material in which oxygen is octahedrally coordinated via a tetrahedral transition state to equivalent octahedral coordination. Shown are the structures of the octahedrally coordinated initial and final structure, as well as the tetrahedral transition state. In **(c)** the surface sections and corresponding clusters refer to the structures illustrated in the diffusion profile for the monoatomic surface diffusion. For illustration, the coordinating lithium atoms at the surface are depicted transparently in the clusters as well. 39

3.5 Schematic illustration of cluster formation on Li(100), which caused rearrangements on the surface at higher coverages. The blue symbols represent the attraction of Li atoms towards oxygen at lower coverages, leading to the formation of an ordered arrangement of clusters. The red symbols depict the attraction towards several oxygen atoms at higher coverages, which leads to a reorganisation of the surface. 42

3.6 Binding energies per oxygen atom $E_{\mathrm{bind,O}}$ in eV as a function of the oxygen coverage Θ_{O} shown in **(a)**. The grey area represents the range, where a strong reorganisation of the Li(100) surface structure to an amorphous arrangement was observed. In **(b)** a phase diagram for the surface oxidation of Li(100) as a function of the oxygen chemical potential is shown. For fixed temperatures of 300 K and 400 K, the chemical potential has been translated to the corresponding pressures. The grey area resembles the oxygen-rich environment, where the Li_2O bulk oxide results as the most stable phase. In **(c)** sections of the most stable Li(100) surfaces at different oxygen coverages Θ_{O} are shown. . 44

3.7 Projected density of states (PDOS) for the most stable Li(100) absorption structures at different oxygen coverages Θ_O. Shown are the averaged PDOS of all lithium (blue) and oxygen (red) atoms. The states that belong to a lithium atom coordinating an oxygen atom are represented by a black dashed line. 46

4.1 Surface structures of absorbed nitrogen on different adsorption sites on the low-index surfaces Li(100) in **(a)**−**(d)**, Li(110) in **(e)**−**(i)** and Li(111) in **(j)**−**(n)**. Lithium atoms of different layers are portrayed in different shades of grey. Nitrogen is shown in purple and the coordinating lithium atoms in blue. The graphic above is an exemplary depiction of the different cluster-like coordinations, which were formed on the absorption of hydrogen on the different lithium surfaces. 55

4.2 Energy profiles for the surface and bulk diffusion of nitrogen. The energy profile in **(a)** shows the diffusion on a Li(100) surface from a *hollow* site to a neighbouring *bridge* site via two intermediate local minima, followed by diffusion to a neighbouring *subsurface* position, by passing another local minimum. The framed values indicate the relative energy in eV related to the initial *hollow* position. The surface sections and corresponding clusters shown in **(1)** - **(6)** refer to the structures illustrated in the diffusion profile for the monoatomic surface diffusion. For illustration, the coordinating lithium atoms at the surface are depicted transparently in the clusters as well. The diffusion profile for a nitrogen atom through the Li(bcc)-bulk structure is shown in **(b)**. The framed values indicate the relative energy in eV related to the most stable structure. The diffusion takes place from a position in the bulk material in which nitrogen is octahedrally coordinated to an equivalent octahedral coordination. Shown are the structures of the octahedrally coordinated initial and final structure, as well as the transition state. 59

4.3 Summary of the different cluster-like coordinations, which were formed on the absorption of N_2 on metallic lithium surfaces. The coordinating lithium atoms are shown in blue and nitrogen in purple 61

4.4 Energy profiles for the diffusion and dissociation of a single N_2 molecule on Li(100) obtained by means of NEB calculations. The different paths in **(a)** - **(f)** were assigned to the profile via a colour code. The numbering of the structures corresponds to that in the energy profile. The relative energies in the energy profile were all related to the initial, undissociated structure. 62

4.5 Binding energies per nitrogen atom $E_{\mathrm{bind,N}}$ in eV as a function of the nirtogen coverage Θ_{N} shown in **(a)**. The grey area represents the range, where a strong reorganisation of the Li(100) surface structure to an amorphous arrangement was observed. In **(b)** a phase diagram for the surface oxidation of Li(100) as a function of the nitrogen chemical potential is shown. For fixed temperatures of 300 K and 400 K, the chemical potential has been translated to the corresponding pressures. The grey area resembles the nitrogen-rich environment, where the $\mathrm{Li_3N}$ results as the most stable phase. In **(1)** - **(6)** sections of the most stable Li(100) surfaces at different nitrogen coverages Θ_{N} are shown. Here, the coordinating lithium atoms are coloured blue. To illustrate the coordination geometries, the bonds between the coordinating lithium atoms are drawn. 66

5.1 Schematic illustration of the investigated processes of H_2O on metallic lithium anodes. 71

5.2 Surface structures of absorbed hydrogen on different adsorption sites on the low-index surfaces Li(100) in **(a)**−**(e)**, Li(110) in **(f)**−**(j)** and Li(111) in **(k)**−**(o)**. Lithium atoms of different layers are portrayed in different shades of grey. Hydrogen is shown in white and the coordinating lithium atoms in blue. The graphic above is an exemplary depiction of the different cluster-like coordinations, which were formed on the absorption of hydrogen on the different lithium surfaces. 76

5.3 Energy profiles for the diffusion of a hydrogen atom on the Li(100) surface and in the bulk material. The energy profile in **(a)** shows the diffusion pathway on Li(100) from a *hollow* site into a neighbouring *subsurface* position, by crossing an adjacent *bridge* and *subbridge* position. The framed values indicate the relative energy in eV, which were related to the most stable *hollow* structure. The energy profile for the diffusion of a hydrogen atom through the Li(*bcc*)-bulk structure is shown in **(b)**. In bulk-lithium hydrogen diffuses from an octahedrally-coordinated environment via a tetrahedral transition state to an equivalent octahedrally-coordinated. Shown are the structures of the octahedrally coordinated initial and final configurations, as well as the tetrahedral transition state. The framed values indicate relative energies related to the octahedrally-coordinated structure. 80

5.4 Energy profile for the dissociation of molecular hydrogen into two adjacent *bridge* positions on Li(100). The framed values indicate the relative energy related to the Li(100)-H_2 adsorption complex. 82

5.5 Top view of the different absorption complexes of an OH molecule in **(a)**−**(e)**, and **(f)** the adsorption structure of H_2O on Li(100). Hydrogen is shown in white, oxygen in red and the coordinating lithium atoms in blue. 83

5.6 Energy profile for the diffusion of an OH molecule on Li(100) in **(a)**, which shows the transition from an OH-molecule in the *bridge* position towards the *hollow* site. In this diffusion process, the OH molecule passes through two local minima, which have been labelled as *sidebridge* and *sidehollow*. The framed values indicate the relative energy, which was related to the initial *bridge* structure. The energy profile for the dissociation of an OH molecule on Li(100) is shown in **(b)**. The pathway shows an OH molecule in the *sidehollow* position releasing its hydrogen atom to the opposite *bridge* position. The framed values indicate the relative energies, which are related to the undissociated OH *sidehollow* absorption complex. 84

5.7 The energy profile in **(a)** shows the diffusion of a H_2O molecule on Li(100) from one *bridge* to another (via flip and twist mechanism) and the diffusion from a *bridge* position to a *top* position. The relative energies in the framed values are referred to the H_2O molecule in the Li(100) *bridge* position. The energy profile for the dissociation of an H_2O molecule on Li(100) is shown in **(b)**. The pathway shows a H_2O molecule in the *bridge* position releasing one of its hydrogen atoms into the opposite *bridge* position. The framed relative energies are related to the undissociated H_2O *bridge* adsorption complex. 86

5.8 The energy profile in **(a)** shows the hydrogen evolution through the reaction of a hydrogen atom in the *bridge* position with an OH molecule and **(b)** with a H_2O molecule on Li(100). Both profiles show the dissociation of the respective molecule under the release of one of their hydrogen atoms towards the adsorbed hydrogen atom. The framed relative energies are related to the respective undissociated structures. 89

5.9 Top view of the undissociated adsorption/absorption complexes of OH and H_2O on Li(100) in **(a)**−**(b)** and the respective complexes in the presence of a hydrogen atom in **(c)**−**(d)**. The figures in **(e)**−**(h)** show the charge density difference isosurfaces of the corresponding undissociated structures. Blue regions indicate an increase and red regions a decrease in electron density. The illustrations **(i)**−**(j)** show the top view of the dissociated OH and water molecule on Li(100) and **(k)**−**(l)** the corresponding structures in the presence of the generated H_2 molecule. 90

5.10 Schematic representation of the steps in the HER on Li(100). In a Volmer-like step, a water molecule adsorbs on the lithium surface and dissociates to form an adsorbed hydrogen atom and OH molecule. Analogous to the Heyrovsky mechanism in an alkaline medium, another water molecule attacks the adsorbed hydrogen atom in the next step, forming an OH and H_2 molecule. In comparison, a recombination of two adsorbed hydrogen atoms according to the Tafel mechanism is unlikely. 92

6.1 Equations of state for different bulk phases calculated with ReaxFF in **(a)** and DFT in **(b)** and the respective ReaxFF optimized crystal structures in **(c)**-**(d)**. Lithium atoms are represented as grey and oxygen atoms as red spheres. 102
6.2 Overview of the different stages of GCMC simulated oxidation of the pristine lithium nanoparticle at 300 K and 0.21 atm. In the grey area, equilibration of the nanoparticle was performed at a fixed Li:O ratio of 2:1. 108
6.3 Recrystallization of an amorphous Li_2O nanoparticle into the *anti*-fluorite phase through simulated thermal annealing at 1000 K in an NVT ensemble. 109
6.4 Radial distribution functions (RDFs) for pure lithium, an amorphous (before annealing), and a crystalline (after annealing) Li_2O nanoparticle. 110
6.5 Simulated powder XRD pattern of a pure lithium particle (black), and an oxidized particle before (red) and after annealing (blue). The intensities $I(\theta)$ are given in arbitrary units and 2θ refers to the incidence angle of the Cu-K-α radiation. The annealed Li_2O particle diffraction peaks were assigned the Miller index of the corresponding atomic plane in analogy to Ref. [164] 111

7.1 Calculated PES (DFT-PBE) for the (4 x 4) Li(100), (4 x 6) Li(110), (4 x 4) Li(111), and (4 x 8) Li(211) surface unit cells. The relative coordinates are given in relation to the supercell 114
7.2 Schematic representation of a Mg(0001) surface and different possible self-diffusion processes. 116
7.3 Snapshots of the initial nucleation and aggregation processes on 100x100 Li(100) (red, (a)-(e)) and 100x100 Na(100) (yellow, (f)-(j)) at 200 K and a surface coverage of 0.125 ML. The initial configuration was generated by a random distribution of adatoms on the respective surface. Hopping and exchange processes were considered for both systems, and the number of adatoms was kept fixed during the simulation. 117
7.4 Schematic representation of the oxidation process of a Mg(0001) surface. 119

7.5 Computed rotational energy profile of simplified α,β-epoxy aldehydes. Level of theory: B3LYP-D3(BJ)/cc-pVDZ (vacuum). Grey areas show the possible range of conformations associated with the respective stereoinduction model for nucleophile addition to the carbonyl (PFA: 285$\pm$ 5°, anti-PFA: 75 $\pm$ 5°, CE: 165 $\pm$ 15°, anti-CE: 195 $\pm$ 15°). . 121

7.6 Energetically most favoured interaction sites between PS and POMPtI in (a) side view and (b) top view; (c) representation of the Fukui function calculated for the one-electron reduced POM-PtCl, shown as charge-difference plot. The iso-surfaces correspond to electron-accepting regions where an additional electron will be located (as indicated by the Fukui function). Regions with higher values are marked in darker shades of green. 123

A.1 Unit cell for bulk-Li_2O shown in **(a)**. The lithium and oxygen atoms are represented by grey and red spheres, respectively. In **(b)** the total density of states (TDOS) for bulk-Li_2O is shown in black. The partial density of states (PDOS) of lithium is shown in blue and in red for oxygen. 129

A.2 Binding energies per oxygen atom $E_{\mathrm{bind,O}}$ in eV as a function of the oxygen coverage Θ_{O} shown in **(a)**. The grey area represents the range, where a strong reorganisation of the Li(110) surface structure to an amorphous arrangement was observed. In **(b)** a phase diagram for the surface oxidation of Li(110) as a function of the oxygen chemical potential is shown. For fixed temperatures of 300 K and 400 K the chemical potential has been translated to the corresponding pressures. The grey area resembles the oxygen-rich environment, where the Li_2O bulk oxide results as the most stable phase. In **(c)** sections of the most stable Li(110) surfaces at different oxygen coverages Θ_{O} are shown. . 131

A.3 Schematic illustration of cluster formation on Li(110), which caused rearrangements on the surface at higher coverages. The blue symbols represent the attraction of Li atoms towards oxygen at lower coverages, leading to the formation of an ordered arrangement of clusters. The red symbols depict the attraction towards several oxygen atoms at higher coverages, which lead to a reorganisation of the surface. 132

A.4 Projected density of states (PDOS) for the most stable Li(100) absorption structures at different oxygen coverages Θ_{O}. Shown are the averaged PDOS of all lithium (blue) and oxygen (red) atoms. The states that belong to a lithium atom coordinating an oxygen atom are represented by a black dashed line. 133
A.5 Projected density of states (PDOS) for the most stable Li(100) absorption structures at different nitrogen coverages Θ_{N}. Shown are the averaged PDOS of all lithium (blue) and nitrogen (purple) atoms. The dashed lines display the states which can be attributed to nitrogen coordinating lithium atoms of the top layers. 134
A.6 Top view of the different arrangements of H_2O dimers on Li(100) in **(a)**-**(f)**. Hydrogen is shown in white, oxygen in red and the coordinating lithium atoms in blue. 137

List of Tables

3.1 Calculated binding energies in eV on the different surface sites shown in Fig. 3.1 (a)-(c). According to the number and geometry of the surrounding Li-atoms of the absorbates, the absorption structures were assigned to a type of cluster structure, corresponding to the ones shown in Fig. 3.1. The charge transferred to the oxygen atom during absorption was determined with the Bader and DDEC6 charge analysis and is given in e/atom. For the absorbed oxygen atoms, the respective sum of bond orders (SBO) is presented, as derived from the DDEC6 method. 33

3.2 Binding energies per atom $E_{\mathrm{bind,O}}$ on the Li(100) surface. The energies are referenced to molecular oxygen in the gas phase and are reported in eV. 38

3.3 ΔE_{for} and ΔE_{back} diffusion barriers for the respective forward and backward diffusion processes in eV. 41

3.4 Binding energies per atom $E_{\mathrm{bind,O}}$ on the Li(100) surface as a function of the oxygen coverage Θ_{O} in monolayers (ML) for different arrangements of the high-symmetry adsorption sites. The energies are referenced to molecular O_2 in gas phase and are reported in eV. 43

4.1 Binding energies per atom $E_{\mathrm{bind,N}}$ on Li(100), Li(110) and Li(111). The binding energies are reported in eV and are referred to molecular N_2 in the gas phase. The charge of nitrogen on its absorption was analyzed using the DDEC6 charge methodology [96, 97] and is reported in e/atom. 56

4.2 ΔE_{back} and ΔE_{for} diffusion barriers for the respective backward and forward diffusion processes of monoatomic nitrogen in eV. 60

4.3 Diffusion and dissociation barriers ΔE_{back} and ΔE_{for} of N_2 on Li(100) for the respective backward and forward processes in eV. Every second structure in every row was assigned its relative energy ΔE_{1-x} in eV (related to the initial structure) and the type of nitrogen cluster (see Fig. 4.1 or Fig. 4.3). 63
4.4 Binding energies per atom $E_{\mathrm{bind,N}}$ on the Li(100) surface as a function of the nitrogen coverage Θ_{N} in monolayers (ML) for different arrangements of the high-symmetry adsorption sites. The energies are referenced to molecular N_2 in gas phase and are reported in eV. 67

5.1 Binding energies per atom $E_{\mathrm{bind,H}}$ on the Li(100), Li(110) and Li(111) surface. The energies are referenced to a H_2 molecule in the gas phase and are reported in eV. The charge that was transferred to hydrogen on its absorption was analyzed within the DDEC6 charge methodology [96, 97] and is reported in e/atom. 77
5.2 ΔE_{back} and ΔE_{for} barriers in eV for the respective backward and forward diffusion/dissociation processes of hydrogen on the Li(100) surface and in Li(bcc) bulk. 82
5.3 Binding energies per molecule $E_{\mathrm{bind,mol.}}$ on Li(100). The energies were related to the respective molecular species in the gas phase and are reported in eV. 84
5.4 ΔE_{back} and ΔE_{for} barriers in eV for the respective backwards and forward diffusion, dissociation and reaction processes of OH and H_2O molecules on Li(100). 88

6.1 Comparison of lattice constants a_0 and c_0 in $\mathrm{\AA}$, formation energies E_{F} in eV and bulk modulus B_0 in GPa for $\mathrm{Li_2O}$ bulk phases, obtained from ReaxFF and DFT. The formation energies were calculated using equation 6.6 and the experimental values for the *anti*-fluorite phase are taken from [159]. 103
6.2 Calculated surface energies (γ) for low-index $\mathrm{Li_2O}$-surfaces in meV. . 105
6.3 Calculated ReaxFF and DFT binding energies in eV for the absorption of an oxygen atom on the high-symmetry adsorption sites of (6x6) (100), (4x6) (110) and (4x8) (111) lithium surfaces. The DFT values are taken from our previous work [68]. 106

A.1 Calculated and experimental values for O_2, Li(bcc) and Li_2O. For O_2 the bond distance (d_{O_2}) is reported in $\mathrm{\AA}$, dissociation energy $\left(E^{\mathrm{gas}}_{\mathrm{Diss},O_2}\right)$ in eV. Lattice constants (a) are reported in $\mathrm{\AA}$, cohesive energy (E_c) and formation energy (E_F) in eV, surface energies $\left(\gamma_{\mathrm{Li(hkl)}}\right)$ in $\mathrm{J \cdot m^{-2}}$ and bulk moduli (B) in GPa. The PBE and BEEF-vdW values for Li(bcc) correspond to those reported in Ref. [117] and [89]. 130

A.2 Binding energies per atom $E_{\mathrm{bind,O}}$ on the Li(110) surface as a function of the oxygen coverage Θ_O in monolayers (ML) for different arrangements of the high-symmetry adsorption sites. The energies are referenced to molecular O_2 in gas phase and are reported in eV. 132

A.3 Convergence study for the energy cutoff and number of k-points. Shown are the binding energies per molecule $E_{\mathrm{bind,mol}}$ on Li(100) for the respective settings. The Li(100)-$H_2O_{\mathrm{bri.}}$ structure corresponds to a Li(100) surface with a single water molecule on the bridge position. On the Li(100)-$OH_{\mathrm{sidebri.}} + H_{\mathrm{bri.}}$ structure the water molecule dissociated in a OH molecule in the *sidebridge* and a H atom in the *bridge* position. The energies were related to a single water molecule in the gas phase and are reported in eV. 135

A.4 ΔE_{back} and ΔE_{for} barriers in eV for the respective backward and forward diffusion, dissociation and reaction processes of OH and H_2O molecules on Li(100). 136

A.5 Binding energies per H_2O molecule $E^{\mathrm{dim}}_{\mathrm{bind,mol}}$ for the respective arrangements of a water dimer on Li(100) shown in A.6. The energies were related to water in the gas phase and are reported in eV. The interaction energy E_{Int} refers to the difference of the binding energy of the water dimers towards the one of a single water molecule $E^{\mathrm{sing}}_{\mathrm{bind,mol}}$ and is reported in meV: $E_{\mathrm{Int}} = E^{\mathrm{dim}}_{\mathrm{bind,mol}} - E^{\mathrm{sing}}_{\mathrm{bind,mol}}$. 137

Name: Matthias van den Borg

Erklärung

Ich versichere hiermit, dass ich die Arbeit selbständig angefertigt habe und keine anderen als die angegebenen Quellen und Hilfsmittel benutzt sowie die wörtlich oder inhaltlich übernommenen Stellen als solche kenntlich gemacht habe und die Satzung der Universität Ulm zur Sicherung guter wissenschaftlicher Praxis in der jeweils gültigen Fassung beachtet habe.
Ich bin damit einverstanden, dass die Dissertation auch zum Zweck der Überprüfung der Einhaltung allgemein geltender wissenschaftlicher Standards benutzt wird, insbesondere auch unter Verwendung elektronischer Datenverarbeitungsprogramme.

Ulm, den .....

Matthias van den Borg